The development of a multimodal imaging agent for the management of Diabetes Mellitus type 2

Asher Jay Garrod BSc

The University of Hull
School of Life Sciences
MSc By Research in Biomedical Sciences

Supervisors: Dr. Graeme Stasiuk & Dr. Justin Sturge

January 2019

Contents

Abstract

Diabetes Mellitus is a metabolic disorder with multiple aetiologies with an estimated 422 million people with the condition, which is characterised by the chronic presence of hyperglycaemia and dysfunction in carbohydrate, protein, and fat metabolism. Diabetes Mellitus is separated into two main types; Diabetes Mellitus Type 1 and Diabetes Mellitus Type 2. In Diabetes Mellitus Type 2, individuals often exhibit insulin resistance with the exact pathophysiology being unknown. However, what is known is that the β-cells (the insulin-producing cells of the pancreas) can change in mass and different observations have been reported as to how this affects the progression of the disease. Since there are several different observations, there is a need to produce an imaging agent which can help give visual evidence as to the changes in the β-cell mass within the pancreas. The aim of this project was to develop an multimodal imaging probe that could be used to image the β-cell mass and it's changes in the pancreas through MRI imaging and fluorescence microscopy.

A multimodal imaging probe was developed which has been synthesised by functionalising fluorescent quantum dots with Exendin-4 (for specific binding to GLP1-R) and Gd-DOTA-TA (for MRI imaging). The spectra of the probe showed an excitation wavelength of 400nm and an emission wavelength of 607nm. With the probe being determined to be 533.6nm in size and with a charge of -20.1mV, there was evidence of good conversion from the TGA ligands to the Exendin-4 and Gd-DOTA-TA. Despite this, the relaxivity of the QD-Exendin-Gd-DOTA-TA conjugate could not be determined due to the low concentration obtained. The confocal studies show that the imaging agent was internalised into the cell, with some indication of specific binding to the GLP1-R on the MIN6 cells. However, cell viability studies show error between readings, so it is unclear of the actual effects of the agent on the cell.

To conclude, the result of this study demonstrated the successful synthesis and functionalisation of the multimodal imaging probe with some future studies needed to optimise the functionalisation process. Furthermore, it was demonstrated that this probe can successfully enter MIN6 cells within 1 hour, and indicates specific binding to GLP1-R. This shows initial potential that this probe can specifically bind to cells expressing GLP1-R and can be used to visualise the mass present in the pancreas.

With this, in future studies, confocal studies can be conducted to focus on alternative cell lines that express this receptor, and the localisation of the probe within the cell. The synthesis of the imaging probe can be repeated and optimised to prevent aggregation. If this is done, a more accurate idea of the cytotoxicity can be done. This information can further indicate the probes potential in visualising the β-cell mass overtime to investigate it's changes.

Acknowledgements

I would primarily like to express my gratitude to Dr Graeme Stasiuk for providing me with the opportunity to undertake this project for me to achieve my MSc By Research in Biomedical Sciences. I thank all of the members of Dr Stasiuk's research group for making me feel part of the group. I want to thank the following members:

Michelle Kinnon; Thank you for teaching me the critical aspects of Chemistry and providing me with quantum dots which were necessary for me to conduct my Master's degree. You also became my friend, and I've experienced so much with you throughout the time I was doing my Master's and could not have done it without you.

Thomas Price; Thank you for going through my concerns and questions, even when they were repetitive and silly. Thank you for teaching me how to work GraphPad and giving me advice throughout my Master's degree.

Mitchell Clarke; Thank you for teaching me key aspects of quantum dot chemistry as well as providing me quantum dots for my experiments.

I would also like to thank members of the Biomedical Sciences department including

Dr Cordula Kemp, Dr Leigh Madden and Ellie Beeby; I'm grateful to you for training me in several biological techniques, for sharing your expertise and for guiding me throughout my Master's.

1. Introduction

1.1 The Pancreas

The Pancreas is a dual functioning gland located in the upper left abdominal cavity behind the stomach (Harris, 2013). The pancreas functions both as an exocrine and an endocrine gland (Pandol, 2011). The exocrine pancreas secretes digestive enzymes, water, and ions during digestion. The digestive enzymes are essential in processing food into its molecular components, and without this, malnutrition would follow (Pandol, 2010). The endocrine pancreas secretes hormones to maintain glucose concentration homeostasis (Nussey & Whitehead, 2001).

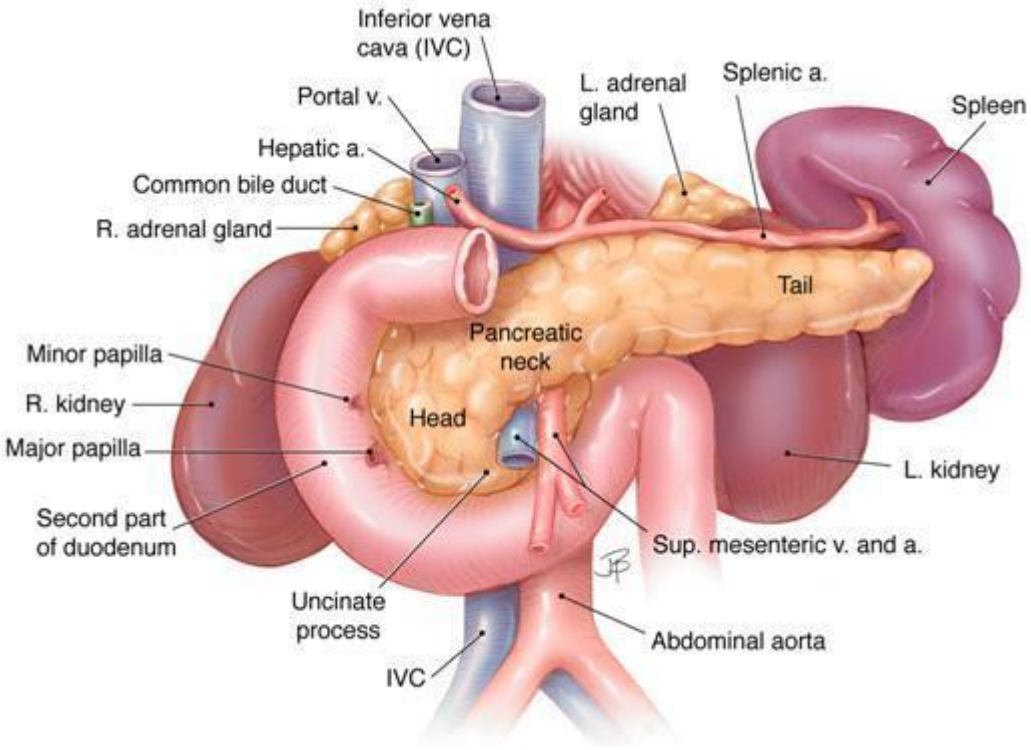

Figure 1.1: A diagram to illustrate the location of the pancreas in relation to other surrounding organs (Longnecker,2014)

The exocrine tissues are organised into what are known as acini. The acini are arranged in lobes and separated by thin, fibrous tissue (Longnecker, 2014). They are surrounded by intercalated ducts which drain into larger ducts. The role of the acini is to secrete digestive fluids and digestive enzymes, including amylases, lipases, and peptidases. The digestive enzymes drain through the ampulla of Vater into the duodenum (Baron *et al*., 2016). The endocrine tissues are called pancreatic islets or The Islets of Langerhans. The Islets contain five endocrine tissues, described in Table 1.1.

Table 1.1: Summary of the five endocrine tissues and their roles within the pancreatic Islets (Jarnagin, 2017)

Cell Type	**Role**	**Approximation of the cell distribution within a Pancreatic Islet**
α (Alpha)	Secretion of Glucagon	35%
β (Beta)	Secretion of Insulin	55%
δ (Delta)	Secretion of Somatostatin. Regulation of digestion and nutrient absorption.	10%
γ (Gamma)	Secretion of pancreatic polypeptide	5%
ε (Epsilon)	Secretion of Gherlin	<1%

The pancreas has a critical role in the regulation of blood sugar concentrations. α and β cells contribute to this regulation by maintaining a negative feedback system. Glucagon and Insulin which are secreted from the α and β cell respectively are essential hormones to maintain blood sugar concentration homeostasis and regulate metabolism (Roder *et al*., 2016). These secreted molecules which control blood sugar homeostasis will be discussed in further detail below.

1.1.1 Glucagon

Glucagon is a 29-amino acid polypeptide hormone, weighing 3.48 KDa, which belongs to the secretin hormone family (Jarnagin, 2017). As previously mentioned, this hormone is produced in the α cell of the pancreatic Islet. Glucagon is encoded from the GCG gene, which provides the proglucagon peptide. The proglucagon peptide is then processed by neuroendocrine convertase 2 to produce the glucagon peptide (Habegger *et al.,* 2010). Regulation of glucagons transcription occurs through homeodomain transcription factors which are influenced by cAMP and amino acids (Habegger *et al.,* 2010).

Glucagons secretion is related to the blood sugar levels present. Low levels of glucose directly stimulate the secretion of glucagon from the α cell (Olsen *et al.,* 2005) Secretion of glucagon occurs through the actions of voltage-dependent sodium (Na^+) and Calcium (Ca^{2+}) channels (Quesada *et al*., 2008). The effect of these voltage-dependent gates maintains action potentials. At low levels of glucose, K_{ATP} channels will cause the membrane potential to be approximately -60Mv. This causes depolarisation of the membrane to which Na^+ and Ca^{2+} channels will be activated. An influx of Ca^{2+} will occur to cause the release of glucagon by exocytosis (MacDonald *et al*., 2007). When glucose levels increase, cytosolic ratios of ATP/ADP will increase which in turn blocks K_{ATP} channels. This will depolarise the alpha cell membrane, and the membrane potential will be at a level the Na^+ and Ca^{2+} channels deactivate. Ca^{2+} influx will cease, and glucagon will not be secreted (Quesada *et al*., 2008).

In the liver, glucagon promotes glycogenolysis, gluconeogenesis, the breakdown of proteins, and ketone synthesis (Stanfield, 2013). Glycogenolysis occurs when glucagon binds to the glucagon receptors in the liver and conversion of glycogen to glucose occurs, with glucose then being released (Stanfield, 2013). Gluconeogenesis occurs when the stores of glycogen decrease, and new glucose will be synthesised by the liver and kidneys (Stanfield, 2013).

In adipose tissues, glucagon stimulates lipolysis and suppresses triglyceride synthesis (Stanfield, 2013). This process starts when glucagon binds to the glucagon receptor. This receptor is a G coupled receptor. In the plasma membrane, a conformational change will activate the G protein (which has an α, β, and γ subunit). At the place of the α subunit, GDP is replaced by GTP. The α subunit is released (Habegger *et al.,* 2010).

The release of the α subunit activates adenylate cyclase. cAMP is produced, and protein kinase A is activated. This, in turn, activates phosphorylase kinase. This enzyme phosphorylates glycogen phosphorylase-B. This creates the active form phosphorylase A. Phosphorylase A is responsible for the release of glucose-1-phosphate from polymers of glycogen. Glycolysis and Gluconeogenesis in the liver are controlled by the activator of glycolysis called fructose-2,6-biphosphate. Protein kinase A phosphorylates one serine residue on a polypeptide chain that contains the enzymes fructose-2,6-biphosphatase and phosphofructokinase-2. Phosphorylation activates the former and deactivates the

latter. This allows gluconeogenesis to predominate over glycolysis because the catalysing of fructose-2,6-biphosphatase is slowed (Habegger *et al.,* 2010).

1.1.2 Glucagon-like peptide 1

Glucagon-like peptide 1 (GLP-1) is a 31 amino acid polypeptide that is derived from post-translational modifications of proglucagon by the enzyme prohormone convertase 1 (Anandhakrishnan & Korbonits, 2016). GLP-1 is primarily synthesised by the enteroendocrine L cells, but it also expressed on pancreatic α cells and neurons on the brain stem region (Anandhakrishnan & Korbonits, 2016).

L-cells are located in the gastrointestinal mucosa and release GLP-1 when fatty acids, sugars, and amino acids are detected as the result of meal consumption (Lim & Brubaker, 2006). Primarily, GLP-1 activates reflexes that start gastric motility, that then results in gastric emptying. Secondly, GLP-1 activates vagal sensory nerve terminals which leads to initiation of vagal-vagal autonomic reflexes that control endocrine pancreas function (Spreckley *et al*., 2015). Circulating GLP-1, therefore, acts as a hormone at the Islets of Langerhans to stimulate the release of insulin. The actions of GLP-1 acts to lower blood sugar glucose (Nadkarni *et al*., 2014). GLP-1 and gastric inhibitory peptide (GIP) show evidence of effecting the increase in insulin secretion in response to the ingestion of food and resulting in the pancreatic β-cell mass increasing (Prasad-Reddy & Isaacs, 2015).

1.1.3 Insulin

Insulin is a 51 amino acid peptide hormone, with a molecular mass of 5.808 kDa (Jarnagin, 2012). It exists as a dimer with an A chain and B chain that is linked together by disulfide bonds.

As previously mentioned, insulin is produced by the β-cell in the pancreatic islet. Insulin is produced by the modification of the single polypeptide, preproinsulin. Preproinsulin is firstly directed to the rough endoplasmic reticulum (RER). In the lumen of the RER, preproinsulin is cleaved to form proinsulin (Fu *et al*., 2013). In the RER, proinsulin is folded correctly, and three disulfide bonds form. Proinsulin is then transported to the trans-Golgi network. Proinsulin will undergo maturation into the active form of insulin by the action of the following enzymes: cellular endopeptidases, prohormone convertases 1 and 2, and carboxypeptidase E. The endopeptidases cleave to release C peptide (Fu *et al*., 2013). This leaves the A and B chain linked by two disulfide bonds and two pairs of basic residues (Lysine-64, Arginine-65 or Arginine-31, Arginine-32). Carboxypeptidases remove these. Insulin is stored in granules until released by exocytosis. Insulin is sorted into clathrin-coated secretory granules and stored as a hexamer with two Zinc (Zn^{2+}) ions (Weiss *et al.,* 2018).

The events of insulin release are initiated when glucose is in high concentration outside the cell and moves

into the cell through facilitated diffusion through glucose transporter 2 (GLUT2). Glucose is then converted to pyruvate through glycolysis and enters the mitochondrial matrix. Oxidative phosphorylation takes place in the matrix and releases ATP into the cytosol (Fu *et al*., 2013). ATP acts as a ligand and binds ATP selective K+ channels causing them to close and blocking potassium movement out of the cell. This prevented potassium movement causes cell membrane depolarisation. This leads to calcium-gated channels to open and calcium to enter. Calcium then triggers insulin release by exocytosis (Fu *et al*., 2013). This process is illustrated in Figure 1.2 below.

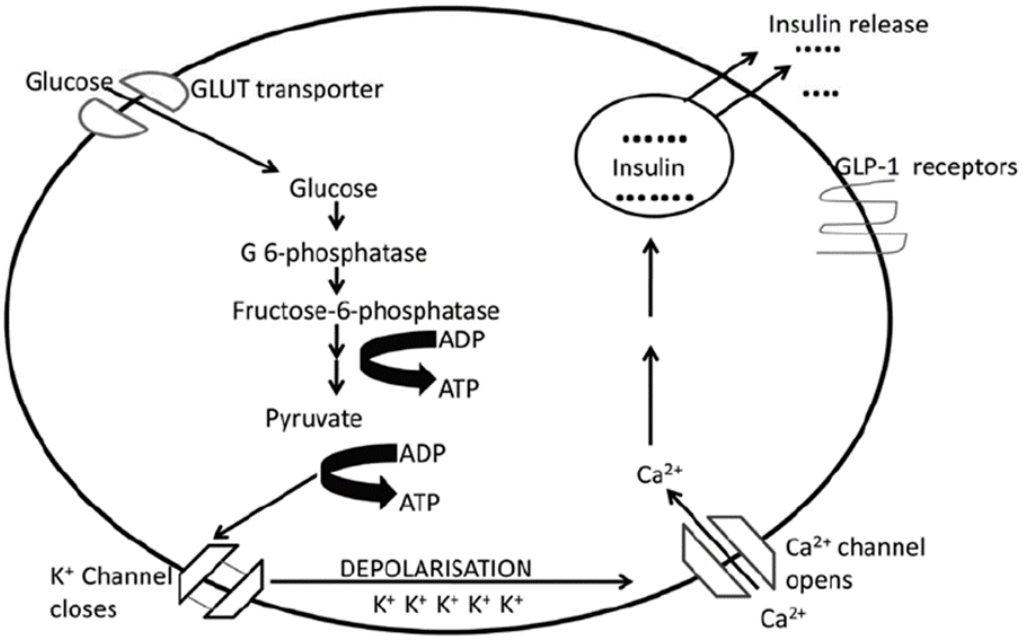

Figure 1.2: A diagram to summarise the events of insulin release in the pancreatic β-cell (Baur *et al*., 2012).

There are approximately 10,000 secretory granules per β-cell , but only 100 to 200 granules are capable of releasing their insulin in the first release phase (Brunner *et al.,* 2007). The remaining granules are in a reserve pool and undergo ATP dependent reactions to release their insulin by exocytosis (Brunner *et al.,* 2007). The pancreatic β cell has one of the highest concentrations of Zn^{2+} in a mammalian cell with a concentration range of between 10-20mM per insulin granule (Davidson *et al*., 2015). Insulin promotes the synthesis of fatty acids and triglycerides by a process called lipogenesis in the liver and adipose tissue, and it also suppresses the process of gluconeogenesis in the liver. Insulin also promotes glycogenesis, the process of glycogen synthesis from glucose (Weiss *et al.,* 2018).

1.2 Glucose

Glucose is a monosaccharide which consists of six carbon atoms and an aldehyde group. It exists as an acyclic and cyclic form. Glucose is a primary source of energy for living organisms and can occur naturally in fruits or plants, or it can be formed as a result of the breakdown of glycogen (glycogenolysis). Glucose is also synthesised in the liver and kidneys from pyruvate and glycerol (gluconeogenesis). Glucose is used in respiration to create ATP in the cells of the body to provide energy (Human Metabolome Database, 2019). Respiration can be aerobic or anaerobic. Aerobic respiration requires Oxygen and is summarised in Figure 1.3.

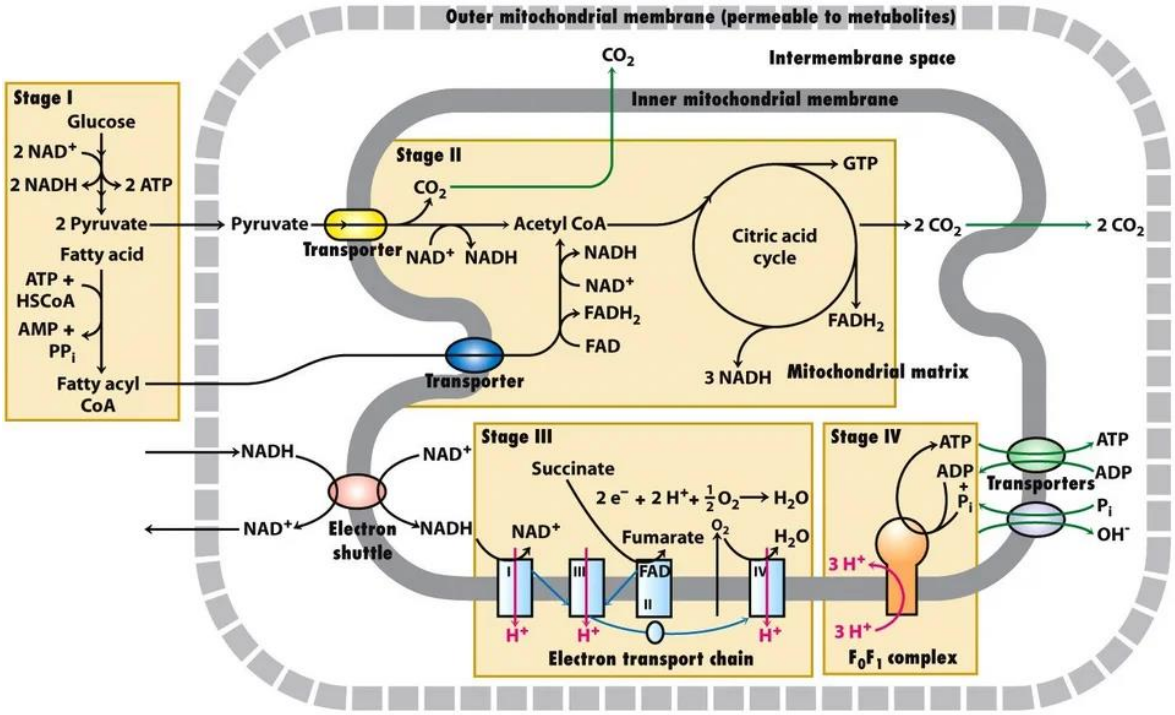

Figure 1.3: An illustration of the processes and where they are undertaken in aerobic respiration (Lodish *et al*., 2016)

1.2.1 The Movement of Glucose

Movement of glucose is enabled by membrane transporters which are either Na^+ dependent or Na^+ independent: Na^+ dependent glucose transporters include SGLT1 (found in the small intestine) and SGLT2 (found in the proximal renal tubule) (Weiss *et al*., 2018). These transporters use the concentration gradient of Na^+ to transport glucose, which will be moving against a concentration gradient (Weiss *et al*., 2018).

The concentration gradient of Sodium is maintained by Na^+/K^+ATPase ion pumps (Lodish *et al*. 2016).

Na^+ independent glucose transporters consist of a family of several isoforms (GLUT1 to GLUT7) (Weiss *et al*., 2016). These transporters facilitate the movement of glucose down its concentration gradient. GLUT4 is in the highest concentration in insulin-sensitive tissues (Weiss *et al*., 2014). GLUT1 enables them to increase their uptake of glucose, and this lowers the amount of circulating blood glucose (Lodish *et al*., 2016). Insulin enhances the uptake of glucose by increasing the number of Na^+ independent glucose transporters to the plasma membrane of target cells (Weiss *et al.,* 2018).

1.3 Diabetes Mellitus

Diabetes Mellitus is a metabolic disorder with multiple aetiologies with an estimated 422 million people with this condition (WHO, 2018). It is characterised by the chronic presence of hyperglycaemia, with the disturbance in the metabolism of carbohydrates, protein, and fats (Stanfield, 2013). The chronic presence of hyperglycaemia is a result of the pancreas not being able to produce insulin (in the required amounts, if at all) or has an impairment to react appropriately to insulin. This results in defects in insulin secretion or insulin action, or both (Stanfield, 2013). Diabetes Mellitus is separated into Diabetes Mellitus Type 1 (T1D) or Diabetes Mellitus Type 2 (T2D).

1.3.1 Diabetes Mellitus Type 1

Diabetes Mellitus Type 1 (T1D) occurs as the β-cells become partially damaged or entirely destroyed, leading to the pancreas being unable to produce sufficient insulin or it does not provide any at all. This is thought to be due to an autoimmune reaction causing the immune system to attack and destroy the β-cells. T1D accounts for 5-10% of all diabetes diagnoses (Stanfield, 2013).

Individuals with this condition are at risk of ketoacidosis because the lack of insulin prevents glucose absorption. Therefore, inhibiting the production of oxaloacetate through reduced levels of pyruvate. This results in the production of ketone bodies being unregulated, potentially increasing the levels of glucose in the blood (Stanfield, 2013). T1D is classified into Type 1a and Type 1b which represent a genetic cause or an environmental cause of T1D, respectively (Stanfield, 2013). Type 1a is a subclass that describes cases which those with T1D had an autoimmune reaction that involves their antibodies attacking the β-cells.

In histological examinations of those with T1D, autoimmune reactions are identified as samples often show activated lymphocytes and autoantibodies to pancreatic proteins (Lebastchi & Herlond, 2012).

Autoantibodies are antibodies that react to self-antigens and have the potential to be found in all cell types within the human body (Schmidt & Leslie, 2005). They can be highly specific and may compromise the function of proteins, carbohydrates, lipids, and nucleic acids. Many autoantibodies are a marker of a pathological process (Elkon & Casali, 2009).

Type 1 Diabetes can also be caused by environmental factors including viral infections which expose a genetic predisposition. Viruses which may induce the β cell destruction include viral infections of the gastrointestinal tract (coxsackie B) which will cause the immune system to try to clear the infection, but cause destruction (Coppieters *et al*., 2012).

Another virus is Rubella which can cause a general response to attack several β cell proteins (Coppieters *et al*., 2012). In diagnosis, markers of this destruction can be identified, and they include islet cell autoantibodies, autoantibodies to insulin, GAD65, tyrosine phosphatases IA-2 and IA-2 β (Stanfield, 2013).

1.3.2 Diabetes Mellitus Type 2

Diabetes Mellitus Type 2 (T2D) occurs typically due to an excess of calorie intake over energy expenditure and progressively insulin resistance occurs. This increases the body's demand for insulin to maintain glucose homeostasis (Fu *et al*., 2013). This disease is heterogenous caused by a combination of genetic and environmental factors (Stanfield, 2013). Genetic factors can affect the genes associated with impaired insulin secretion, insulin resistance. Environmental factors such as diet, lack of exercise, alcohol intake, cigarette consumption, and stress affect the onset and progression of T2D (Stanfield, 2013)

Chronic hyperglycaemia is present in this disease with long-term damage to tissues in the blood vessels, nerves, eyes, kidneys, and heart. T2D makes up 85-90% of all diabetes diagnoses. The exact pathophysiology is unknown, but the disease is associated with an increase in glucose production, impaired insulin action, and loss of insulin secretion (Papatheodorou *et al.,* 2016).

1.4 Symptoms and complications

1.4.1 Symptoms

Diabetes is often varied considerably between individuals and can often be asymptomatic in nature, especially in the early stages of Type 2 Diabetes, but common symptoms include: polyuria (excessive urination), polydipsia (excessive thirst), polyphagia (excessive eating, or appetite), fatigue, weight loss (without intending to do so), recurrent infections, recurrent wounds that won't heal, blurred vision, thrush. Individuals should seek medical attention immediately if they present with the following symptoms: No appetite, vomiting, stomach pain, a fruity/chemical smell on the breath, as these symptoms could be a sign of ketoacidosis (Ramachandran, 2014).

1.4.2 Complications

Complications in Diabetes often affect the vascular system of the body and therefore, effects can be micro or macrovascular. The main microvascular complications include neuropathy, nephropathy, and retinopathy. Induced by chronic hyperglycaemia via advanced glycation end products (AGE), and the creation of proinflammatory microenvironment, and the induction of oxidative stress. (Fowler, 2011).

Diabetic polyneuropathy (DPN) is the most common diabetic complication and is a leading cause of disability due to the development of foot ulcers, and a foot or leg amputations, and fall-related injuries. (Papatheodorou *et al*., 2016). Sensory symptoms often start in smaller nerves, located in the toes and fingers. Over time, the damage and sensory symptoms continue throughout the limbs in the classic 'stocking and glove' distribution pattern. Individuals will at this stage start to experience loss in sensation, and pain sensation, tingling, burning sensations, allodynia, or hyperalgesia. Diagnosis of DPN is made on neurologic exam and nerve conduction studies. The pathogenesis of DN is complicated and has many contributing factors, which include metabolic factors, hyperglycaemia, oxidative stress, mitochondrial dysfunction, the formation of AGE products, and the addition of inflammatory products (Juster-Switlyk & Smith, 2016).

Diabetic nephropathy (DN) is the most common cause of end-stage renal disease with one-third of patients with Type 1 Diabetes Mellitus having end-stage renal disease (Sharaf El Din *et al*., 2017). The glomerular hyperfusion and hyperfiltration are present due to the decrease of the afferent arteriolar resistance. Increased glucose causes the Sodium Glucose Transporter 2 gene to stimulate increased absorption of filtered sodium and glucose (Papatheodorou *et al*., 2016). With increased sodium uptake, the proximal tubular epithelia wont absorb glucose into the filtrate, so it is not excreted.

Also, energy expenditure decreases and results in vasodilation, leading to polyuria (Sharaf El Din *et al.,* 2017). The increase in glucose availability leads to an increased activity in the polyol pathway, which results in fructose being synthesised. Fructose can result in an increase in uric acid intracellularly. Uric acid stimulates nicotinamide adenine dinucleotide phosphate (NADPH) oxidase enzyme causing increased intracellular oxidative stress, mitochondrial injury, adenosine triphosphate (ATP) depletion, endothelial injury, RAS activation and increased epithelial-mesenchyme transition (EMT) (Sharaf El Din *et al*., 2017).

Diabetic Retinopathy (DR) is a complication of diabetes associated with the retina of the eye becoming damaged, leading to vision impairment and sometimes, blindness. DR is complex and progressive (Mathebula, 2018). The mechanism that contributes to DR includes the polyol pathway, activation of protein kinase C, formation of AGE products, and oxidative stress. These microvascular changes contribute to macrovascular complications, such as atherosclerosis and strokes (Duh *et al*., 2017)

1.5 Diagnosis of Diabetes

Determining the type of diabetes an individual may have depended on several factors including family history, current medications, circumstance, time of diagnosis, and the results of plasma glucose tests: Fasting Plasma Glucose (FPG), HbA1c, Oral glucose tolerance test, and random plasma glucose (Chaudhury *et al.,* 2017). Other tests include ketone urine tests and peptide C tests (Brewster *et al*., 2017). Individuals often do not fit entirely into one category of diabetes and circumstance can change the diagnosis (Davidson, 2010). For example, individuals can develop diabetes on a large dose of exogenous steroids but can become normoglycemic after this medication is discontinued. This also may lead to a risk of diabetes in later years as episodes of pancreatitis can occur (Davidson, 2010).

1.5.1 HbA1c Test

Glycated haemoglobin (HbA1c) is a component of haemoglobin which is formed in a non-enzymatic glycosylation reaction (Leow, 2016). The reaction occurs between glucose and a Valine residue on the N-terminal end of the β chain in haemoglobin. The result forms a Schiff base aldimine intermediate. This is then converted to 1-deoxyfructose (Leow, 2016). The HbA1c test is, therefore, the measure of the β-N-1-deoxyfructosyl component of glycated haemoglobin.

The longer hyperglycaemia occurs, the more glucose can bind to haemoglobin and therefore more of HbA1c can form. The build-up of this component, therefore, reflects the levels of glucose in the blood (Renz *et al*., 2015). The lifespan of the red blood cell is approximately 120 days, which means this test can be used to identify a 3-month average of plasma glucose (Sacks, 2011). The test is used to diagnose higher levels of plasma glucose in those who are considered prediabetic and is used to monitor plasma glucose in individuals with diabetes.

The test can be used to show the effectiveness of medications diabetic patients are on (Chaudhury *et al.,* 2017).

This was first demonstrated in studies by Larsen *et al.* (1990). The studies showed that the monitoring of HbA1c (compared to monitoring urine glucose alone) in those with T1D lead to improvement in metabolic control. To those who did not show change, this led to a change in their medication which subsequently leads to an improvement of the remaining individuals. The measurement of HbA1c equals the assessment of fasting glucose levels and also captures postprandial glucose peaks; therefore, it could be said that HbA1c testing is more reliable than FPG and 2-h OGTT plasma glucose (Bonora and Tuomilehto, 2011). The test can be a good indicator of an individual's lipid profile, in a study by Khan *et al.* (2007), HbA1c levels directly correlated with levels of cholesterol and low-density lipoproteins.

This test requires little preparation, is highly reproducible and fasting is not needed which is advantageous (Bonora and Tuomilehto, 2011). HbA1c is measured by a variety of methods including high-performance liquid chromatography, capillary electrophoresis, and immunoassay although laboratories may differ in analytical technique (Urrechaga, 2012). Table 1.2 shows the levels of HbA1c in nondiabetic, pre-diabetic, and diabetic individuals. However, values in the interpretation of the results can differ. The International Diabetes Federation and The American College of Endocrinology recommend that levels of HbA1c should be above 48 mmol/mol (6.5%) however the American Diabetes Society suggest levels of HbA1c should be above 53 mmol/mol (7%) (Sherwani *et al.,* 2016).

Studies by Heller *et al.* (2017) show no difference in macrovascular complications or mortality in those with 48 mmol/mol however Currie *et al.* (2010) identified an increase in mortality in their retrospective study of 47,970 patients with type 2 diabetes with a HbA1c level of 48 mmol/mol or above. The different findings of the significance of HbA1c levels suggest that the test is needed for diabetic control and diagnosis. It also indicates that higher levels of HbA1c and glucose contribute to the pathophysiology of the disease. The test is not appropriate in all cases. For example, the analysis will underestimate the level of HbA1c in those with conditions which results in a shorter average of circulating red blood cell lifespan. This is because the test will assume normal red blood cell lifespan and subtypes of red blood cells. Hence, people with recent blood loss, sickle cell disease, iron deficiency anaemia, cystic fibrosis, or pregnancy are not suitable for the test (Wolfsdofr & Garvey, 2016).

Table 1.2: A table to show the levels of HbA1c per mmol/mol in non-diabetics, prediabetics, and diabetics. (Higgins, 2012).

Diabetic Progress	HbA1c (mmol/mol)
Non-Diabetic	<42
Prediabetic	42-47
Diabetic	>48

1.5.2 Fasting Plasma Glucose (FPG)

The fasting plasma glucose test is used to diagnose prediabetes and T2D. Patients are advised to not eat or drink (except water) for 8-10 hours before the scheduled test is performed. The test is aimed to identify if insulin is acting correctly. The test is for symptomatic individuals or high-risk individuals (Sacks, 2011). When the body is in a fasting state, this should cause glucagon to be released. This should, in turn, cause glucose to be released into the bloodstream and glycogenolysis will occur in the liver (Sacks, 2011).
In healthy individuals, this is counteracted with the appropriate level of insulin. In T2D, insulin response or production will be impaired and thus, fasting blood sugar glucose will remain high (Sacks, 2011).

The results can be interpreted in milligrams per decilitre (mg/dl) or millimoles per litre (mmol/l).
Fasting plasma glucose tests below 6.1 mmol/l or 110 mg/dl are considered normal. Results between 6.1-6.9 mmol/l or 111-125 mg/dl are interpreted as an individual having impaired fasting glucose or prediabetic. Results of 7 mmol/l or above or 126mg/dl are considered diabetic (Ketema & Kibret, 2015).

The results can also be affected if the blood sample is analysed too long after it is taken from the patient. The test can also be affected by stress (this increases endogenous glucose production) and exercise (this can decrease concentrations of fasting glucose) (Bonora & Tuomilehto, 2011). Patients themselves may also cause an error in the test by not fulfilling the preparations required for the test. For example, patients are required to consume a diet of 200g of carbohydrates several days before the test is scheduled and must not eat 8-10 hours before the test, both of which a patient may not fulfil (Bonora & Tuomilehto, 2011). In a study by Rohlfing *et al.* (2002) Coefficients of variation of the HbA1c, FPG and 2-hour FPG had values of 3.6, 5.7, 16.6% respectively. Biological variability of HbA1c was lower than FPG (1% v. 4%) which suggests both tests should be taken.

1.5.3 Glucose Tolerance Test (GTT)

The glucose tolerance test is used to determine how quickly glucose is removed from the blood. If insulin is not adequately released or there is insulin resistance, the glucose will remain in the blood, showing high results of blood glucose (Higgins, 2012). The patient is required to fast for 8-12 hours, avoid medication, and eat less than 200g in carbohydrates before the fast. Blood is then taken to record the blood glucose levels at time 0. The patient then ingests a high glucose content drink, and a blood test is retaken after 2 hours (Higgins, 2012). Table 1.3 illustrates the levels of blood glucose in those who are nondiabetic and those with T2D.

Table 1.3: A table representing blood sugar before and after testing. It shows the levels shown to determine if a patient has normal blood glucose or has T2D.

	Normal Blood Glucose (mmol/l)	**Impaired glucose tolerance (mmol/l)**	**T2D (mmol/l)**
Fasting (before the test)	<6	6-7	>7
At 2 hours	<7.8	7.9-11	>11

1.5.4 C Peptide Test

Insulin is produced in the β-cell in the pancreatic islet and is modified from proinsulin (which is cleaved from preproinsulin). Proinsulin undergoes maturation into the active form of insulin by the action of the following enzymes: by cellular endopeptidases, prohormone convertases 1 and 2, and carboxypeptidase E (Fu *et al*., 2013). The endopeptidases cleave at two sections to release C peptide.

This cleavage of proinsulin leads to insulin and C peptide being released in equal amounts. C peptide can be measured, and results give clinicians an indication of β-cell function. The test is used to distinguish between Diabetes Mellitus type 1 and 2 as Type 1 Diabetics tend not to produce a lot of insulin and therefore not a lot of C-peptide (Leighton *et al*., 2017).

The test is more stable compared to measuring insulin alone as C peptide is degraded slower than insulin (Leighton *et al*., 2017). Furthermore, C peptide has negligible liver clearance meaning exogenous and endogenous insulin can be distinguished (Jones & Hattersley, 2013).

Disadvantages of the test are that it is inappropriate for those with kidney disease as C peptide is metabolised by the kidneys with approximately 10% of it being excreted in the kidneys. There have been advances in assays testing C peptide. Non-isotopic assays (e.g. fluorescent) reduce assay costs and improve reproducibility. There are still limitations to the assays however as there is no standardisation between laboratories (Jones & Hattersley., 2013).

1.6 Treatment of Diabetes

Treatment and management of diabetes are aimed at change in lifestyle and with the addition of pharmacological treatments. Lifestyle measures that are focused on are diet, exercise, weight, alcohol consumption, and cigarette consumption. Pharmacological treatments focus on the following: increased glucagon secretion, reduced insulin secretion, neurotransmitter release, increased lipolysis, increased glucose absorption in the nephron, reduced incretin release, decrease in glucose uptake in target tissues (Chaudhury *et al.,* 2017). Oral diabetic medications can be classified into Thiazolidinedione (TZD), sulfonylureas, dipeptidyl peptidase 4 (DPP-4) inhibitors, sodium-glucose cotransporter (SGLT2), α-glucosidase inhibitors, biguanides, meglitinide. Single or multiple medications (with or without insulin) may be used, and this often depends on an individual's HbA1C percentage. (Chaudhury *et al*., 2017).

1.6.1 Lifestyle Measures

Literature suggests that genetic and environmental factors are critical to the development of T2D. Environmental changes can be modified, and disease onset can possibly be prevented or slowed with lifestyle changes. This approach is advised for those newly diagnosed with type 2 diabetes or who are at risk of developing the T2D. (Asif, 2014). Lifestyle interventions aim to provide dietary and exercise advice which can be used to achieve goals such as: reducing saturated fat in the diet, replacing carbohydrates with whole grain alternatives, increase fruit and vegetable uptake and taking 2 and a half hours a week of moderate intensity exercise. Modification of a patients diet also should result in a patient being in a healthy BMI bracket (18.5-24.9) (Asif, 2014).

The benefits of changing the lifestyle in diabetic patients or those at risk of developing it was demonstrated by Knowler *et al.* (2002). This study was conducted with 3234 patients with elevated fasting glucose to placebo, metformin, or a lifestyle measures programme. Results demonstrated that a lifestyle measures programme reduced the incidence of diabetes by 58% compared to 31% of those who were placed on metformin in a period of 3 years. Early studies such as this demonstrated the effectiveness of changing environmental factors, such as diet, that contribute to the onset of diabetes.

1.6.2 Thiazolidinediones

Thiazolidinediones (TZD's) otherwise known as glitazones activate peroxisome proliferator-activated receptors (PPAR's) with the endogenous ligand for these receptors being free fatty acids (Tyagi *et al.,* 2011). When activated, the receptor binds to DNA in a complex with retinoid X receptor (PPAR, RXR complex). This, in turn, causes an increase in the transcription of genes that promote the storage of fatty acids in adipose tissue (Tyagi *et al.,* 2011). The PPAR, RXR complex binds to the peroxisome proliferator hormone response elements upstream of target genes. This causes upregulation of genes involved in a decrease in insulin resistance, leptin decrease, an increase in insulin sensitivity (Tyagi *et al.,* 2011).

Advantages of these group of medications are that they can be used to treat diabetic patients with chronic kidney disease/problems. One member of this drug group, pioglitazone (as shown in Figure 1.4), has been reported in the literature to have renal protective properties by decreasing urinary albumin and urinary protein (Sarafidis *et al*., 2010). However, there is evidence of cardiovascular disease risks with the drug rosiglitazone (another member of the thiazolidinedione drug group). A meta-analysis from studies conducted by Nissen & Wolski (2007) shows the risk of developing a myocardial infarction was increased significantly with rosiglitazone.

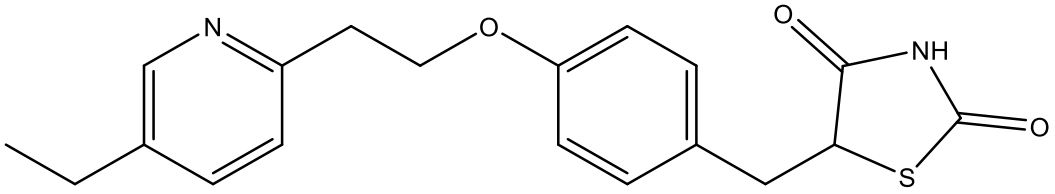

Pioglitazone

Figure 1.4: The chemical structure of Pioglitazone, a member of the Thiazolidinedione group of diabetic medications.

1.6.3 Sulfonylureas

Sulfonylureas are organic compounds which act to increase insulin release from the β cells. By doing so, this results in glucose being metabolised as opposed to free fatty acids (Broichhagen *et al*., 2014). Sulfonylureas work by binding to and closing ATP sensitive potassium channels of the β cells. This causes depolarization of the cell membrane (Broichhagen *et al*., 2014). This causes calcium-gated channels to open, increasing the amount of insulin storage granules that move and fuse to the cell membrane to release insulin (Broichhagen *et al*., 2014). Sulfonylureas, however, can induce hypoglycaemia, headaches, hypersensitivity, and stomach upsets (Sola *et al*., 2015).

1.6.4 Dipeptidyl Peptidase 4 Inhibitors

Dipeptidyl Peptidase 4 inhibitors are anti-hyperglycaemic medications which block the action of the enzyme Dipeptidyl Peptidase 4 (DPP-4) (Pathak & Bridgeman, 2010). This enzyme breaks down incretin. Incretin helps to increase the levels of insulin release and decrease the levels of glucagon release and blood glucose (Pathak & Bridgeman, 2010). Dipeptidyl Peptidase 4 inhibitors, therefore, aim to increase levels of incretin (Pathak & Bridgeman, 2010). DPP-4 inhibitors can be used alone or in combination with Metformin to treat T2D (Diabetes UK, 2018). Some of the most used of these inhibitors are illustrated in Figure 1.5.

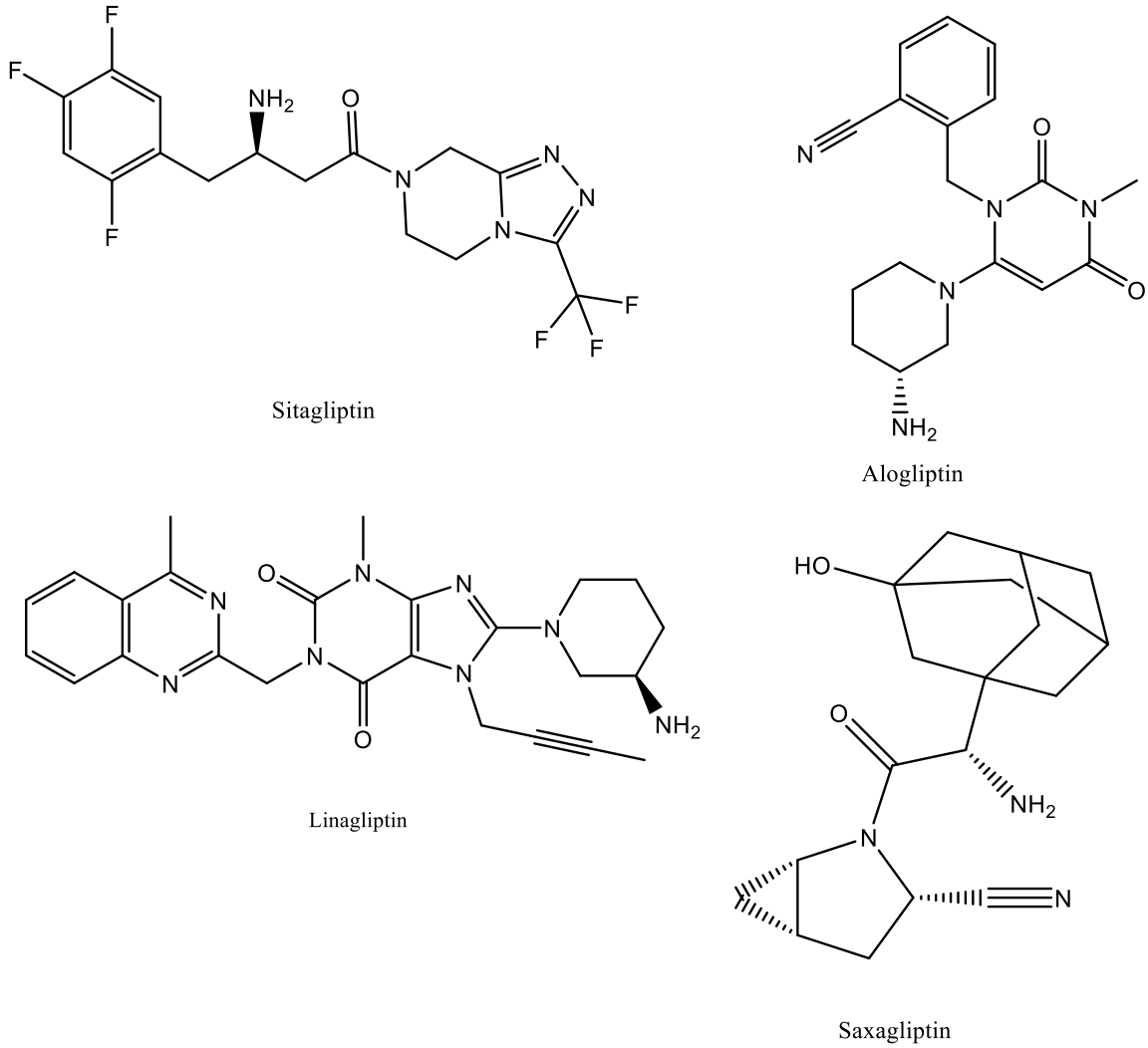

Figure 1.5: Chemical structures of four DDP-4 Inhibitors used in the United Kingdom. Sitagliptin (Top left), Alogliptin (Top right), Linagliptin (Bottom right), and Saxagliptin (Bottom left). They are either used individually or in combination with Metformin to block the activity of the enzyme Dipeptidyl Peptidase 4 (DPP-4) to stop the breakdown of Incretin, which in turn helps the release of Insulin which contributes to glucose homeostasis.

1.6.5 Sodium-Glucose Cotransporter 2 Inhibitors

Sodium-glucose cotransporter 2 (SGLT2) is a member of the sodium glucose cotransporter family which are sodium-dependent glucose transport proteins. SGLT2 is a significant cotransporter involved in glucose reabsorption in the kidney. Glucose is reabsorbed in the nephron via the proximal convoluted tubule. Inhibitors of SGLT2 are often called gliflozins and aim to reduce blood glucose levels. SGLT2 inhibitors inhibit SGLT2, therefore, preventing the reabsorption of glucose (Kalra, 2014).

Glucose is then excreted through the urine. Blood glucose levels will decrease as less glucose is reabsorbed and put back into the bloodstream.

1.6.6 α-glucosidase Inhibitors

α-glucosidase inhibitors are medications that prevent the absorption of carbohydrates. α-glucosidase inhibitors are saccharides that act as competitive inhibitors of enzymes required to digest carbohydrates. Inhibition of these enzymes means there is a reduced rate of digestion of carbohydrates. Less glucose is absorbed because the carbohydrates are not broken into glucose (Van de Laar, 2008).

1.7 β-Cell mass and imaging targets

In Diabetes, hyperglycaemia is the consequence of inadequate levels of insulin to lower levels of plasma glucose. Insulin levels are dependent on the β-cells producing and secreting it. The amount also depends on the total number of β-cells in the Islets, the β-cell mass, and the output of the cells (β-cell function) (Chen *et al*., 2017).

There is a suggestion that β-cells have compensatory abilities, which cause an increase in their mass, and that this prevents most obese and insulin resistant individuals from developing T2D (Chen *et al*., 2017). It is hypothesised that the increase in insulin release and expanded β-cell mass counteracts the development of hyperglycaemia. However, an article by Inaishi *et al*., (2016) reports that within eight studies into β-cell mass in T2D and non-diabetics, there is a decrease in β-cell mass, ranging from 24% to 65% which contradicts the findings in (Chen *et al*., 2017) who reported β-cell mass increase.

This observation of decreased β-cell mass was observed in Deng *et al.,* (2004). Reduced Islet sizes were seen in pancreas samples from T2D patients and non-diabetics. Studies into the changes in β-cell mass suggest that the reduction in mass is due to an increase in apoptotic mechanisms, and not a decrease in neogenesis or replication (Mezza *et al*., 2013).

The different observations in beta cell mass in the pathogenesis and progression of T2D mean more research should be aimed at the preservation of β-cell function, the regeneration of working β-cell mass, and the imaging of the β-cell mass (Steppel & Horton, 2004). Studies into developing imaging agents that can show (by MRI, PET, or fluorescence) insulin release, of β-cell mass, or Ca^{2+} mechanisms can help distinguish the changes in Diabetes Type 2 progression. Figure 1.6 below illustrates different receptors and cytosolic targets that have been a potential protein to image. The following subsections will elaborate on these targets.

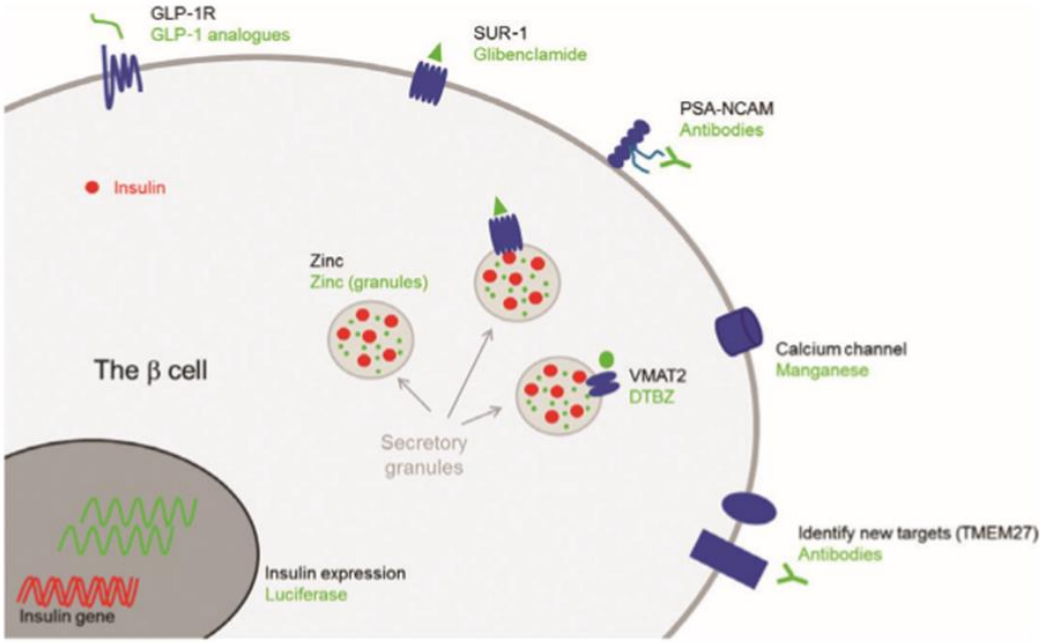

Figure 1.6: A diagram to illustrate the summarise the targets of the β-cell and corresponding imaging tracers (Laurent *et al*., 2016). The cellular targets are written in black font, alongside the corresponding imaging tracers/substances used to investigate them.

Key for abbreviations:
Glucagon-Like Peptide 1 Receptor (GLP-1R)
Sulfonylurea Receptor 1 (SUR-1)
Polysialylated modification of neural cell adhesion molecule (PSA-NCAM)
Vesicular Monoamine Transporter 2 (VMAT2)
Transmembrane Protein 27 (TMEM27)

1.7.1 Vesicular Monoamine Transporter 2

Vesicular monoamine transporter 2 (VMAT2) is responsible for the translocation of monoamines from the cytosol into the secretory granules and has a role in transporting neurotransmitters (Jodal *et al*., 2017). Pancreatic β-cell secretory granules express VMAT2 and are a target for PET and SPECT radiotracers (Jodal *et al*., 2017). VMAT2 is expressed on delta cells and PP cells in the Islets of Langerhans, so VMAT2 in itself is a less specific target for β- cell imaging (Jodal *et al*., 2017). Dihydrotetrabenazine (DTBZ) analogues target VMAT2 and compounds include ^{11}C-DTBZ, ^{18}F-FP-DTBZ, ^{18}F-FE-DTBZ, and ^{18}F-AV-133 (Laurent *et al*., 2016).

Specificity of some of these agents is inconsistent with studies conducted by Fagerholm *et al.* (2010) showing ^{11}C-DTBZ binds mostly to exocrine tissues of the pancreas. Specificity has also been a drawback in studies using ^{18}F-AV-133 with non-specific binding in β-cells in rats (Laurent *et al*., 2016).

1.7.2 Sulfonylurea Receptor 1

Sulfonylurea receptor 1 (SUR1) is a subunit of ATP dependent potassium (K^+) channels and is involved in insulin secretion (Jodal *et al*., 2017). SUR1 is located in the plasma membrane of the pancreatic Islet cell (Laurent *et al.,* 2016). Glibenclamide and Glipizide are T2D drugs and have been developed as radiolabelled compounds including ^{99m}Tc-DTPA-Glipizide, ^{99m}TC-Glibenclamide, and ^{18}F-Glibenclamide (Jodal *et al*., 2017).

1.7.3 Transmembrane Protein 27

Transmembrane protein 27 (TMEM27) is specifically expressed on the β- cell surface and kidney collecting ducts (Laurent *et al*., 2016). A study by Vats *et al.* (2012) used fluorescent and radiolabelled compounds to determine the specificity in β-cells. The results showed the tracers specifically were uptaken in pancreatic islets (co-localized with insulin staining) and hTMEM27 positive tumours, demonstrating the specificity for β- cells.

1.7.4 Zinc

GdDOTA-diBPEN is an MRI agent sensitive for Zn(II) reported by Lubag *et al*., (2011) and Esqueda *et al*. (2009). This compound showed improvement in the magnetic resonance images in the pancreas of mice and appeared to measure zinc co-secreted with insulin into the bloodstream (Hanaoka *et al*., 2004)

1.7.5 Glucagon-Like Peptide 1 Receptor

GLP1 binds to Glucagon-like peptide one receptor (GLP1-R). This receptor is expressed on the pancreatic β-cell, and the receptor belongs to a G-protein coupled receptor family (Wang *et al.,* 2014). Exendin-4, a GLP1-R agonist, and GLP-1 analogue is resistant to cleavage by dipeptidyl peptidase 4 (DPP4), displaying the same binding specificity as GLP-1 (Wang *et al*., 2014). Exendin-4 derivatives have therefore been developed for fluorescence and MRI of endogenous β- cells (Laurent *et al*., 2016).

One of these derivatives includes ^{111}In-DTPA-Lys^{40}-exendin-4 which binds explicitly to GLP1-R positive tissues in rats (Wild *et al.,* 2006). Another is ^{18}F-Al-NOTA-MAL-Cys(39)-exendin-4 developed by Mi *et al.* (2016). Their studies showed that ^{18}F-Al-NOTA-MAL-Cys(39)-exendin-4 uptake increased after 60 minutes and they concluded this agent might be suitable for pancreatic β-cell imaging. Other studies by Zhang *et al.* (2013) are demonstrating the use of nanoparticles, such as superparamagnetic iron oxide nanoparticles to target the GLP1-R. They have described the use of targeted superparamagnetic iron oxide (SPIO) nanoparticle using Exendin-4 which is conjugated to polyethene glycol-coated SPIO (PEG-SPIO). The results demonstrated that exendin-4 functionalized SPIO was able to specifically bind to and be internalised by GLP-1R-expressing INS-1 cells. Table 1.4 summarises results of clinical trials which have utilised the imaging of GLP-1 receptors.

Table 1.4: Summary of studies and the following findings in the utility of GLP1-R imaging

Investigated compound	Study Findings	Author(s)
[Lys^{40}(Ahx-DTPA-^{111}In)NH$_2$]Exendin-4	There is a high density of GLP1-R in insulinomas and high specific uptake of the compound	Wild *et al*. (2006)
[Lys^{40}(Ahx-DTPA-^{111}In)NH$_2$]Exendin-4	GLP1-R is a successful target for molecular imaging and therapy for insulinomas	Wicki *et al*. (2007)
[Lys^{40}(Ahx-DOTA-^{111}In)NH$_2$]Exendin-4	*In vivo* experiments showed GLP1-R imaging was successful in diagnosing small insulinomas pre and intraoperatively	Christ *et al.* (2009)
[^{125}I]BH-exendin(9-39)	Useful probe for pancreatic β-cell imaging	Mukai *et al.* (2009)
[^{64}Cu](Lys^{40}(DOTA)NH$_2$exendin-4	An active ligand for PET imaging in *vivo* imaging of β- cell mass	Connolly *et al.* (2012)
^{68}Ga-DO3A-exendin-4	Pancreatic uptake of this compound is decreased by selective destruction of β-cells	Selvaraju *et al.* (2013)

1.8 Magnetic Resonance Imaging

Magnetic resonance imaging (MRI) is a non-invasive imaging technique which can produce anatomical images of the body (Katti *et al.,* 2010). MRI uses signals from the nuclei of the hydrogen atoms in the human body to generate images. The nucleus of the hydrogen atom consists of one proton and one electron. The proton is positively charged, and the electron is negatively charged, resulting in the hydrogen atom overall is electrically neutral (Grand *et al*., 2012). The proton possesses a property called spin, and the proton nuclear spin rotates about its axis. As a rotating mass, the proton has angular momentum and wants to maintain spatial orientation of its rotation axis. As a rotating mass, with an electrical charge, there is also magnetic momentum. This means the proton behaves like a small magnet. In addition to this, the proton can be affected by external magnetic fields and electromagnetic waves (Weishaupt *et al*., 2008). Figure 1.7 represents the spins of protons in an external magnetic field.

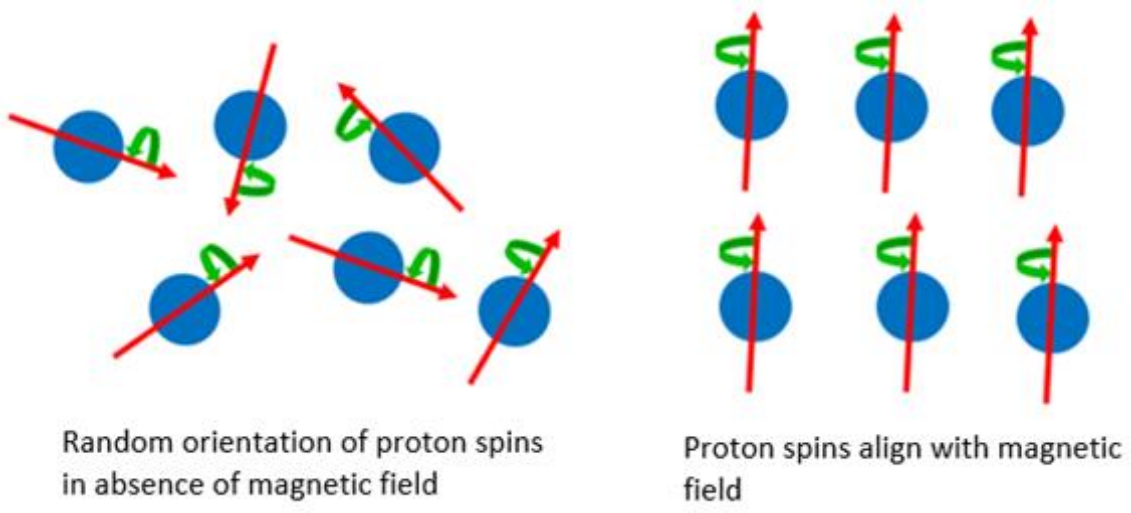

Figure 1.7: The orientation of protons spins when in absence or presence of an external magnetic field.

A proton's nuclear spin always has the same magnitude and therefore can neither be accelerated nor decelerated. When an external magnetic field is applied, the spins align with the direction of the field. Precession of the nuclei occurs at a characteristic speed that is proportional to the strength of the magnetic field applied (Grand *et al*., 2012). This is called the Larmor frequency. Energy can be introduced to a stable spin system by applying an electromagnetic wave of the same frequency of the Larmor frequency. The electromagnetic wave is generated in a radio transmitter and applied to the object of interest. The process of energy absorption is known as excitation of the spin (Weishaupt *et al*., 2016).

All of the longitudinal magnetisations is rotated into the transverse plane by the radiofrequency pulse by a radio frequency pulse that is strong enough and then applied long enough to tip the magnetisation by exactly 90°. Whenever transverse magnetisation is present, it rotates or precesses about the z-axis, which induces the alternating voltage of the same frequency of the Larmor frequency in a receiver coil. This signal is collected and processed to generate an MR image (Weishaupt *et al.,* 2016).

Immediately after excitation, the magnetisation rotates in the XY-plane and is now called transverse magnetisation. It is the rotating transverse magnetisation that gives rise to MR signal in the receiver coil (Weishaupt *et al*., 2016). The MR signal rapidly fades due to two independent processes: T1 relaxation and T2 relaxation. As transverse magnetisation decays, the longitudinal magnetisation is slowly restored (the projection of the magnetization vector onto the z-axis). This is longitudinal relaxation or T1. The nuclei can return to their ground state by dispersing their excess energy into the surroundings. The time constant for this recovery is T1 (Currie *et al*., 2012). Transverse or T2 relaxation is the decay of transverse magnetisation. Transverse relaxation differs from longitudinal relaxation because the spins do not disperse their energy but instead exchange energy with each other. Figure 1.8 illustrates the difference in T1 and T2 images in that they focus on different areas. Coherence is lost in two ways: energy transfer (between spins) and time-dependent inhomogeneities of the external magnetic field (Currie *et al*., 2012).

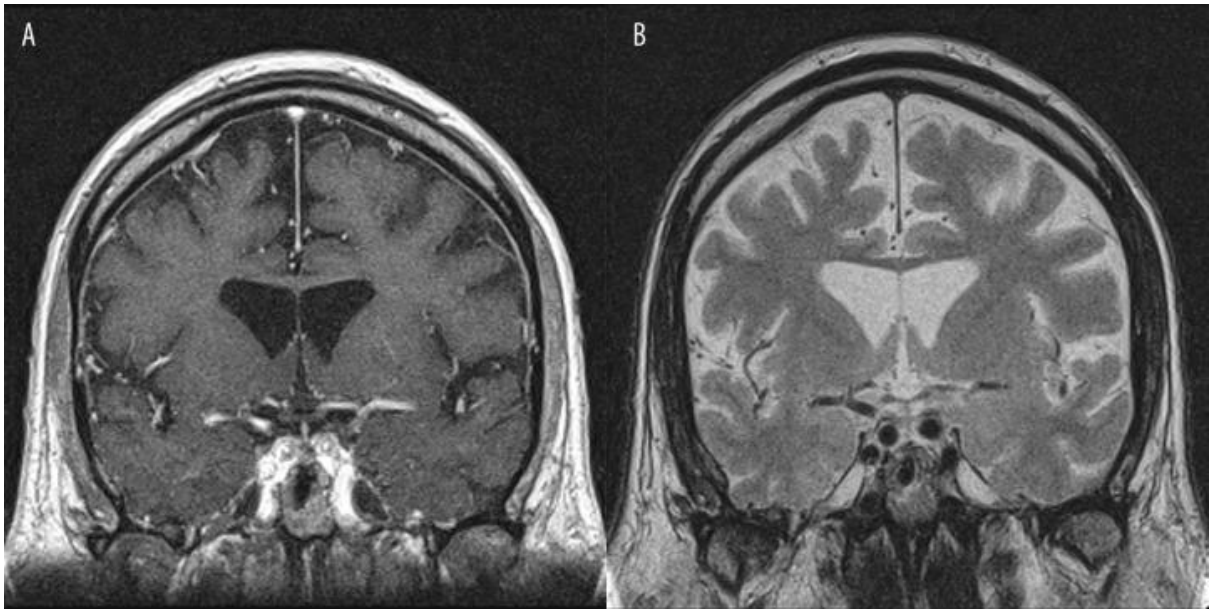

Figure 1.8: A) T1 weighted image post contrast of the brain, coronal plane. B) T2 weighted image pre-contrast of the brain, coronal plane (Bladowska *et al*., 2011)

Contrast agents are used in MRI to emphasise the contrast in images. MR contrast agents alter the intrinsic contrast properties of biological tissues by changing the local magnetic field or the resonance properties of a tissue.

The local magnetic field strength is altered due to the unpaired electron spins of the contrast agent interacting with the surrounding hydrogen nuclei of the water, protein, or fat molecules of the tissue. The mechanisms of the MR agent, therefore, compromise the processes of the electron shell (Nam *et al.,* 2014).

The majority of MRI contrast agents are either paramagnetic Gadolinium (Gd^{3+}) ion complexes or superparamagnetic Iron Oxide Magnetite particles. Paramagnetic contrast agents are usually formed with Dysprosium (Dy^{3+}) or Gadolinium (Gd^{3+}) or the transition metal Manganese (Mn^{2+}). Due to the presence of unpaired electrons, the following elements have paramagnetic properties; Gadolinium has seven, Dysprosium has four, and Manganese has five unpaired electrons (Xiao *et al*., 2016). Gadolinium-based contrast agents shorten T1 and T2 relaxation times of nearby water protons. However, these metal ions can cause tissue toxicity and to reduce that, chelation is used. One of the contrast agents, Gd-DOTA, (Gadoteric acid/Dotarem) is a macrocyclic structured Gadolinium-based MRI contrast agent. Consisting of DOTA as the chelating agent, this compound reduces the T1 relaxation time in MRI scanning. Gd-DOTA can be used for the imaging of blood vessels, vessels which are inflamed and those affected by disease, where the vessels become leaky (Xiao *et al.,* 2016). Figure 1.9 illustrates some of the Gadolinium-based contrast agents that are clinically used.

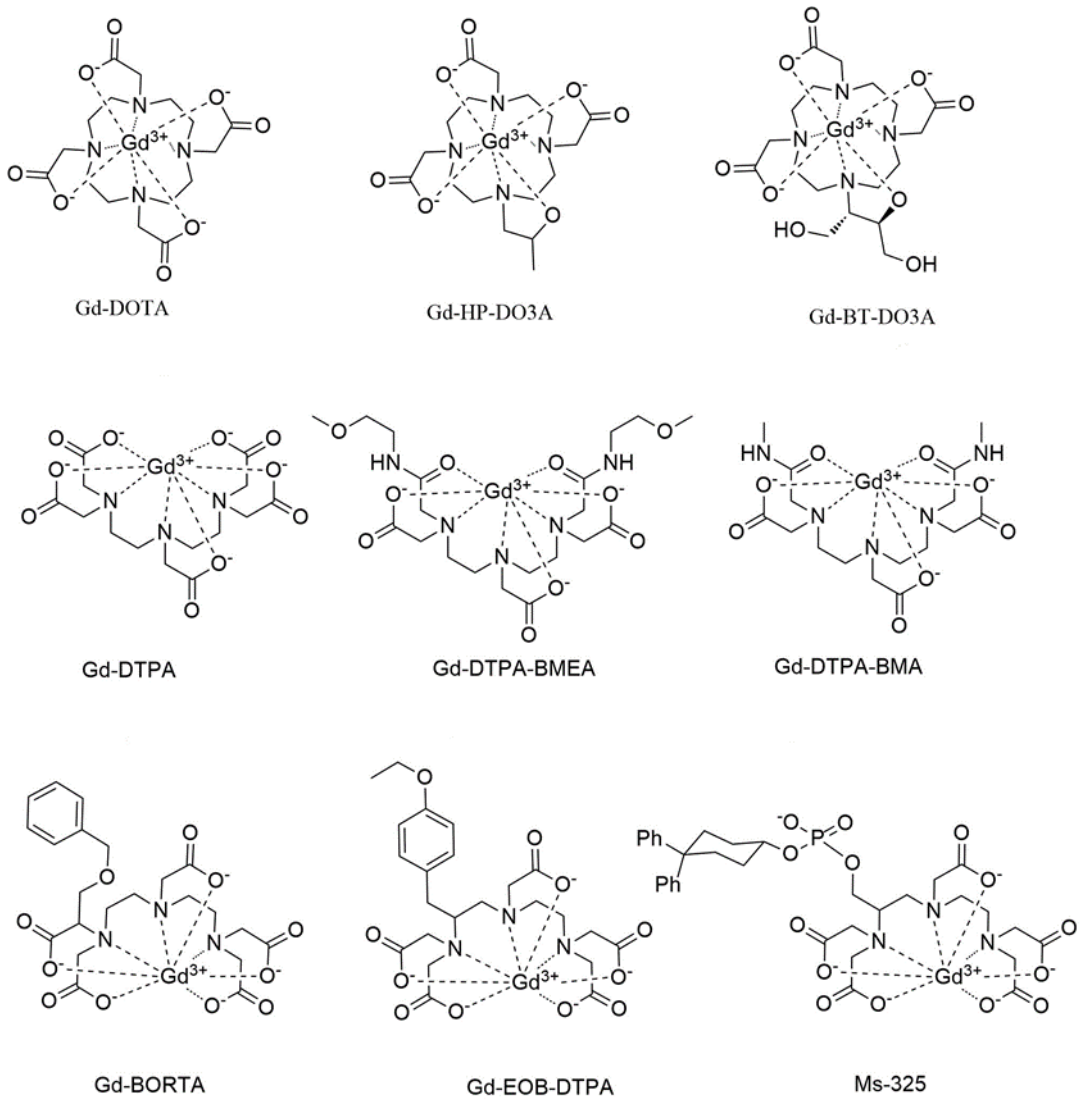

Figure 1.9: Clinically used Gadolinium-based contrast agents (Xiao *et al*., 2016)

There are several advantages and disadvantages of MRI. The technique is non-invasive, does not use radiation, which is advantageous. In addition to those, there is less chance of patients gaining an allergic reaction to the MR contrast agents. MR images can also large areas with clear images on soft tissue. MRI in itself, however, is expensive and cannot distinguish between benign and cancerous tissues (Nam *et al*., 2014)

1.9 Fluorescence Imagery

Fluorescence is a form of luminescence that involves excitation of electrons to a higher energy state as a result of photon absorption. During the excited state (S1) electrons lose energy and return to S0. The loss of energy results in the release of a low energy photon that has a longer wavelength than the absorbed photon (Combs, 2013). The Stokes shift is the gap between the maximum of the first absorption band and the maximum of the fluorescence spectrum.

Fluorescence imaging allows the visualisation of molecular structures and processes.

Fluorescence starts with a photon of energy (supplied by an external source) being absorbed by a fluorophore, creating an excited electronic singlet state (S1) (Bachmann *et al.,* 2006). S1 exists for a finite amount of time, during this time, the fluorophore undergoes interactions with its environment. Fluorescence emission occurs, a photon of energy is emitted, returning the fluorophore to its ground state (Bachmann *et al*., 2006). Due to energy dissipation, the energy of the photon is lower than the excitation photon. The difference in energy or wavelength is referred to as the Stokes shift (Bachmann *et al*., 2006). A Jablonski diagram (as seen below, labelled as Figure 1.10) is classically used to illustrate the physics and stages of fluorescence.

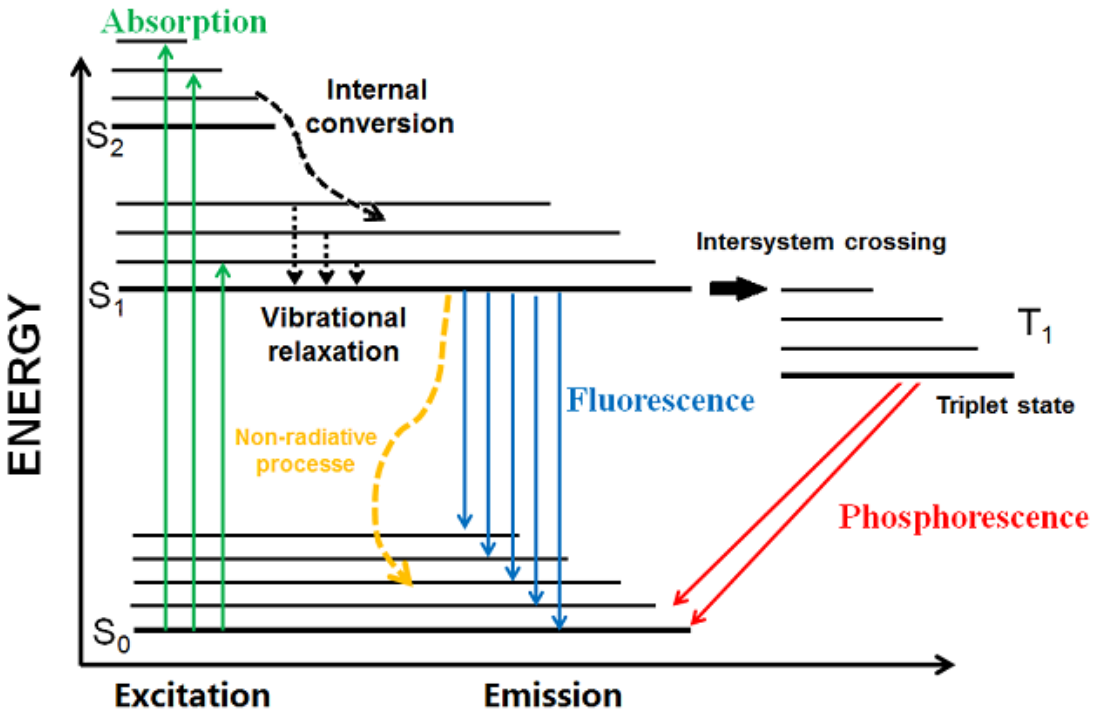

Figure 1.10: A simplified Jablonski diagram showing the electronic states of a given molecule that results in fluorescence (Institut de Biologie Structurale, 2018)

1.10 Quantum Dots

Quantum dots (QD's) are semiconducting nanomaterials that show electronic and optical properties. These properties include size-tunable light emission, simultaneous excitation of multiple fluorescence colours, high signal brightness, long-term photostability, and broad absorption and excitation spectra (Jin *et al*., 2011). Quantum dots have semiconductor cores (e.g. Se, Cd, InP) and surrounded by a semiconductor shell (e.g. ZnS). The addition of this shell improves their optical properties (Barroso, 2011). There are two types of quantum dots: Type I and Type II.

Type I quantum dots have charge carriers that are confined to the core of the particle, by large band offsets of both the conduction and valence bands of shell material.

Type II quantum dots have separation of excited electrons and holes into either the core or shell by a staggered band structure (Tytus *et al*., 2008)

Quantum dots show advantages over fluorescent dyes (Barroso, 2011). Firstly, they have tuneable core sizes of approximately 1-10nm, which means they generate a wide range of fluorescent emission peaks. Secondly, quantum dots show wide-ranging absorption patterns (Barroso, 2011). Lastly, quantum dots are more photostable (Barroso, 2011). Quantum dots have been utilised in various biological applications including *in vivo* Imaging. Many quantum dots are synthesised using Cadmium, despite its toxicity. Alternatives include $CuInS_2$ or InP.

Quantum dots in biological applications show more advantages compared to fluorophores and fluorescent proteins. Quantum dots are more photostable and with strong fluorescence. Also, their broad excitation and narrow emission spectra make it easy for several wavelengths and colours to be investigated in a given experiment (Mo *et al*., 2017). In fixed cells, they can show strong fluorescence, but limitations can be seen in live cells as quantum dots tend to accumulate in living cells or be detected by endocytic vesicles (Smith *et al*., 2008). Cells also tend to endocytose quantum dots in an unspecific manner, meaning specific receptor targeting can be difficult (Deng *et al*., 2013).

Recent application of quantum dots has been in *in vivo* imaging of tumours. The application is difficult as the quantum dot needs to be sensitive, other concerns are that quantum dots over 6nm have been observed as not suitable for lymphatic drainage (Ji *et al*., 2014). Despite tumours having blood vessels that are leaky by nature, this observation could mean tumour staging or the full extent of tumour progression is not observed.

Cadmium QD'S are easily synthesised but show toxicity, so there is a concern for using them in biological applications. For example, Cd^{2+} has been reported to be released from the quantum dot during oxidation and endocytosis into the cell, which contributes to the generation of reactive oxygen species.

Cd^{2+} can bind to sulfhydryl groups on many intracellular proteins, leading to the reduced functionality in various subcellular organelles (Wang *et al*., 2014). Cd^{2+} toxicity has also been observed in human fibroblasts and tumours when using CdSe/ZnS quantum dots (Wang *et al*., 2014).

1.11 Multimodal Imaging

MRI has an excellent anatomic resolution but lacks specificity in cells. To combat this, a high concentration of contrast agent would have to be used but at the molecular levels, targets present at much lower levels (pico-nanomolar) (Stasiuk *et al*., 2015). Another approach is to combine medical imaging techniques (e.g. MRI, PET) with high sensitivity modality like fluorescence which creates a multimodal approach. These probes can target different proteins, molecules, or pathological processes in a given disease. This is done primarily by functionalising the agent with specific proteins that bind to the molecules of interest.

For example, Huang *et al.* (2018) have described the use of a Glypican-1 (GPC-1) antibody conjugated with Gadolinium-Gold nanoparticles. GPC-1 is expressed in pancreatic cancer, and this study showed with confocal imaging and flow cytometry that the probe could successfully detect the expression of GPC-1. Furthermore, higher MR signals were shown in the pancreatic cancer cell lines that express GPC-1 compared with HEK-293T. Moreover, the probe could effectively detect pancreatic cancer cells *in vivo* by dual-modal fluorescence imaging/magnetic resonance imaging at 30 minutes post-injection. The sensitivity of this probe was demonstrated in the study because MR imaging could determine the presence of the probe in the cells, but the fluorescence imaging could show the probe was targeting the cell membrane of the cells. Other multimodal imaging agents aim to target specific elements which are known to contribute to biological processes, for example, Zinc or Fluorine.

1.12 Aims of the project

This Master's project aims to develop a multimodal imaging fluorescent/MRI agent to image the β-cell mass in the pancreas. This agent will be formed by functionalising the surface of fluorescent red and yellow emitting quantum dots with Exendin-4 for targeting of the GLP1 receptor and Gd-DOTA-TA for MRI. This project will aim to determine the characteristics of the agent. Also, cellular studies aim to give results into the cell viability of the multimodal agent and as to whether the agent enters the cell with specificity.

2.0 Materials and Methods

2.1 Probe Synthesis

2.1.1 Quantum dot phase transfer

Mitchell Clarke and Michelle Kinnon synthesised all Quantum dots used for this project (see acknowledgements). Quantum dots were provided in Hexane, and from this, they could be taken into the water using phase transfer. To do this, 1ml of the quantum dot was added to 3ml of ethanol and vortexed. After this, 1ml of this was added to 4 Eppendorf tubes and spun in a centrifuge at 13.3 rotations per minute (rpm) for 3 minutes. The ethanol waste was then removed from the Eppendorf's. A 3:1 of ethanol and chloroform solution was made, and 1ml of this was added to the 4 Eppendorf's. They were span again at 13.3rpm for 3 minutes. After this, the waste was removed, and 1ml of chloroform was added to each Eppendorf. A 70% Thioglycolic acid (TGA, 0.2M) solution was made, and 200µl of this was used to create a solution with a total volume of 10ml, using water. This solution was then degassed under Argon for approximately 20-30 minutes.

When the solution had been degassed, 1ml of the quantum dots in chloroform was added to 2ml of the TGA solution. 50µl of Tris(2-carboxyethyl)phosphine (TCEP, 0.5M) was then added. The pH was adjusted to 10.5 using Tetramethylammonium hydroxide (TMA-OH). The quantum dots were then spun on a heated magnetic plate at 1500rpm until the quantum dots went into the water layer, creating two distinct layers. The top layer was then separated equally into 30KDa filtered Eppendorf's as well as 50µl of water. The filtered Eppendorf's were then spun at 1300rpm for 3 minutes. 100µl of water was added, and the quantum dots were resuspended and then spun at 1300rpm for 3 minutes. This process was repeated a further 2 or 3 times to wash the quantum dots and remove any waste fully. After the last spin cycle, the quantum dots were then resuspended into 1ml of water and were ready to use.

2.1.2 Quantum dot functionalisation

Quantum dots were functionalised with either Exendin-4, Gd-DOTA-TA, or both Exendin-4 and Gd-DOTA-TA. A custom Exendin protein was purchased from Cambridge Research Biochemicals Limited ([Cys]-Exendin 4 ([C]-HGEGTFTSDLSKQMEEEAVRLFIEWLKNGGPSSGAPPPSamide) to be functionalised with quantum dots. The protein was prepared at a 1M stock by dissolving it in 233µl of DDH_20. This stock was then aliquoted into Eppendorfs and frozen ready for use.

In a filtered Eppendorf tube, the quantum dot was combined with Exendin (1M) or Gd-DOTA-TA (0.01M) with the addition of 200µl of water. 20µl of TCEP was added, and The pH was then adjusted to between 9-10 using Tetramethylammonium hydroxide (TMA-OH). One half of this solution was placed into two separate filtered Eppendorf tubes and diluted with water. These were spun at 13.3 rpm for 10 minutes. The solution in each tube was resuspended in water and spun at 13.3 rpm for a further 10 minutes. Again, the solution in each tube was resuspended in water and spun at 13.3 rpm for a further 10 minutes. The solution was again resuspended in water, spun, and the contents of the two filtered Eppendorf tubed were combined. For the quantum dot that was functionalised with Exendin and Gd-DOTA-TA, the Gd-DOTA-TA was functionalised first then a second step was added to functionalise the quantum dot with the Exendin. The concentration of the following solution was determined by UV Vis.

2.1.3 Photophysics

Fluorescence excitation and emission experiments were done on the Fluromax-4 spectrofluorometer. The functionalised quantum dots and quantum dots in water were analysed. An emission/excitation experiment was selected, and samples were loaded into the machine. Equation settings were adjusted (S1/R1), and the experiment was run. Data was smoothed and plotted using GraphPad Prism.

2.1.4 UV Vis

The UV Vis spectrophotometer was used to determine concentrations of the functionalised quantum dots and quantum dots in water and to show absorption. A blank sample of water was first run to create a baseline. After this, samples were prepared in a 1:8 ratio with water to be run. Each data set was plotted alongside the photophysics data on GraphPad Prism.

2.1.5 Dynamic Light Scattering (DLS) and Zeta potential

DLS was conducted to determine the size change in functionalised quantum dots compared to the quantum dots in water. Zeta potential readings were undertaken to determine the surface charge of the functionalised quantum dots compared to the quantum dots in water. Samples were run on the DLS Machine, and a Zeta potential cell was required for the Zeta readings. For the DLS readings, 10 µl of sample was added to 100 µl of water in a disposable plastic cuvette. The settings were set so that InP was the core material of the nanoparticle. The sample was placed in the machine, and several readings were taken, an average was then generated alongside a graph. The results were then saved, and readings could be reported appropriately. For the Zeta readings, the samples were prepared the same in separate cuvettes, and a Zeta potential cell was placed inside the cuvette. The settings were changed to allow the machine

to read the potential. The sample was placed in the machine, and several readings were taken, an average was then generated alongside a graph. This was then saved, and readings could be reported appropriately.

2.2 Cell Culture

2.2.1 Cell Lines

The human embryonic kidney cells (HEK293) and the pancreatic β-cells (MIN6) used in the project were purchased externally (from ECACC) or donated. HEK293 cells were cultured in Dulbecco's modified Eagle Medium (DMEM; Lonza) and were supplemented with 10% Fetal Bovine Serum (FBS; Lonza), 1% Penicillin/Streptomycin (P/S; Gibco) and 1% Glutamine (Lonza). MIN6 cells were cultured in DMEM and were supplemented with 15% FBS, 1% P/S, 1% Glutamine, 50µmol of β- mercaptoethanol (Fluka) and 1% of HEPES.

2.2.2 Use of Class II Biological Safety Cabinet

The class II biological safety cabinet is used to create a sterile environment for samples to be taken into and subsequently tested. To protect the laboratory worker and biological samples, tissue culture laboratory coats and nitrile gloves are worn when performing experiments. Before the use of the cabinet, the surfaces inside were cleaned with disinfectant then 70% ethanol. 70% ethanol was also applied to any materials that were required within the cabinet to ensure they were sterile.

A container of 1% Virkon solution was used to dispose of waste. After work was complete within the hood, all equipment and waste were removed. The biosafety hood was again cleaned with disinfectant then 70% ethanol. Any waste material from the hood was disposed of appropriately.

2.2.3 Cell Passaging

Media and Trypsin-EDTA were placed in the water bath at 37°C. The biosafety hood was prepared as described in section 2.2.1. Before cells were passaged, cells were observed under the microscope to assess their confluency percentage. Cells were passaged at 80-90% confluency. When cells had reached the required confluency, flasks were transferred to the biosafety hood. Spent media in the flasks were removed and discarded. The cells were then washed twice with Phosphate Buffer Saline (PBS) and then Trypsin-EDTA was added. The flask was incubated for 5-10 minutes in the incubator at 37 °C, 5% CO_2. Cells would be observed under the microscope to confirm the cells had fully detached. On confirmation of this, a small amount of medium was added to deactivate the trypsin, creating a cell suspension.

In separate 75ml culture flasks (Sarstedt), 30ml of fresh media was added, and the cell suspension was added to the new flasks at the appropriate volume to ensure the correct splitting ratio (typically 1:8 for HEK293, 1:4 for MIN6). The cells were then placed into the incubator (37 °C and 5% CO_2) until they reached 80-90% confluency.

2.2.4 Cell Counting

A haemocytometer (also known as a counting chamber) is a slide used to determine the concentration of cells in a sample of cells. A grid on the glass of the haemocytometer is designed to make the counting of cells more accurate. The full grid design can be seen in Figure 2.1 below.

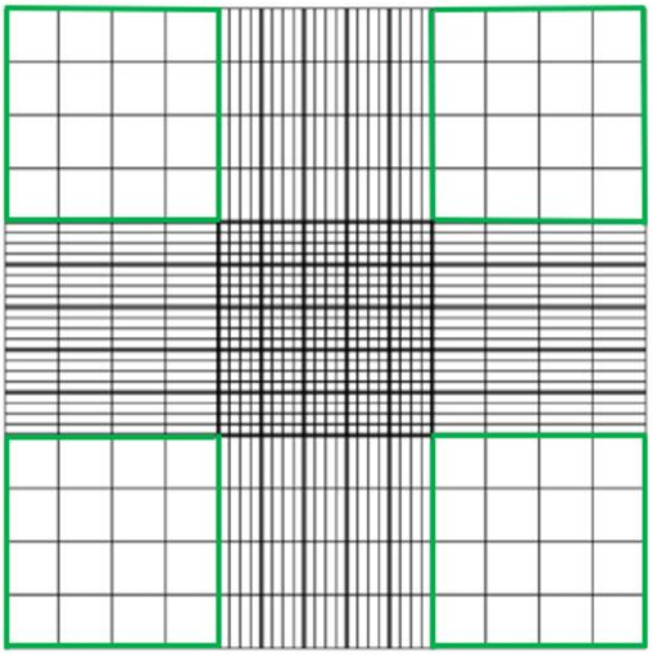

Figure 2.1: The design of a haemocytometer grid. The green highlighted corners are the corners of which cells are counted.

Before use, the haemocytometer was cleaned with 70% ethanol. A coverslip was then fixed on top of the haemocytometer grid. In an Eppendorf tube, a 1:1 ratio of cell suspension and 0.2% Trypan Blue was made. 10µl of this solution was placed underneath the coverslip. The haemocytometer was then put under the microscope at X20 magnification, and all cells present in all four corners (highlighted in figure 2.1) were counted. An average number of cells was calculated by adding up the totals of all four corners. This number is then multiplied by 2 to account for the volume of Trypan Blue added.

This number is then multiplied by $1x10^4$ to gain cells per ml (cells/ml). The volume of cells to be added was calculated by dividing the number of cells needed by the number of cells present.

2.2.5 Freezing cells for liquid Nitrogen storage

Cells that were not required for immediate use were prepared and stored in Liquid Nitrogen. Before cell preparation, the biosafety hood was prepared as described in section 2.2.1. Once cells had reached 80-90% confluency, the cells were trypsinised as described in section 2.4.1 to create a cell suspension. Once the cell suspension was formed, this was centrifuged for 5 minutes at 1700rpm. The supernatant was discarded , and cell freezing media was then created at a 1:10 ratio (1ml of Dimethyl sulfoxide (DMSO): 9ml of FBS). The cell pellet was then resuspended in the cell freezing media. Once resuspended, the cells in cell freezing media were added equally to cryogenic vials. The cryogenic vials were then placed to a container which holds Isopropanol and stored at -80°C overnight. After this, the cryogenic vials could then be placed into liquid nitrogen and then used when required.

2.3 Cell Viability

MTS assays were conducted to determine the cellular viability for multimodal imaging agent and individual compounds. An MTS assay is a colourimetric assay which measures the quantification of cells in proliferation. The assay is based on the reduction of MTS tetrazolium by NADPH dependent dehydrogenase enzymes in mitochondria of viable cells. This generates a purple coloured formazan product which can be quantified. Cells were trypsinised as described in section 2.4.1 and cells were counted as described in 2.4.2 to achieve 20,000 cells per well/105,000 cells/ml. 190µl of cell suspension was added alongside 190µl of PBS into three 96 flat well-bottomed plates. The plates were placed in the incubator (37 °C and 5% CO2) for 24 hours to allow the cells to adhere. Figure 2.2 below shows how the cells were distributed on the 96 well plates.

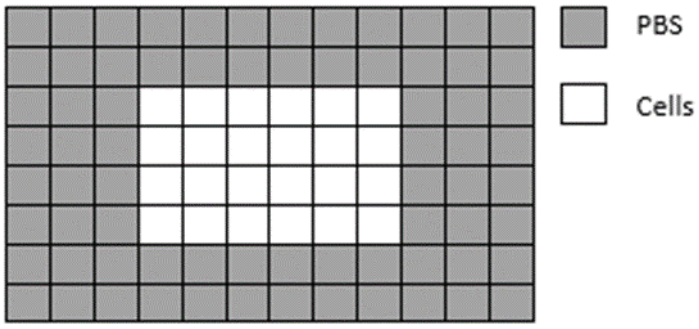

Figure 2.2: A diagram to denote how the cells and PBS were distributed on a 96 well plate. The white sections represent wells that contained cells, and the grey sections represent wells that contain PBS.

After incubation of the cells, 90µl of the cells media was removed, and treatments were added to the cells. The treatments added are shown in Table 2.1. After the treatments were added, the plates were incubated for 24 hours in the incubator (37 °C and 5% CO2). After incubation of the treatments, all contents of the wells were removed. 20µl of MTS solution was added alongside 180µl of PBS directly into the wells. The plates were incubated for 2 hours. After this, the plates were recorded by a BIO-TEK Synergy HT plate reader at 490nm. Data was exported in maximum optical density (MAX OD) form.

Table 2.1: The amounts of stock and media that were added to each well in an MTS assay.

Stock A					
100 µl stock A 100 µl media	50 µl stock A 150 µl media	25 µl stock A 175 µl media	10 µl stock A 190 µl media	5 µl stock A 195 µl media	2 µl stock A 198 µl media
100 µl stock A 100 µl media	50 µl stock A 150 µl media	25 µl stock A 175 µl media	10 µl stock A 190 µl media	5 µl stock A 195 µl media	2 µl stock A 198 µl media
100 µl stock A 100 µl media	50 µl stock A 150 µl media	25 µl stock A 175 µl media	10 µl stock A 190 µl media	5 µl stock A 195 µl media	2 µl stock A 198 µl media
100 µl stock A 100 µl media	50 µl stock A 150 µl media	25 µl stock A 175 µl media	10 µl stock A 190 µl media	5 µl stock A 195 µl media	2 µl stock A 198 µl media
Stock B					
100 µl stock B 100 µl media	50 µl stock B 150 µl media	25 µl stock B 175 µl media	10 µl stock B 190 µl media	5 µl stock B 195 µl media	2 µl stock B 198 µl media
100 µl stock B 100 µl media	50 µl stock B 150 µl media	25 µl stock B 175 µl media	10 µl stock B 190 µl media	5 µl stock B 195 µl media	2 µl stock B 198 µl media
100 µl stock B 100 µl media	50 µl stock B 150 µl media	25 µl stock B 175 µl media	10 µl stock B 190 µl media	5 µl stock B 195 µl media	2 µl stock B 198 µl media
100 µl stock B 100 µl media	50 µl stock B 150 µl media	25 µl stock B 175 µl media	10 µl stock B 190 µl media	5 µl stock B 195 µl media	2 µl stock B 198 µl media
Stock C					
100 µl stock C 100 µl media	50 µl stock C 150 µl media	25 µl stock C 175 µl media	Cells No Stock 200 µl media	Cells 100 µl stock B No Media	No cells, no stock, 200µl MTS
100 µL stock C 100 µl media	50 µl stock C 150 µl media	25 µl stock C 175 µL media	Cells No Stock 200 µl media	Cells 100 µl stock B No Media	No cells, no stock, 200µl MTS
100 µL stock C 100 µl media	50 µl stock C 150 µl media	25 µl stock C 175 µl media	Cells No Stock 200 µl media	Cells 100 µl stock B No Media	No cells, no stock, 200µl MTS
100 µL stock C 100 µl media	50 µl stock C 150 µl media	25µl stock C 175 µl media	Cells No Stock 200 µl media	Cells 100 µl stock B No Media	No cells, no stock, 200µl MTS

2.4 Cell characterisation

2.4.1 FACS Analysis

A flask of cells at 80% confluency was trypsinised (as described in 2.2.3 and 2.2.4), and then the cell suspension was pelleted at 1700rpm for 3 minutes. The pellet was then resuspended in 1ml of PBS. 50 µl of cell suspension was placed into two FACS tubes. 5µl of the primary antibody (Human GLP-1R Alexa Fluro 488-conjugated antibody, R&D Systems) was added to one tube, and five µl of negative control antibody (Mouse IgG2B Alexa Fluro 488-conjugated Isotype Control, R&D Systems) was added to another tube and left in a dark room at room temperature for 30 minutes. After this, 1ml of PBS was added to each tube and centrifuged at 400 g for 3 minutes. The supernatant was discarded, and the cell pellet was resuspended in 300µl of PBS and then ran on the FACS machine.

2.4.2 Confocal Imaging

To study the effects of the imaging agent in the two cell lines used in this project, cells were prepared and imaged under confocal microscopy. Confocal dishes from IBIDI (35mm 4 chamber confocal dishes. CAT# 80416) were used to seed the cells in. Cells were grown to 80% confluency (as described in 2.2.3), and when they achieved this confluency, cells were trypsinised and counted (as described in 2.2.4) to produce 150,000 per chamber. Each chamber of the dish was filled with 400µl of cell suspension and left in the incubator overnight (at 37 °C and 5% CO_2). After incubation, cells were observed under the microscope to observe the amount of cells, if the space of the chamber was not fully covered, cell media was refreshed, and the dishes were placed again overnight into the incubator. Once cells had covered the chamber surface, they were washed once with X1 PBS. Quantum dot and media was then added at given times points. After incubation of quantum dot all contents was removed, and cells were washed with X1 PBS. Cells were then fixed with Formalin and excess washed away with X1 PBS. Confocal dishes could then be imaged by confocal microscopy with Zeiss software.

3.0 Results and Discussion

The aim of this project is to develop a multimodal imaging probe which uses fluorescent quantum dots and the MRI contrast agent, Gd-DOTA-TA, to image the β-cell mass in the pancreas. This probe was developed by functionalising the surface of red (607 nm) or yellow (570 nm) fluorescing quantum dots with Exendin-4 and Gd-DOTA-TA. As previously described, Exendin-4 is an agonist of the GLP-1R receptor, which is expressed on the surface of the β-cells in the pancreas. Exendin-4 is therefore utilised to enable specific targeting to the β-cell. Quantum dots (QD's) are semi conducting nanoparticles that show size dependent optical and electronic properties that can be easily tailored, and because of this, they have been used to develop for biomedical imaging purposes (Reiss *et al*., 2016). However, QD's are often used that contain toxic metals (e.g Cd^{2+} or $Pb2^{+}$) which has caused some concern on the toxicity and tissue exposure of these specific type of QD's (Reiss *et al*., 2016). InP/ZnS QD's have been shown to be less toxic *in vivo* when histological and haematological examinations have been done in tissues in different species (Lin *et al*., 2014). Because of these findings, InP/ZnS QD's were used in this project. InP/ZnS QD's were provided (see acknowledgements) in Hexane. Since Hexane is toxic and not miscible with aqueous media, phase transfer was conducted (as described in section 2.1.1), and then aqueous QD's were functionalised (as described in 2.1.2). The Schematic below illustrates this. The following QD probes were validated physically, within cells, and through cell viability studies.

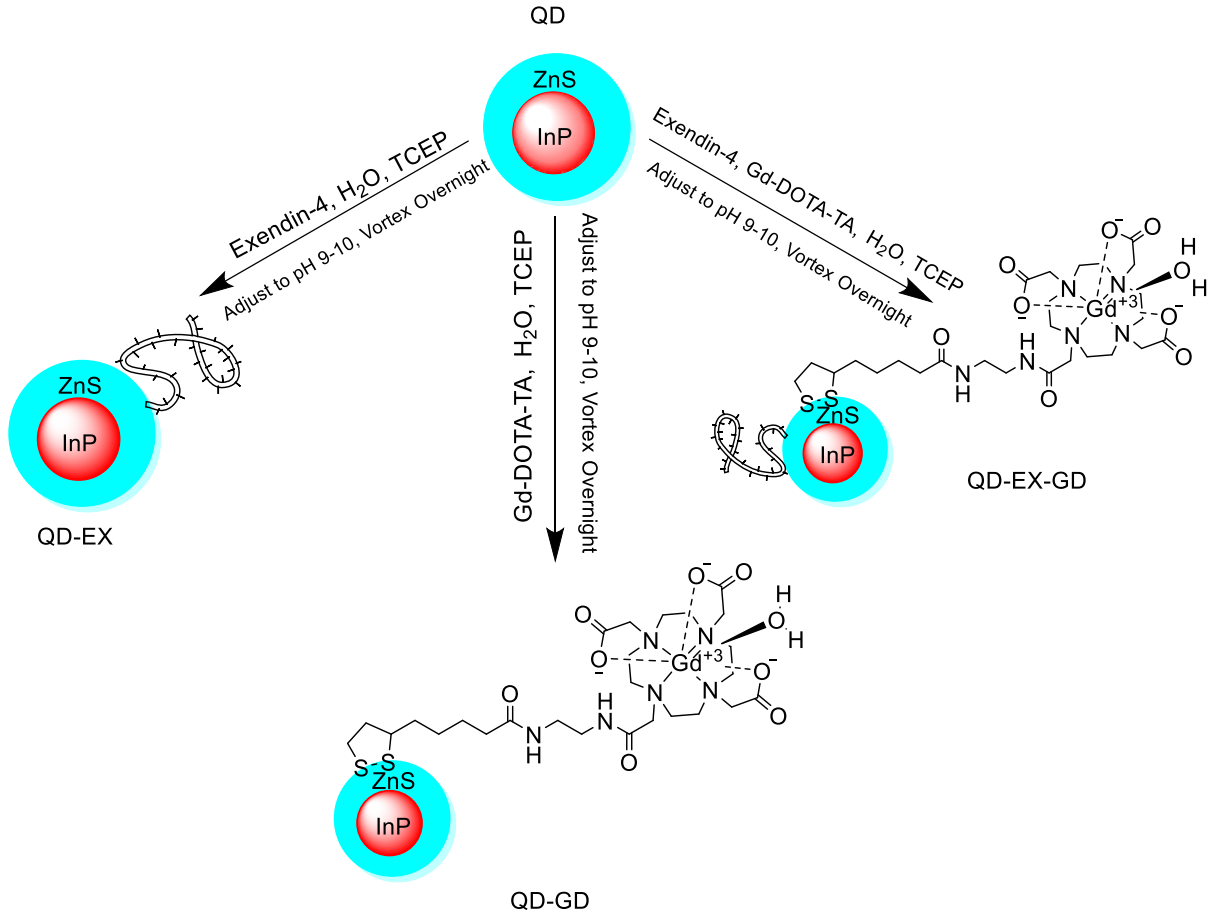

3.1 Probe Synthesis and Characterisation

As previously mentioned, QD's of between 2.5 nm and 2.75 nm diameter were provided in Hexane and phase transfer using thioglycolic acid (TGA) as a water solubilising surface ligand, had to be conducted in order for the QD'S to be in water, and therefore they could be used for biological testing (as described in section 2.1.1). The concentration of the Hexane used was $5x10^{-6}$M and this had to be removed during the washing process of phase transfer. QD's were then functionalised (as described in section 2.1.2) and washed in order to concentrate the compounds. Figure 3.1.1 shows the photophysical properties of the QDs capped with TGA in water. They are excited at 400 nm and emit at 607 nm, this is a characteristic stoke shift for InP/ZnS QDs. The concentration is determined from the first excitonic peak, (UV-vis spectra blue line) at 520 nm. It was found that after phase transfer the concentration of QD was $3.22x10^{-6}$ M, this is a 64% conversion, this loss of QD is due to the harsh basic conditions of the phase transfer reaction (pH 11) this can degrade the QD structure.

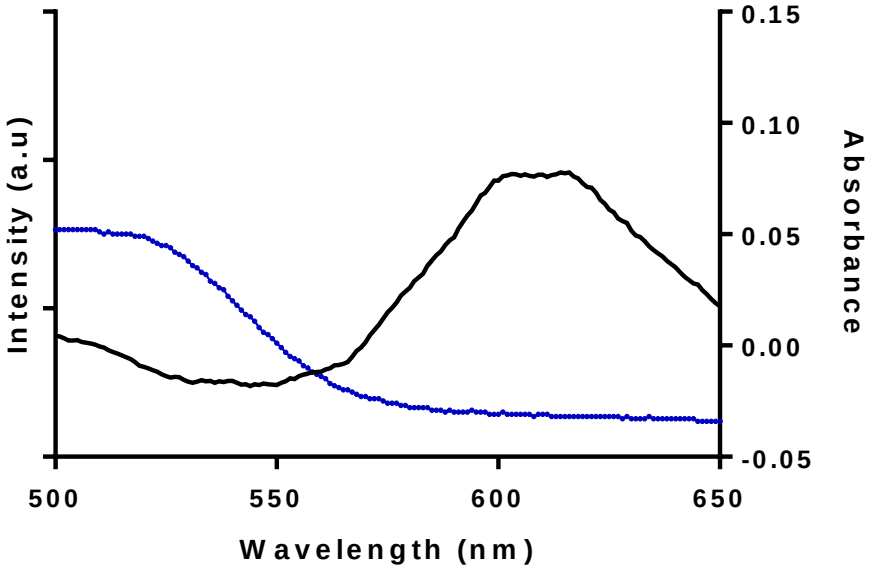

Figure 3.1.1: The absorption (represented by the blue line) and the emission (represented by the black lines) of the red fluorescing InP/ZnS quantum dots. The excitation wavelength of the QD's is 400 nm and emission at 607 nm with a concentration of 3.22×10^{-6} M, (H_2O, pH 7.4, 298K).

Once in an aqueous solution, the QDs can be functionalised with either Exendin-4 for targeting, Gd-DOTA-TA for MRI or both to create a targeted multimodal contrast agent. Functionalisation with Exendin-4 has been done using a modified Exendin-4 with an extra cysteine residue at the C terminus. This allows for a Thiol unit to bind to the ZnS surface of the QD. The reaction occurs overnight at pH 10 to deprotonate the Thiol, with excessive TCEP to reduce any Dithiol bonds formed in solution. Figure 3.1.2 shows the photophysical properties QD's functionalised with Exendin-4 the emission maxima does not shift showing functionalisation does not affect fluorescence emission, and the concentration was shown to be 3.11×10^{-7} M which is tenfold lower concentration than the Red QD's in water, showing that functionalisation with Exendin-4 has not been very efficient. This is possibly due to aggregation during the washing process or again the high basic condition of the functionalisation process.

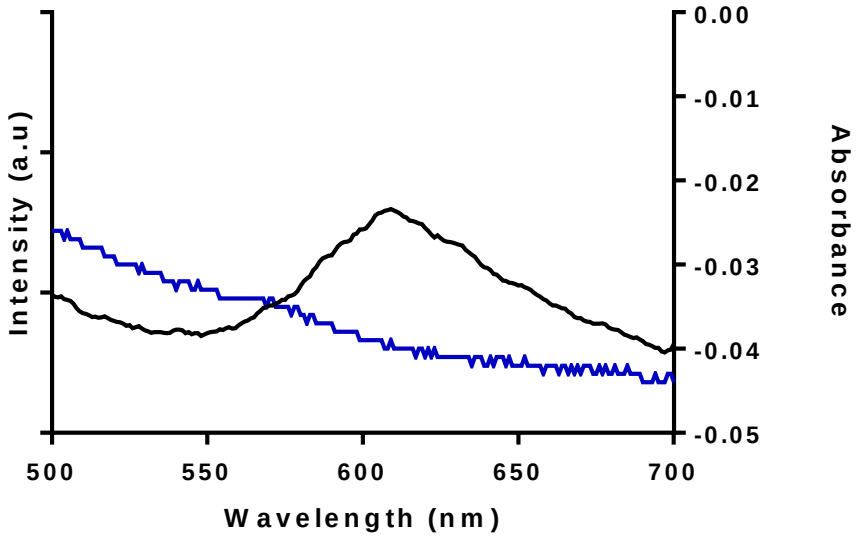

Figure 3.1.2: The absorption (represented by the blue line) and the emission (represented by the black lines) of the red fluorescing InP/ZnS quantum dots functionalised with Exendin-4. The excitation wavelength of the QD's is 400 nm and emission at 607 nm with a concentration of 3.11×10^{-7} M. (H_2O, pH 7.4, 298K).

To create a dual-modal MRI/optical probe, the QDs were surface functionalised with Gd-DOTA-TA, which is a Dithiol appended Gd-DOTA based complex. The Di-thiol unit is used to coordinate to the Zn of the ZnS surface on the QD. TCEP is used to reduce the Dithiol bond to allow for an S-Zn bond from the Gd-DOTA-TA to the Zn of the QD surface. Figure 3.1.3 shows the photophysical properties QD's functionalised with Gd-DOTA-TA the emission maxima does not shift showing functionalisation does not affect fluorescence emission and the concentration was shown to be 3.422×10^{-6} M which suggests a quantitive conversion from the Red QD's in water, showing that functionalisation with Gd-DOTA-TA has not affected the QD. This has created a stable dispersion of QDs in the solution that do not aggregate as readily as the QD-Exendin-4.

To produce the targeted multimodal contrast agent both Exendin-4 and Gd-DOTA-TA were functionalised in a one-pot reaction to the surface of the QDs. Figure 3.1.4 indicates that the QD's functionalised with Exendin-4 and Gd-DOTA-TA was at a concentration of 8.16×10^{-7} meaning a large proportion of QD has been lost during the washing process.

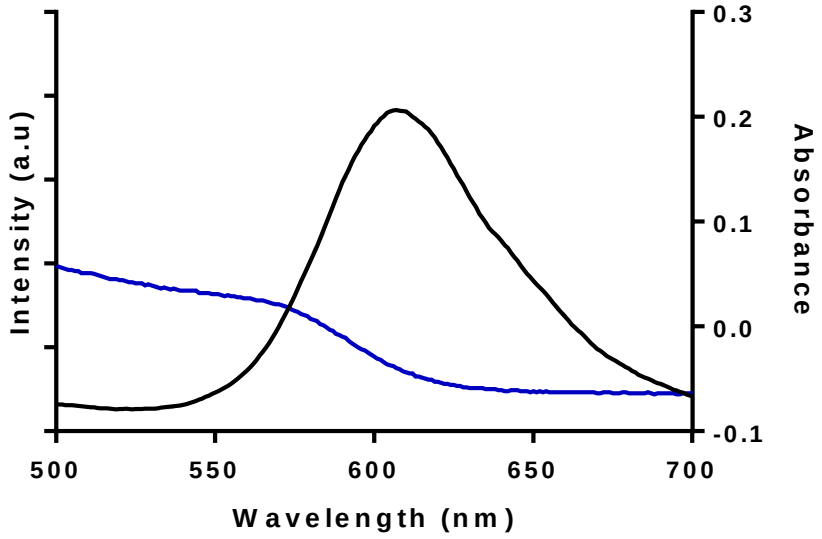

Figure 3.1.3: The absorption (represented by the blue line) and the emission (represented by the black lines) of the red fluorescing InP/ZnS quantum dots functionalised with Gd-DOTA-TA. The excitation wavelength of the QD's is 400 nm and emission at 607 nm with a concentration of 3.422×10^{-6} M. (H_2O, pH 7.4, 298K).

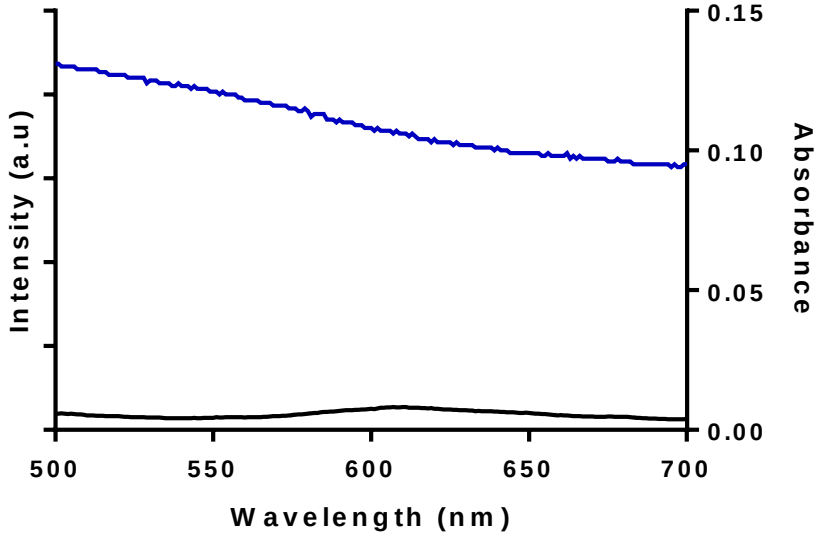

Figure 3.1.4: The absorption (represented by the blue line) and the emission (represented by the black lines) of the red fluorescing InP/ZnS quantum dots functionalised with Exendin-4 and Gd-DOTA-TA. The excitation wavelength of the QD's is 400 nm and emission at 607 nm with a concentration of 8.16×10^{-7} M. (H_2O, pH 7.4, 298K).

After QD's were functionalised, the absorption and the emission profiles were taken as seen in Figures 3.1.1-3.1.4 and in addition to that, Dynamic Light Scattering (DLS) and Zeta potential (Zeta) measurements were taken. DLS is a technique that determines the size distribution of nanoparticles in solution or the hydrodynamic diameter. The larger particles indicate that more components are on the surface of the nanoparticle or there are larger aggregates. The Zeta potential determines the charge of the surface of the nanoparticle and this charge has effects on how they interact and uptake mechanisms with cells. Changes in these will indicate that the surface of the QDs will have been functionalised. The full graphs and readings are shown in the Appendix.

Table 3.1.1 shows the DLS and Zeta potential values obtained of the QD's and the functionalised QD's in addition to the r1 value of QD-Gd-DOTA-TA. InP/ZnS represent the value for the QD in the table shows a value of 89.30 nm and -27.6 mV. The Zeta potential shows a negative value due to the capping agent used in the phase transfer, Thioglycolic acid (TGA). With this being negatively charged, the TGA ligands bound on the surface of the QD's results in QD's in water giving a value of -27.6 mV.

When the QD's are functionalised, the TGA ligands are replaced with different ligands, in this project Exendin-4 and Gd-DOTA-TA are used. The table shows the value of the QD functionalised with Exendin-4 to be 2032 nm and -0.433mV. The increase in hydrodynamic diameter suggests that there is functionalisation, but there are large amounts of aggregations. This would be expected in line with the low concentrations achieved after functionalisation. Exendin-4 is negatively charged.
The TGA on the QD should be replaced with the Exendin-4, so the overall charge increase. This is seen in the Zeta value being close to neutral, but as the charge gets close to zero, it allows for large aggregates to form (seen in the DLS).

The table describes that the QD's functionalised with Gd-DOTA-TA have values of 46.62 nm and -9.59 mV. The size of the nanoparticle has decreased, and the charge has increased indicating that the functionalisation has been successful. The Gd(III) complexes hold a neutral charge, so the increase in overall charge is expected. The lower hydrodynamic diameter suggests that there are lower numbers of aggregates in the solution. Using the Evans method to calculate the concentration of Gd(III), it was calculated that there were 1462 complexes on the surface of the nanoparticle. Finally, the table also describes the QD's functionalised with Exendin-4 and Gd-DOTA-TA with values of 533.6 nm and -20.1 mV and with the value of the Zeta potentially increasing, this indicates that there has been an accurate exchange of ligands and therefore the QD's have been functionalised well, with both the exendin and the Gd-DOTA-TA. The large size in DLS suggests aggregates are being formed.

The r_1 for Gd-DOTA-TA was 4.8 $mM^{-1}s^{-1}$ at 400 MHz, this is similar to that of Gd-DOTA (4.4 $mM^{-1}s^{-1}$) (Stasiuk 2013), when on the QD this lowers to 2.9 $mM^{-1}s^{-1}$, which is unexpected as the larger mass should lower rotational correlation time and an increase of r_1 would be seen (Stasiuk, 2011). This relaxivity is per Gd(III) unit when the relaxivity is per object the r_1 is significantly increased to 4239 $mM^{-1}s^{-1}$, this number per object is the largest for a QD-Gd conjugate with values of 2500 $mM^{-1}s^{-1}$ being reported (Stasiuk, 2013).

The relativity of the QD-Exendin-Gd-DOTA-TA conjugate could not be determined due to the low concentration obtained.

Table 3.1.1: A table reporting the r_1, dynamic light scattering measurements, and Zeta potential of the red fluorescing quantum dots, and the red fluorescing quantum dots functionalised with either Exendin-4, GD-DOTA-TA, or both.

Compounds	r_1 / $mM^{-1}s^{-1}$	Size / nm	ZETA / mV
InP/ZnS	-	89.30	-27.6
QD-Exendin	-	2032	-0.433
QD-Gd-DOTA-TA	2.9	46.62	-9.59
QD-Exendin-Gd-DOTA-TA	-	533.6	-20.1

3.2 Cell Characterisation

3.2.1 FACS Analysis

To determine whether the GLP1-R was expressed in the MIN6 cell line, FACS analysis was conducted on the MIN6 cells and the HEK-293 cells, which do not express GLP1-R. As described in section 2.4.1, both cell lines were run through FACS analysis. Each experiment had a control cell group, with the control antibody added. In addition to a control cell group, each experiment had either the HEK293 or MIN6 cells, with the GLP1-R antibody added. Figure 3.2.1 shows two histograms which represent whether or not the antibodies used bound specifically to GLP1-R, and therefore this would determine the receptors presence in the HEK293, and MIN6 cell line. The figure on the left shows the experiment that was run in HEK-293 cells. The purple peak represents the control cell population, and the green peak represents the cells that had the GLP-1R antibody added to them. The histogram shows a small shift which indicates unspecific binding. The figure on the right shows the experiment that was run in MIN6 cells. Again, the purple peak represents the control cell population, and the green peak represents the cells that had the GLP-1R antibody added to them. The histogram shows a large shift away from the control cell population which indicates the antibody is specifically binding to the GLP1-R (R&D Systems, 2019). This experiment showed that GLP1-R is being expressed in the MIN6 cell line and therefore, confocal studies with Exendin-4 conjugates could be conducted, as this protein should specifically bind to the GLP1-R.

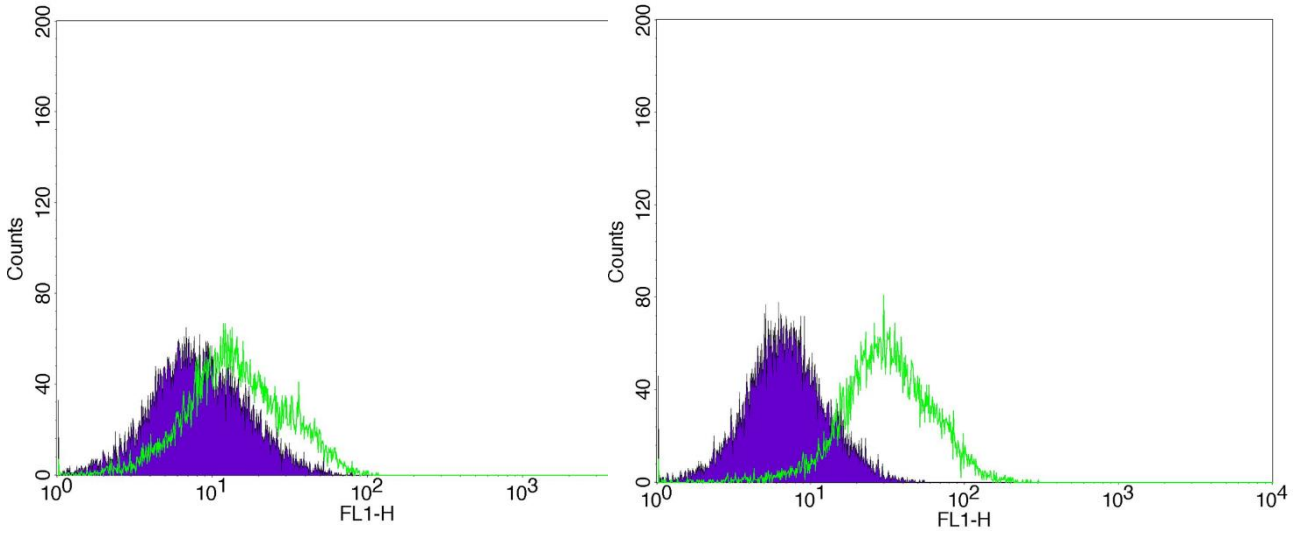

Figure 3.2: The histograms denoting the expression of GLP1-R in the cell lines HEK-293 (Left) and MIN6 (Right). FACS analysis was conducted on the two cells lines. In each histogram, the purple peaks represent the control cell group and the green peaks represents the cell lines with the GLP1-R antibody added. (Antibodies used: Human GLP-1R Alexa Fluro 488-conjugated antibody; Mouse IgG2B Alexa Fluro 488-conjugated Isotype Control. R&D Systems).

3.2.2 Confocal Microscopy

Initial experiments were conducted with red fluorescing quantum dots (Red QD's). The red QD's were used in a time course study in HEK-293 and MIN6 cells to observe the incubation time required for the red QD's to be endocytosed into the cells. Following the initial studies, further time course studies using yellow fluorescing quantum dots (Yellow QD's), and Yellow QD's functionalised with Exendin-4, Gd-DOTA-TA, and both Exendin-4 and Gd-DOTA-TA were conducted in HEK-293 and MIN6 cells.

Figure 3.2.1 and figure 3.2.2 show the confocal time course studies of HEK293 cells incubated with Red QD's and MIN6 cells incubated with Red QD's, respectively. The time course study for each cell line includes a 8,4,2 and 1 hour time point to give an initial idea of how long the cells required in order to uptake the QD's.

The images from the HEK293 Red QD time course study (figure 3.2.1) show a uptake in QD after 1 hour incubation and throughout the time course, Red QD was taken into the cells and appears to have localised into particular areas in clusters, perhaps indicating that they are localising into particular cell organelles. This finding initially could be a longer time period used in comparison to other QD studies used in HEK293 cells. In Zhang *et al*. (2016), CdSe/ZnS QD's were up-taken in HEK293 cells within 30 minutes, and those functionalised with different proteins to investigate binding to the cell membrane, entered within 1 hour. Though the QD's in this study has InP cores, it gives an initial indication that QD's in HEK293 cells may be able to uptake QD's in a shorter time. The fluorescence intensity of the confocal images at each time point was calculated and has been shown in figure 3.2.3. The figure shows that the fluorescence is increasing as the time increases in the HEK293 study. As the longer time points show an higher intensity, perhaps the QD has had more time to localise and more QD has been able to enter the cell causing an increase in fluorescence intensity. This could support the observation that the QD is localising in particular areas, if more QD enters and localises over time.

The images from the MIN6 Red QD time course study (figure 3.2.2) also show an uptake in QD after 1 hour, though in more quantity, compared to the HEK293 images. The Red QD was taken into the cells and again appears to have localised into particular areas in clusters. In Yong *et al*., (2009) the pancreatic cell line MiaPaCa was used and cells were incubated with InP/ZnS QD's for 2 hours and 1 hour and significant uptake was seen. Though this Master's project uses a different cell line, the findings do show similarities in the incubation time required for the QD's to enter the cell. The fluorescence intensity of the confocal images at each time point was calculated and has been shown in figure 3.2.3. The figure shows the fluorescence increasing over time but the measurements are higher in value compared to the HEK293 values. As with the HEK293 study, As the longer time points show an higher intensity, perhaps the QD has had more time to localise and more QD has been able to enter the cell causing a increase in fluorescence intensity.

Quantum dots can enter cells non-specifically, or bind specifically to receptors. As Table 3.1.1 shows, the QD's are negatively charged (with a value of -27.6mV) and because of this, the cell membrane's phospholipid bilayer (which is positively charged) is likely interacting with the QD's and entering the cell by endocytosis.

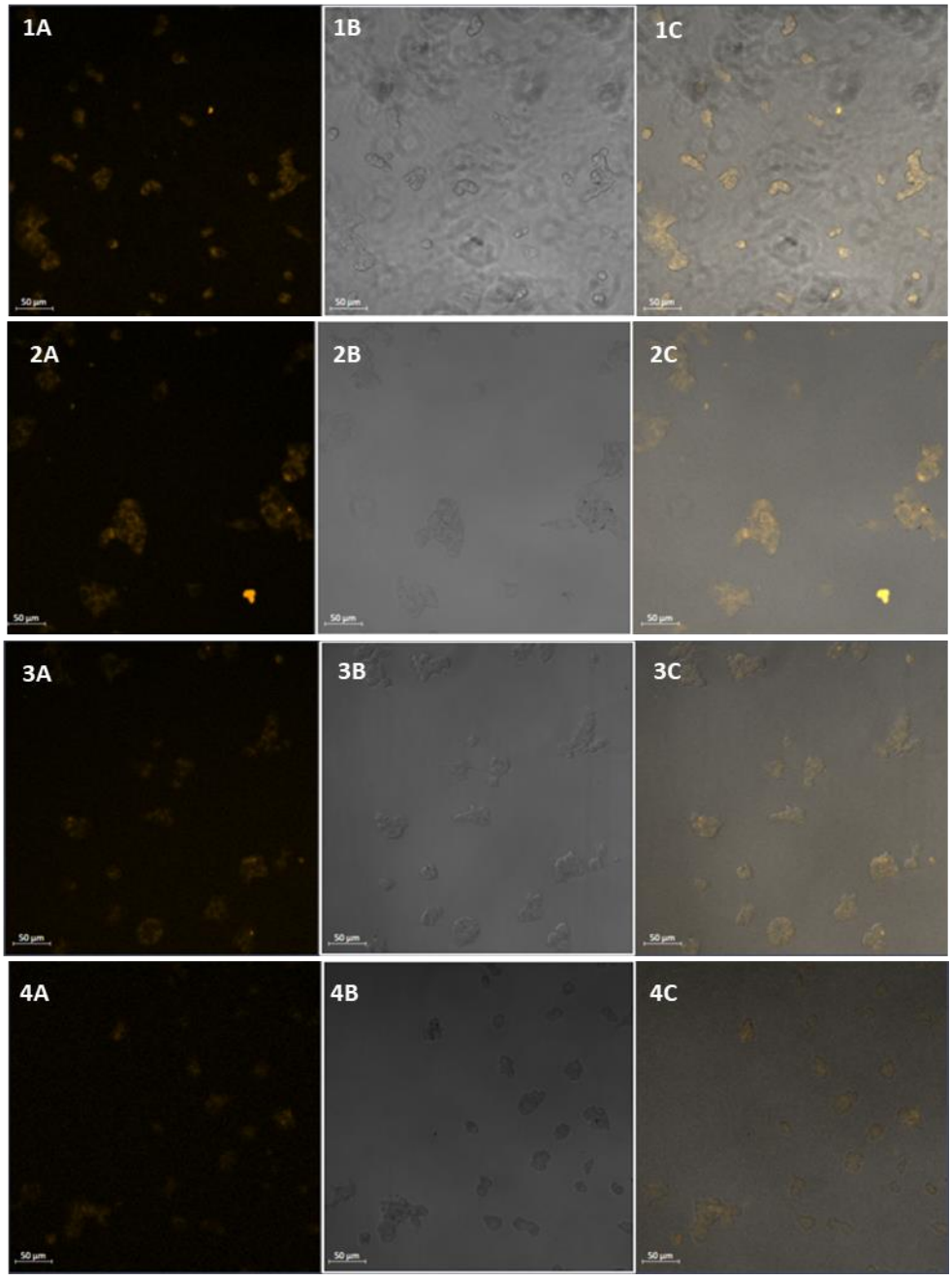

Figure 3.2.1: Confocal images from a 8 hour time course study of HEK293 cells incubated with Red QD's (concentration of 3.22×10^{-6} M). Confocal microscopy was used to obtain images from each time point in the time course study. 8 hours (1A,1B,1C. 50µm scalebar), 4 hours (2A,2B,2C. 50µm scalebar), 2 hours (3A,3B,3C. 50µm scalebar), 1 hour (4A,4B,4C. 50µm scalebar).

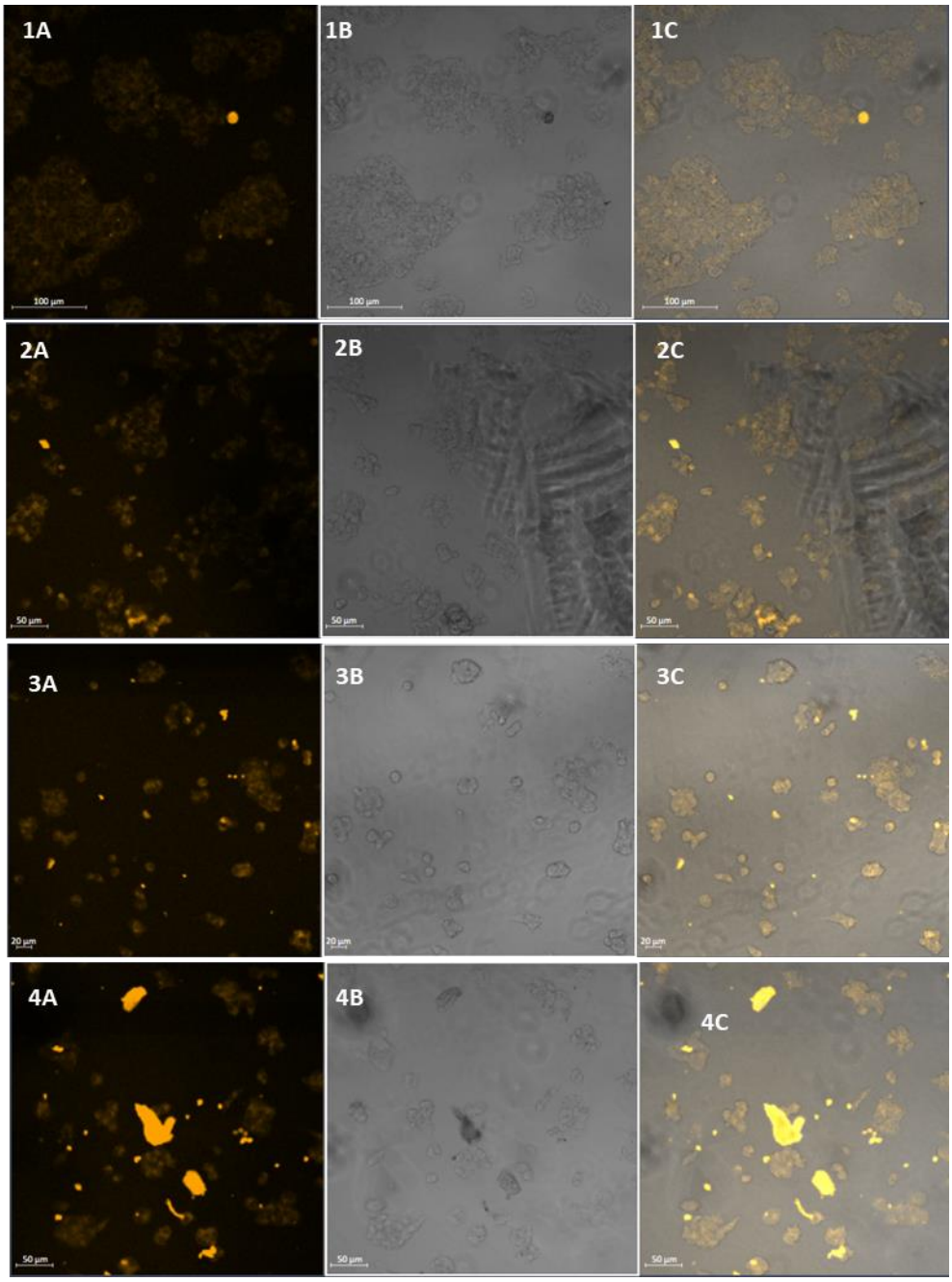

Figure 3.2.2: Confocal images from a 8 hour time course study of MIN6 cells incubated with Red QD's (concentration of 3.22×10^{-6} M). Confocal microscopy was used to obtain images from each time point in the time course study. 8 hours (1A,1B,1C. 100µm scalebar), 4 hours (2A,2B,2C. 50µm scalebar), 2 hours (3A,3B,3C. 20µm scalebar), 1 hour (4A,4B,4C. 50µm scalebar).

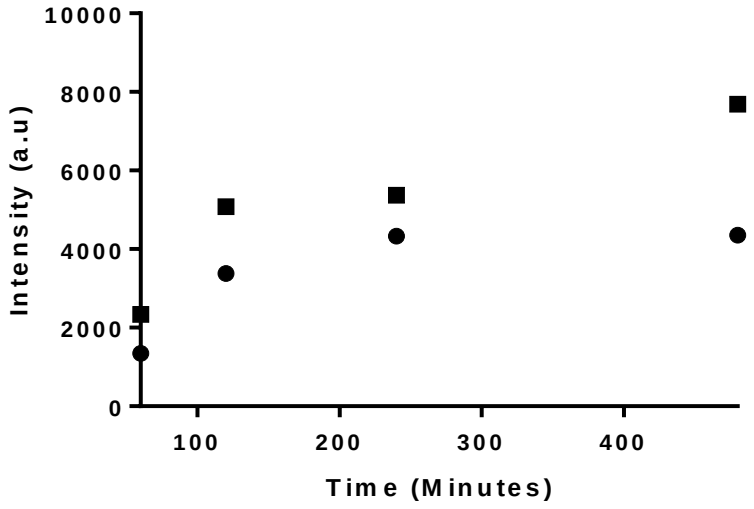

Figure 3.2.3: Fluorescence intensity measurements of each confocal image taken in the time course studies of HEK293 and MIN6 cells incubated with Red QD's (concentration 3.22×10^{-6} M). Circle points represent HEK-293, Square points represent MIN6. The 'analyse' function was used in ImageJ to obtain an average fluorescence intensity measurement of each image in the time course and were plotted on GraphPad.

Figure 3.2.4 and figure 3.2.5 show the confocal time course studies of HEK293 cells incubated with Yellow QD's and MIN6 cells incubated with Yellow QD's, respectively. With the previous results from the time course studies using Red QD's, the Yellow QD time course studies were altered to investigate time points at 1 hour and less. This was because the previous two studies indicated the cells were up taking QD in as little as 1 hour incubation time.

The images from the HEK293 Yellow QD time course study (figure 3.2.4) show a small amount of uptake in QD after 1 hour incubation. Before this time point however, a decrease in uptake was observed. This could of perhaps been due to the washing and fixing process, so quantum dot was washed away and less QD could be uptaken. The images do show clusters of QD, and this occurs due to the charge of the QD and the ligands on it's surface.

The fluorescence intensity of the confocal images at each time point was calculated and has been shown in figure 3.2.6. The figure shows that the fluorescence is low at each time point, additionally supporting the observation that QD was not up taken as successfully in the HEK293 Yellow QD experiment.

The images from the MIN6 Yellow QD time course study (figure 3.2.5) show a large amount of QD uptake into the cells, as well as clusters of QD alone within the image. To determine whether QD is localising in particular organelles, confocal co-localisation studies should be conducted. As previously mentioned, this uptake is likely non-specific due to the charges of the QD and the cells membrane. Additional QD could of clustered together in these images due to not being washed away in the washing and fixing process.

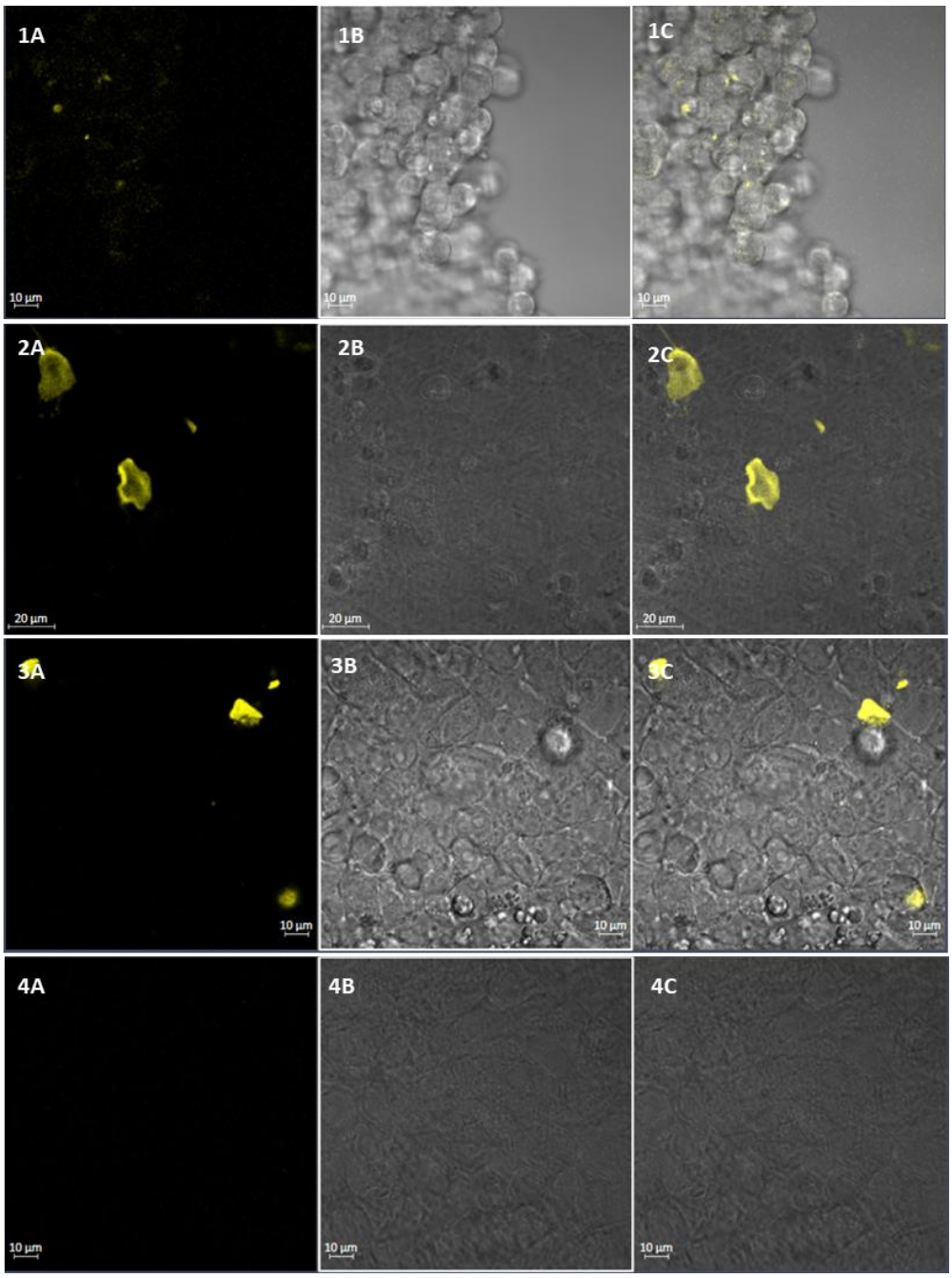

Figure 3.2.4: Confocal images from a 1 hour time course study of HEK-293 cells incubated with Yellow QD's (concentration of 2.95×10^{-9} M). Confocal microscopy was used to obtain images from each time point in the time course study. 1 hour (1A,1B,1C. 10µm scalebar), 30 minutes (2A,2B,2C. 20µm scalebar), 20 minutes (3A,3B,3C. 10µm scalebar), 10 minutes (4A,4B,4C. 10µm scalebar).

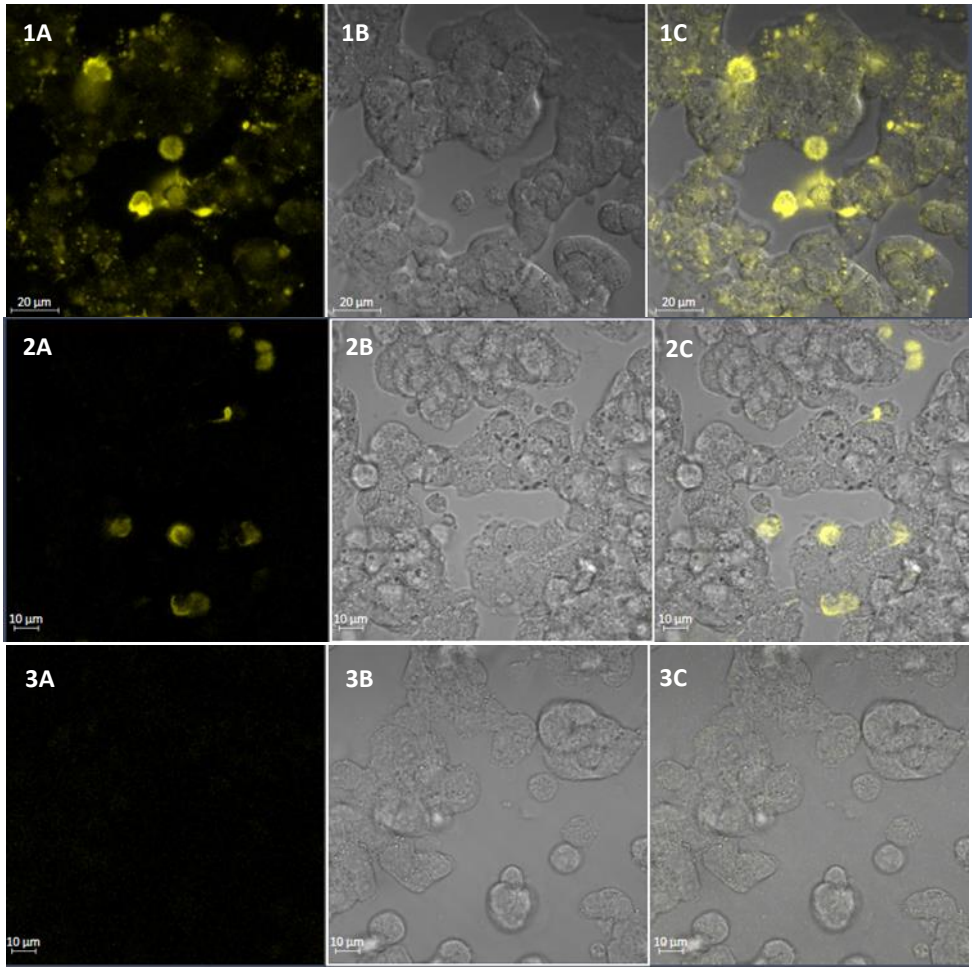

Figure 3.2.5: Confocal images from a 1 hour time course study of MIN6 cells incubated with Yellow QD's (concentration of 2.95×10^{-9} M). Confocal microscopy was used to obtain images from each time point in the time course study. 1 hour (1A,1B,1C. 10µm scalebar), 30 minutes (2A,2B,2C. 10µm scalebar), 10 minutes (3A,3B,3C. 10µm scalebar).

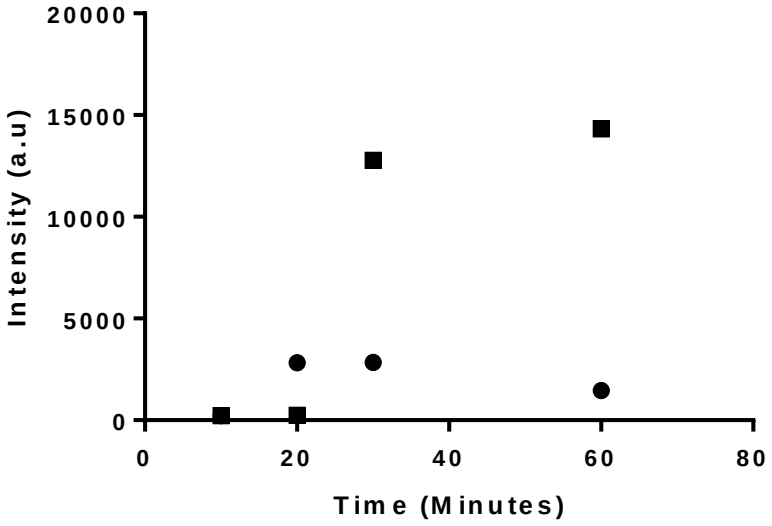

Figure 3.2.6: Fluorescence intensity measurements of each confocal image taken in the time course studies of HEK293 and MIN6 cells incubated with Yellow QD's (concentration $2.95x10^{-9}$ M). Circle points represent HEK-293, Square points represent MIN6. The 'analyse' function was used in ImageJ to obtain an average fluorescence intensity measurement of each image in the time course and were plotted on GraphPad.

Figure 3.2.7 and figure 3.2.8 show the confocal time course studies of HEK293 cells incubated with Yellow QD's functionalised with Exendin-4 and MIN6 cells incubated with Yellow QD's functionalised with Exendin-4, respectively.

The images from the HEK293 Yellow QD functionalised with Exendin-4 time course study (figure 3.2.7) show a large amount of uptake throughout the cell at the 1 hour time point, with clusters of QD within some of the cells. This again could be the QD localising at particular organelles as previously speculated. At the 30 minutes time point, and less, there is a significantly less amount of QD uptake. This could of perhaps been due to the washing and fixing process, or due to the health of the cells.

The images from the MIN6 Yellow QD functionalised with Exendin-4 time course study (figure 3.2.8) show binding to the outside of the cells at the 1 hour time point and the 30 minute time point. β-cell of the Islets of Langerhans in the pancreas express the receptor GLP1-R (Wang *et al.,* 2014). As MIN6 is a pancreatic β-cell cell line, MIN6 cells should also express this receptor (Rajan *et al*., 2015). This was shown to be occurring in the FACS analysis histograms shown in Figure 3.2**.** Exendin-4 is an agonist of GLP-1R, the Exendin-4 should therefore exhibit specific binding to this receptor (Nakashima *et al*., 2012). As the images show binding to the cell membrane, this could be suggesting the QD functionalised with Exendin-4 is specifically binding to the GLP1-R and entering the cell this way.

A study by Jones *et al*., (2018) demonstrated by confocal microscopy that cellular dyes modified with Exendin-4 localise to the surface of MIN6 cells expressing GLP1R. As previous studies such as this have shown Exendin-4 can specifically bind to the GLP1-R. Furthermore, the study by Jones *et al*., (2018) reports that the Exendin-4 is entering the cell because GLP1-R is undergoing agonist-mediated endocytosis. This finding could be used to support that the QD functionalised with Exendin-4 in this Master's project is entering specifically through the receptor. In future, more could be done to investigate then internalisation process.

The fluorescence intensity of the confocal images at each time point was calculated and has been shown in figure 3.2.9. The graph shows that HEK293 increases with intensity over time, as does MIN6. However, the 30 minutes and the 60 minute measurements of the MIN6 data points as higher in intensity compared to the HEK293, indicating more QD uptake.

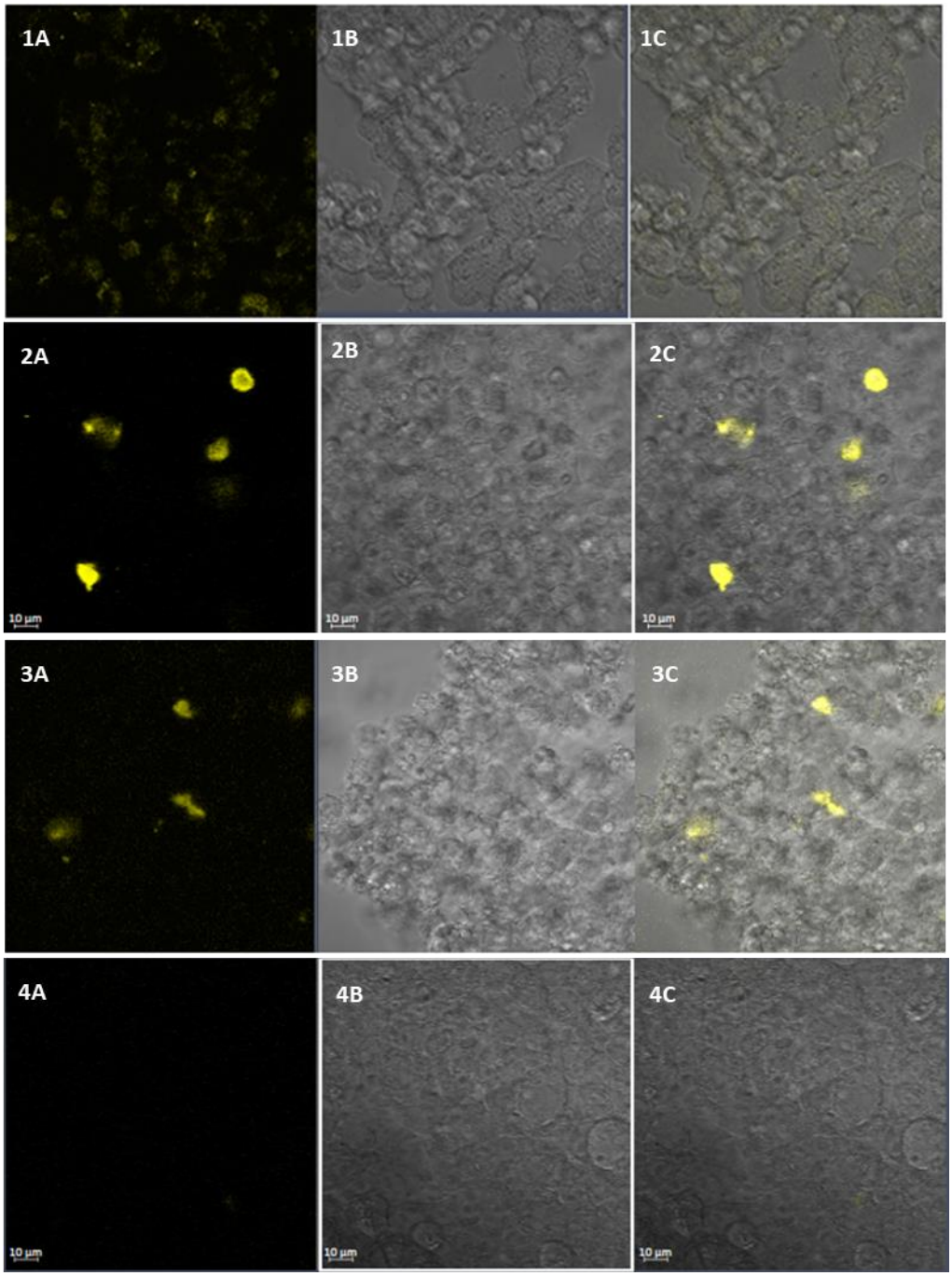

Figure 3.2.7: Confocal images from a 1 hour time course study of HEK-293 cells incubated with Yellow QD's functionalised with Exendin-4 (concentration of 2.25×10^{-9} M). Confocal microscopy was used to obtain images from each time point in the time course study. 1 hour (1A,1B,1C. 10µm scalebar), 30 minutes (2A,2B,2C. 10µm scalebar), 20 minutes (3A,3B,3C. 10µm scalebar), 10 minutes (4A,4B,4C. 10µm scalebar).

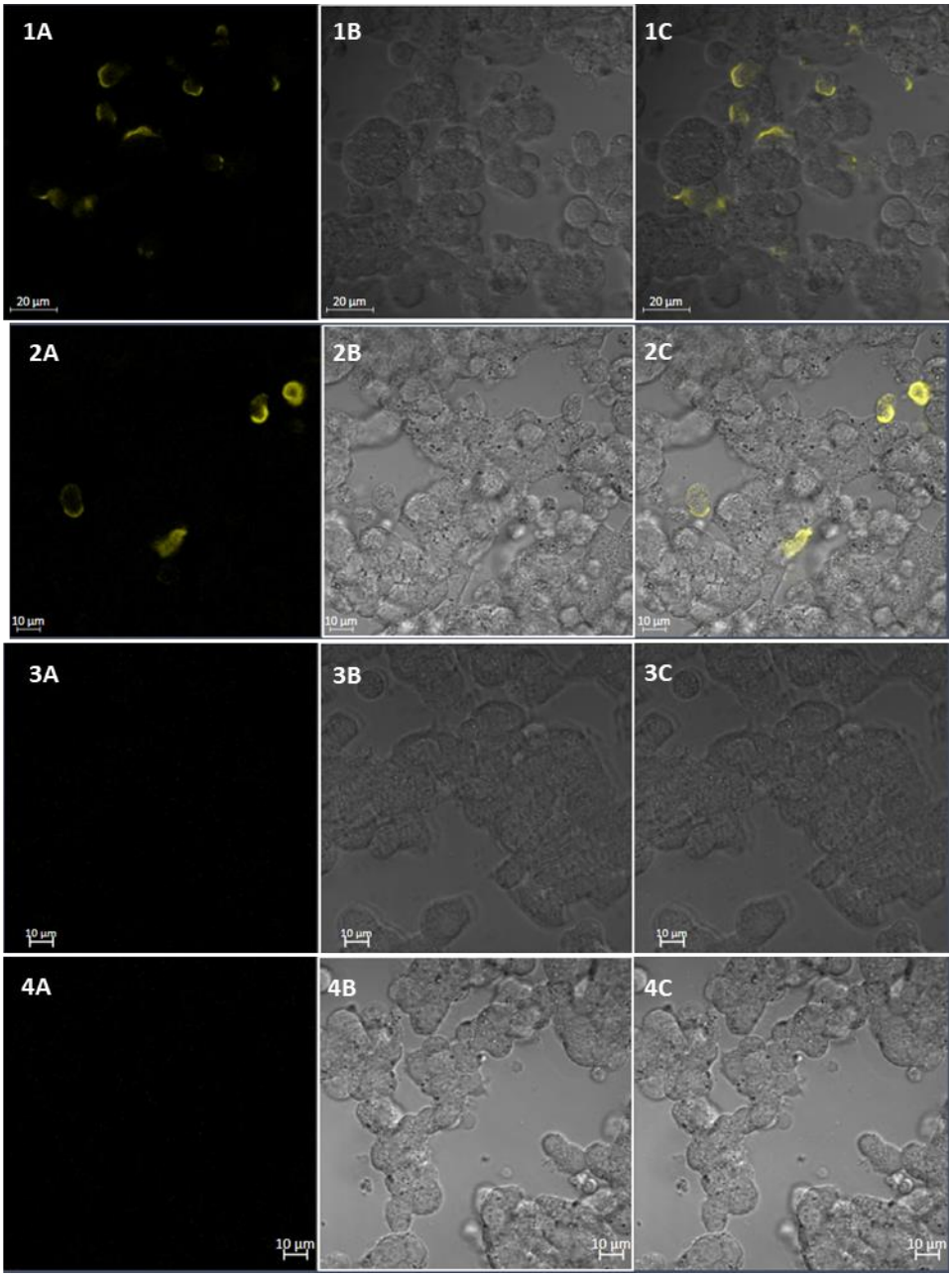

Figure 3.2.8: Confocal images from a 1 hour time course study of MIN6 cells incubated with Yellow QD's functionalised with Exendin-4 (concentration of 2.25×10^{-9} M). Confocal microscopy was used to obtain images from each time point in the time course study. 1 hour (1A,1B,1C. 20µm scalebar), 30 minutes (2A,2B,2C. 10µm scalebar), 20 minutes (3A,3B,3C. 10µm scalebar), 10 minutes (4A,4B,4C. 10µm scalebar).

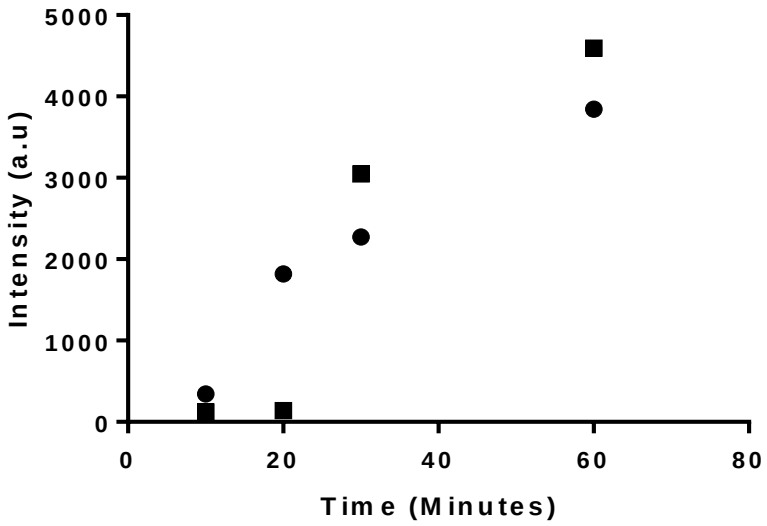

Figure 3.2.9: Fluorescence intensity measurements of each confocal image taken in the time course studies of HEK293 and MIN6 cells incubated with Yellow QD's functionalised with Exendin-4 (concentration $2.25x10^{-9}$ M). Circle points represent HEK-293, Square points represent MIN6. The 'analyse' function was used in ImageJ to obtain an average fluorescence intensity measurement of each image in the time course and were plotted on GraphPad.

Figure 3.2.10 and figure 3.2.11 show the confocal time course studies of HEK293 cells incubated with Yellow QD's functionalised with Gd-DOTA-TA and MIN6 cells incubated with Yellow QD's functionalised with Gd-DOTA-TA, respectively.

The images from the HEK293 Yellow QD functionalised with Gd-DOTA-TA time course study (figure 3.2.10) show clusters of the compound but no significant uptake into the cells. This could of perhaps been due to the washing and fixing process, or due to the health of the cells. The images from the MIN6 Yellow QD functionalised with Gd-DOTA-TA show more cell uptake at the 1 hour and 30 minute time points. This could be because the MIN6 cells are more versatile and will uptake the QD-GD compound.

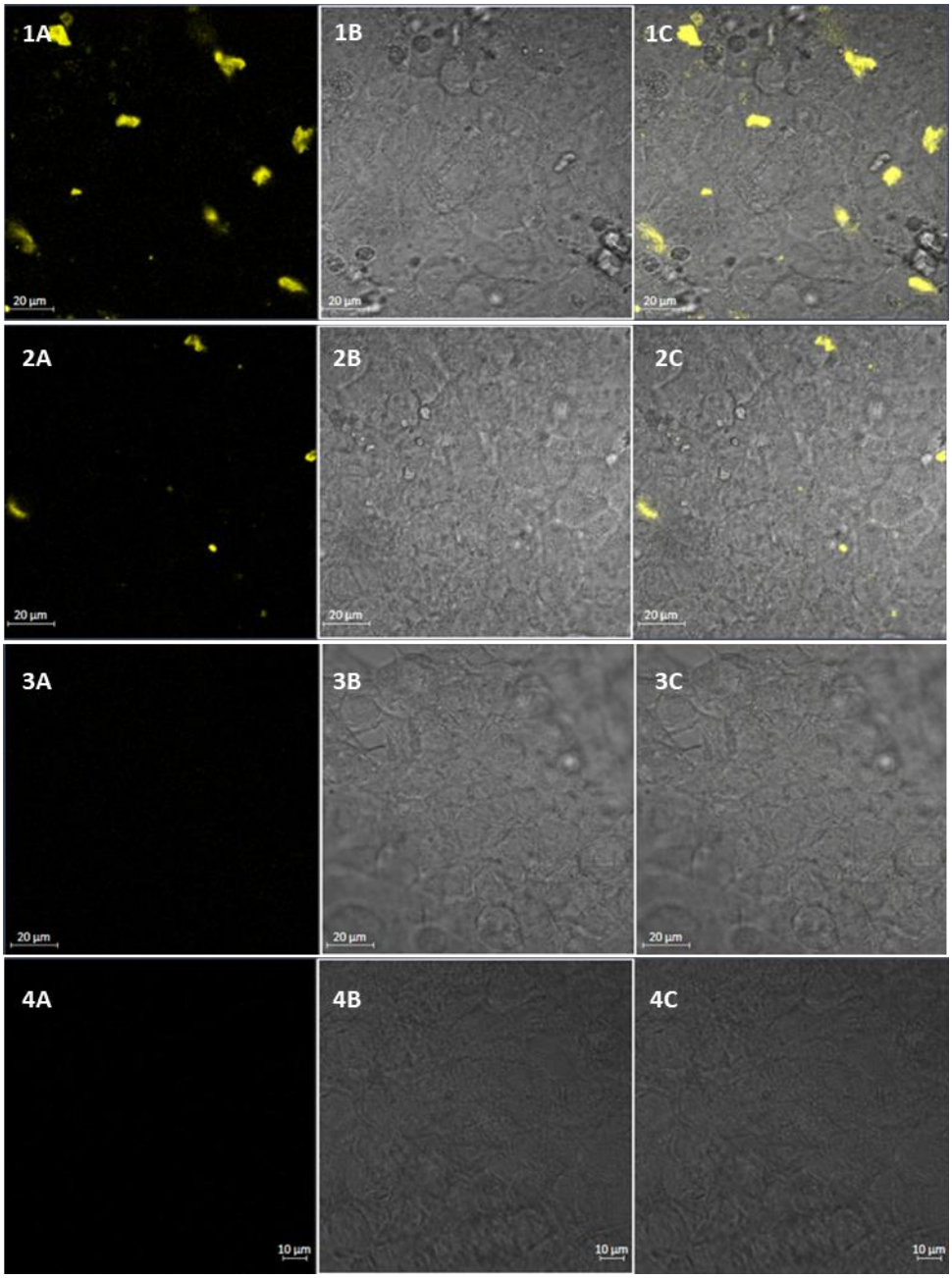

Figure 3.2.10: Confocal images from a 1 hour time course study of HEK-293 cells incubated with Yellow QD's functionalised with Gd-DOTA-TA (concentration of 1.6×10^{-9} M). Confocal microscopy was used to obtain images from each time point in the time course study. 1 hour (1A,1B,1C. 20µm scalebar), 30 minutes (2A,2B,2C. 20µm scalebar), 20 minutes (3A,3B,3C. 20µm scalebar), 10 minutes (4A,4B,4C. 10µm scalebar).

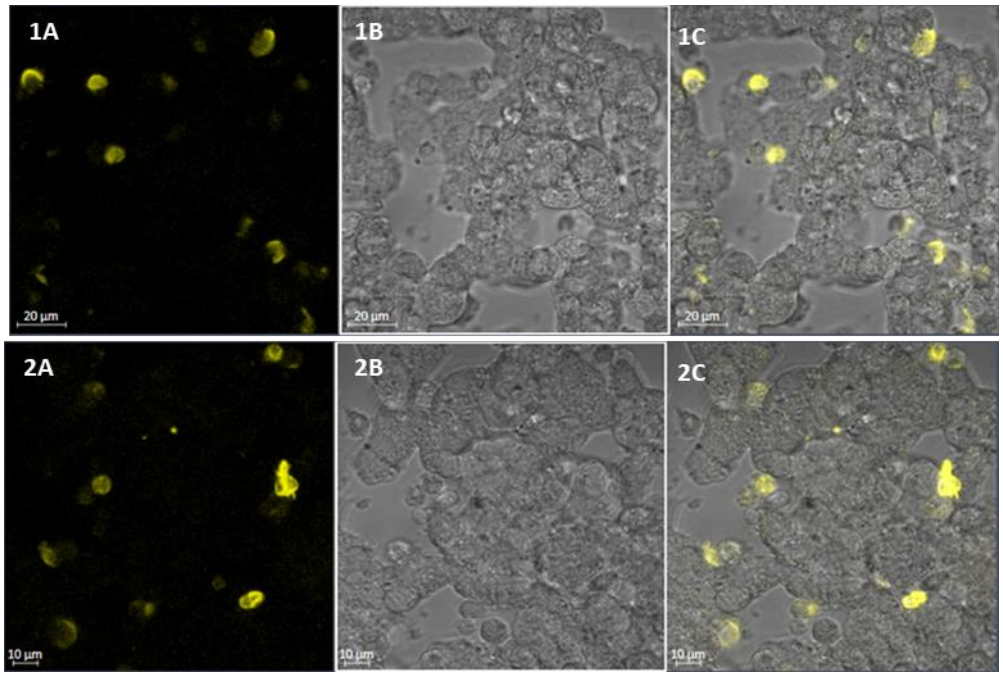

Figure 3.2.11: Confocal images from a 1 hour time course study of MIN6 cells incubated with Yellow QD's functionalised with Gd-DOTA-TA (concentration of $1.6x10^{-9}$ M). Confocal microscopy was used to obtain images from each time point in the time course study. 1 hour (1A,1B,1C. 10µm scalebar), 30 minutes (2A,2B,2C. 10µm scalebar).

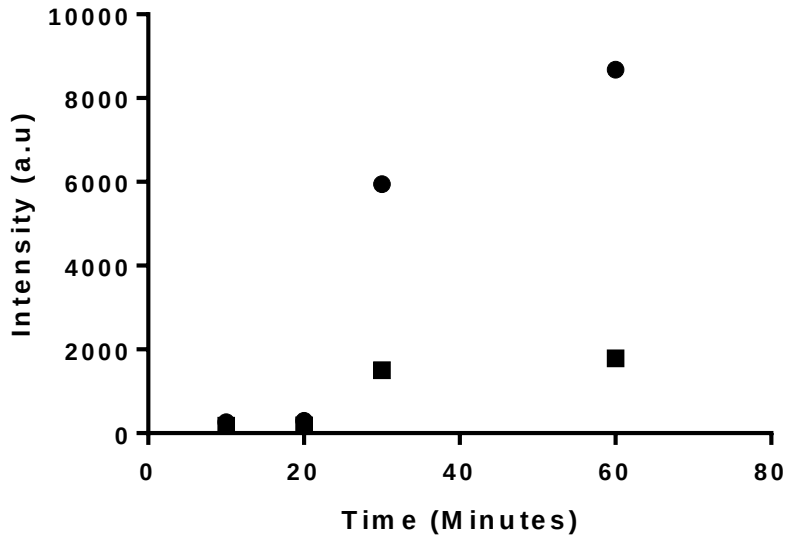

Figure 3.2.12: Fluorescence intensity measurements of each confocal image taken in the time course studies of HEK293 and MIN6 cells incubated with Yellow QD's functionalised with Gd-DOTA-TA (concentration $1.6x10^{-9}$ M). Circle points represent HEK-293, Square points represent MIN6. The 'analyse' function was used in ImageJ to obtain an average fluorescence intensity measurement of each image in the time course and were plotted on GraphPad.

Figure 3.2.13 and figure 3.2.14 show the confocal time course studies of HEK293 cells incubated with Yellow QD's functionalised with Exendin-4 and Gd-DOTA-TA and MIN6 cells incubated with Yellow QD's functionalised with Exendin-4 and Gd-DOTA-TA, respectively.

The images from the HEK293 Yellow QD functionalised with Exendin-4 and Gd-DOTA-TA time course study (figure 3.2.13) show that the compound was not up taken into the cells. Figure 3.2.13 includes the cell control for the HEK293 experiments and shows there is no background fluorescence in the control image, so the fluorescence seen in the confocal images is that of the QD and QD functionalised compounds. The images from the MIN6 Yellow QD functionalised with Exendin-4 and Gd-DOTA-TA time course study (figure 3.2.14) show the QD is localised into areas of the cell at the 1 hour time point and 30 minute time point. Exendin-4 on the compound could of contributed to the compound going into the cell similarly to the QD's functionalised with Exendin-4 only (Jones *et al*., 2018.)

The fluorescence intensity of the confocal images at each time point was calculated and has been shown in figure 3.2.15. The graph shows a increase in intensity as time increases, with a large jump in intensity between 30 and 60 minutes.

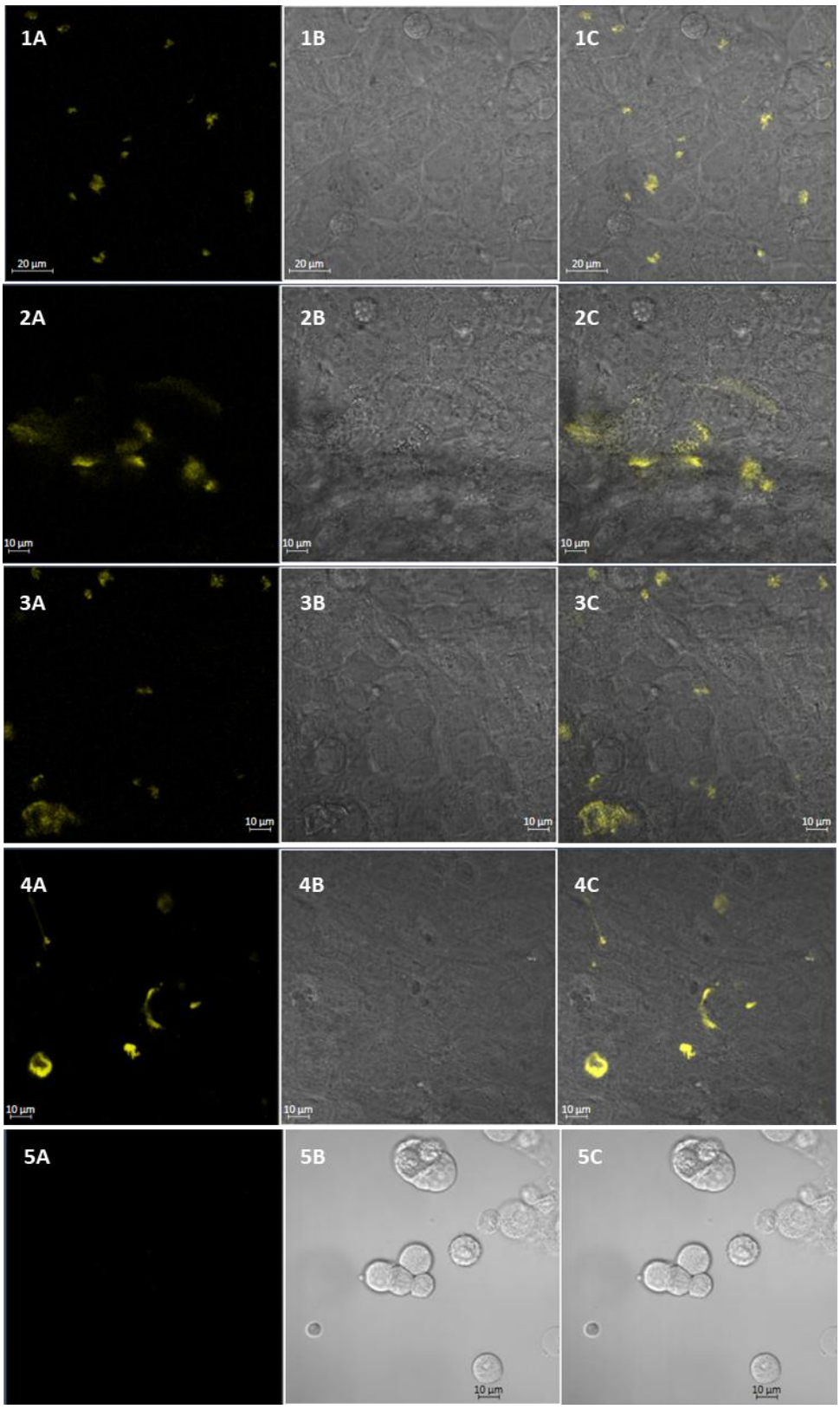

Figure 3.2.13: Confocal images from a 1 hour time course study of HEK-293 cells incubated with Yellow QD's functionalised with Exendin-4 and Gd-DOTA-TA (concentration of 1.64×10^{-9} M). Confocal microscopy was used to obtain images from each time point in the time course study. 1 hour (1A,1B,1C. 20µm scale bar), 30 minutes (2A,2B,2C. 10µm scale bar), 20 minutes (3A,3B,3C. 10µm scale bar), 10 minutes (4A,4B,4C. 10µm scale bar) and the cell control (5A,5B.5C. 10µm scale bar).

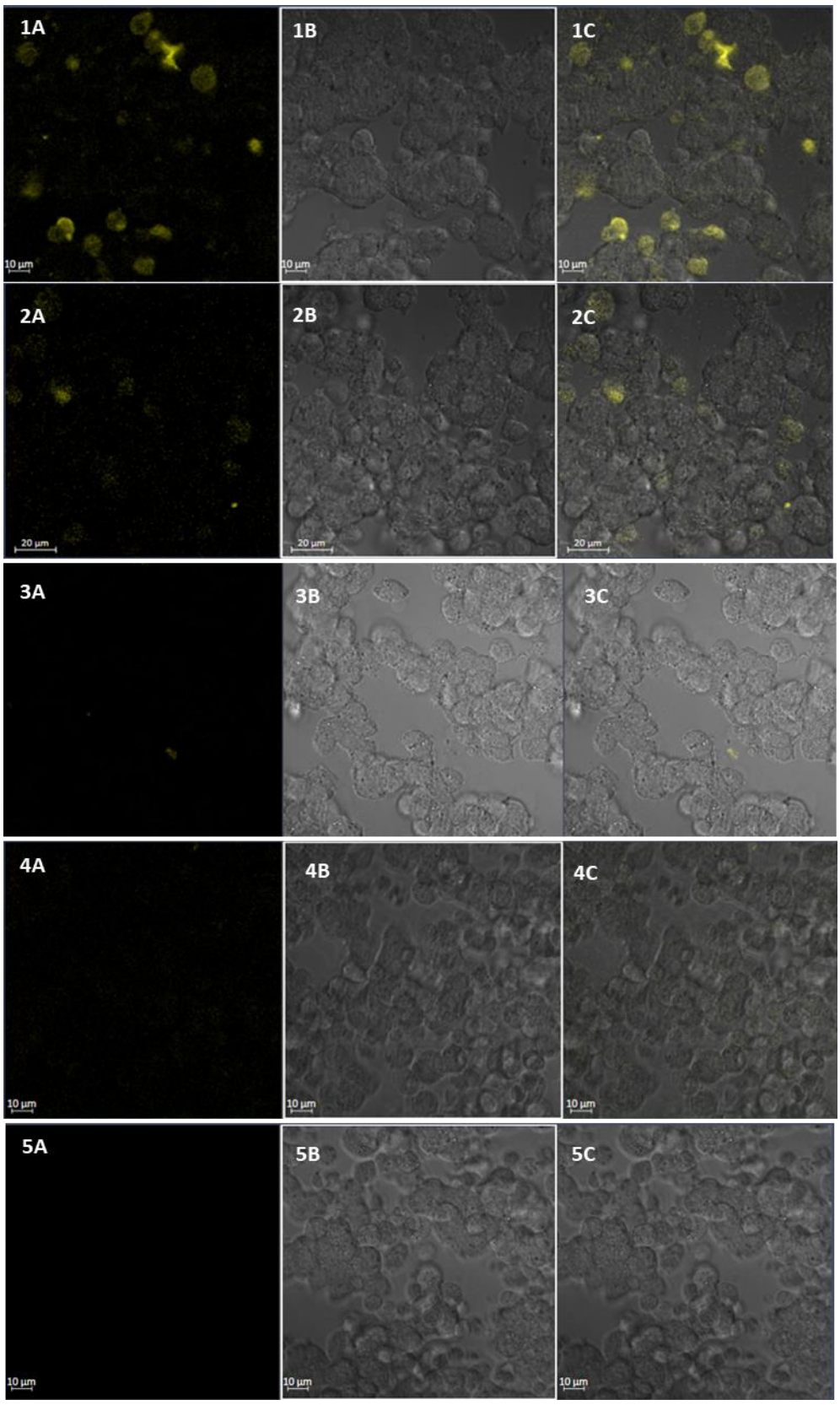

Figure 3.2.14: Confocal images from a 1 hour time course study of MIN6 cells incubated with Yellow QD's functionalised with Exendin-4 and Gd-DOTA-TA (concentration of 1.64×10^{-9} M). Confocal microscopy was used to obtain images from each time point in the time course study. 1 hour (1A,1B,1C. 10µm scale bar), 30 minutes (2A,2B,2C. 20µm scale bar), 20 minutes (3A,3B,3C. 10µm scale bar), 10 minutes (4A,4B,4C. 10µm scale bar) and the cell control (5A,5B.5C. 10µm scale bar).

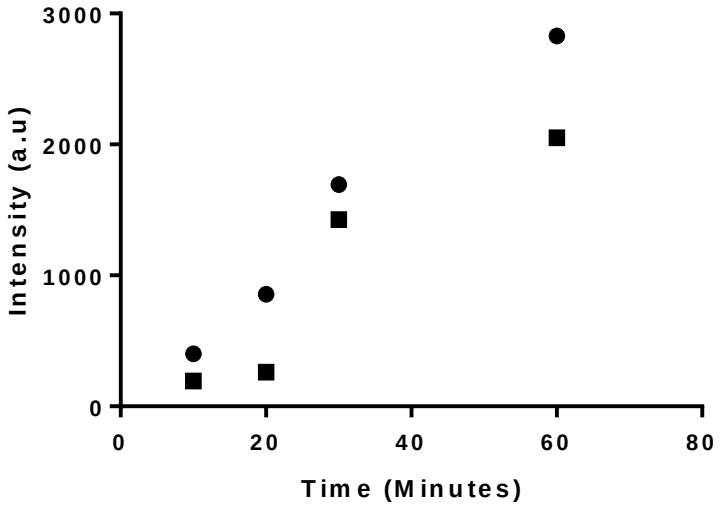

Figure 3.2.15: Fluorescence intensity measurements of each confocal image taken in the time course studies of HEK293 and MIN6 cells incubated with Yellow QD's functionalised with Exendin-4 and Gd-DOTA-TA (concentration $1.64x10^{-9}$ M). Circle points represent HEK-293, Square points represent MIN6. The 'analyse' function was used in ImageJ to obtain an average fluorescence intensity measurement of each image in the time course and were plotted on GraphPad.

3.3 Cell Viability

The MTS assay as previously described in section 2.3 is a 3 day assay that is used to assess cell viability when cells are incubated with particular compounds. The assays were done by incubating each of the compounds in both cell lines (HEK-293 and MIN6).

The results for HEK-293 cells incubated with Yellow QD's, as seen in figure 3.3.1, show a increase in absorbance between 0.000652nM and 0.000362nM, with each data point having a varied amount of error, with error bars exceeding 5%. The data points do show increase but not consistently. This likely due to the variation in the control values, and experimental values in the HEK293 cells. Cells were likely seeded unevenly, or were over confluent. Despite this, the cells are increasing in absorbance suggesting the cells are viable at the concentrations used. When MIN6 were incubated with Yellow QD's, as seen in figure 3.3.2, there appears to be no clear correlation, with data points staying at between 0.2 and 0.5 absorbance at 490nm. The error bars are also larger in each data, point. This again indicates there was the variation in the control values, and experimental values in the MIN6 cells. The MTS assays with QD's don't show any initial toxic effects, which is to be expected. This is because the QD's used were InP/ZnS QD's, and these are free of any heavy metals. As discussed in Clarke *et al*., (2019) InP/ZnS QD's should therefore not exhibit toxic effects in a biological application.

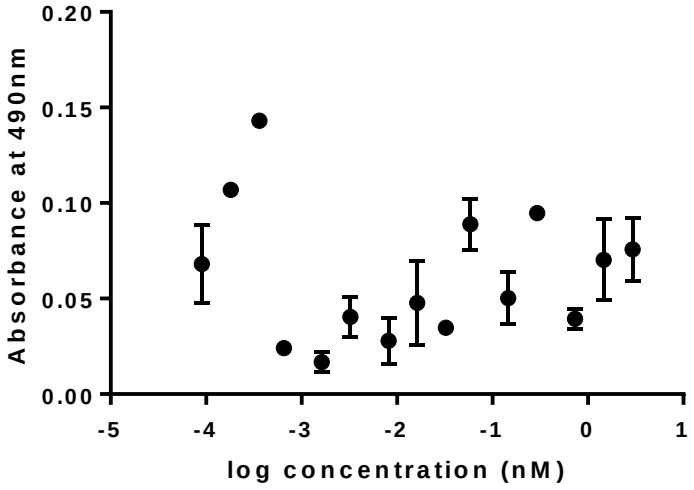

Figure 3.3.1: MTS assay results of HEK-293 cells incubated with Yellow QD's (2.935 nM to 0.0000905 nM) overnight at 37°C, 5% CO_2. After overnight incubation, cells were washed and incubated with MTS solution for 1-2 hours. Absorption was recorded by a BIO-TEK Synergy HT plate reader at 490nm and absorption data plotted with the control readings, against log concentration on GraphPad (n=2).

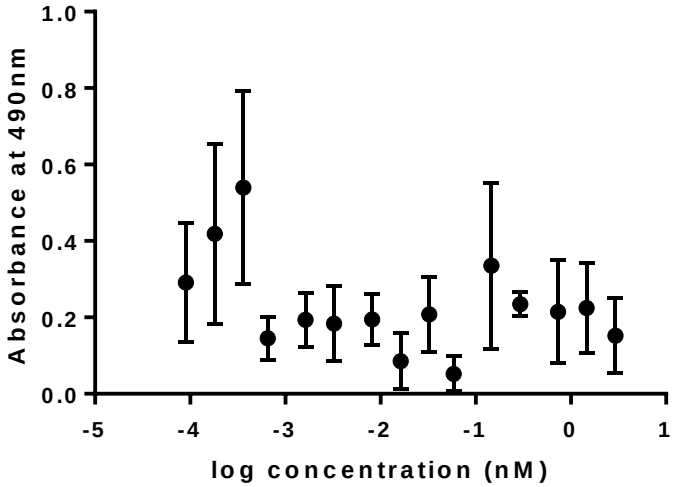

Figure 3.3.2: MTS assay results of MIN6 cells incubated with Yellow QD's (2.935 nM to 0.0000905 nM) overnight at 37°C, 5% CO_2. After overnight incubation, cells were washed and incubated with MTS solution for 1-2 hours. Absorption was recorded by a BIO-TEK Synergy HT plate reader at 490nm and absorption data plotted with the control readings, against log concentration on GraphPad (n=2).

The results for the HEK-293 cells incubated with Yellow QD's functionalised with Exendin-4, shown in figure 3.3.3, show an increase in absorbance between 0.0163nM and 0.0587nM, before dropping in absorbance again. This indicates that the cells may be less viable after this point so smaller intervals in concentration could be investigated in further studies. The error bars are large and this could have been due to the uneven seeding of cells and variation in the control values. This could also be due to the aggregation of the compound as indicated by Table 3.1.1. The Zeta potential value of the QD functionalised with Exendin-4 is -0.433mV. As previously discussed, the value being close to neutral allows for large aggregates to form due to the pH. The MIN6 cells incubated with Yellow QD's functionalised with Exendin-4, as shown in figure 3.3.4, show the absorbance values stay low then there is a increase in absorbance after 0.05625nM, which is a higher concentration. We would expect to see a decrease in absorbance with higher concentration, due to the aggregation in the compound.

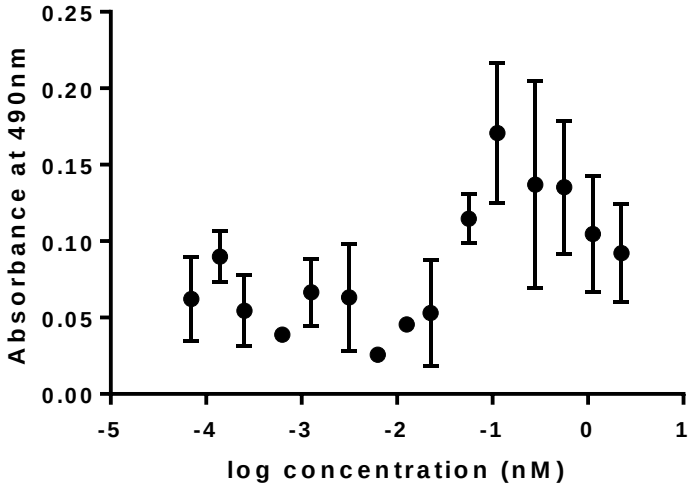

Figure 3.3.3: MTS assay results of HEK-293 cells incubated with Yellow QD's functionalised with Exendin-4 (2.25 nM to 0.00007 nM) overnight at 37°C, 5% CO2. After overnight incubation, cells were washed and incubated with MTS solution for 1-2 hours. Absorption was recorded by a BIO-TEK Synergy HT plate reader at 490nm and absorption data plotted with the control readings, against log concentration on GraphPad (n=2).

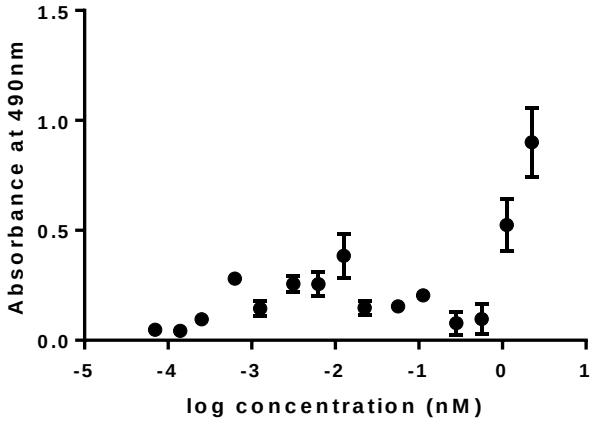

Figure 3.3.4: MTS assay results of MIN6 cells incubated with Yellow QD's functionalised with Exendin-4 (2.25 nM to 0.00007 nM) overnight at 37°C, 5% CO2. After overnight incubation, cells were washed and incubated with MTS solution for 1-2 hours. Absorption was recorded by a BIO-TEK Synergy HT plate reader at 490nm and absorption data plotted with the control readings, against log concentration on GraphPad (n=2).

The results of the HEK293 cells incubated with QD's functionalised with Gd-DOTA-TA, as shown in figure 3.3.5, show large inconsistency between points and therefore is it difficult to determine the true effects of the compound. The large error bars on each data point could be due to seeding of cells or infection within the cells. The results of MIN6 cells being incubated with QD's functionalised with Gd-DOTA-TA, as shown in figure 3.3.6, show absorbance readings between 0.10 and 0.20 at 490nm and points stay within this range. This could be an indication that the compound has little effect on this cell type, so should eb repeated to determine the effect further.

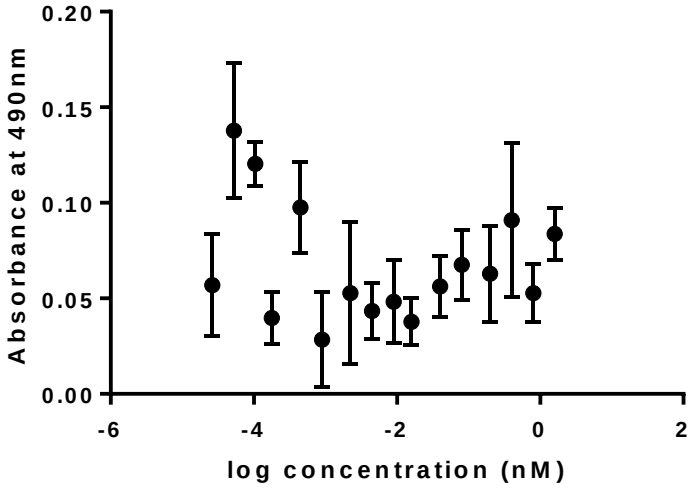

Figure 3.3.5: MTS assay results of HEK-293 cells incubated with Yellow QD's functionalised Gd-DOTA-TA (1.6 nM to 0.0000263 nM) overnight at 37°C, 5% CO2. After overnight incubation, cells were washed and incubated with MTS solution for 1-2 hours. Absorption was recorded by a BIO-TEK Synergy HT plate reader at 490nm and absorption data plotted with the control readings, against log concentration on GraphPad (n=2).

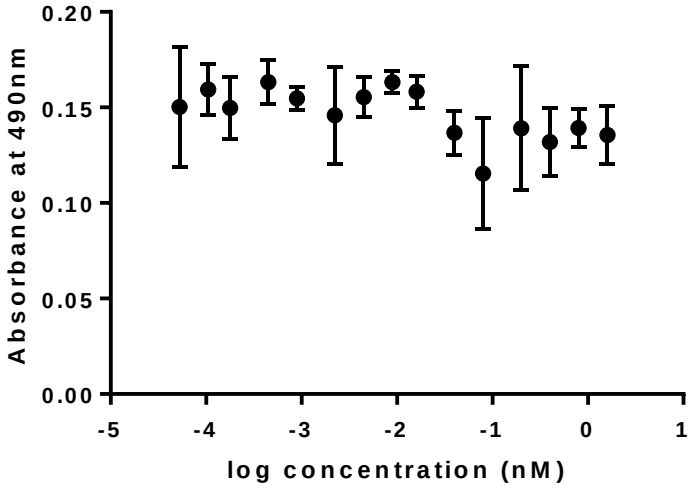

Figure 3.3.6: MTS assay results of MIN6 cells incubated with Yellow QD's functionalised with Gd-DOTA-TA (1.6 nM to 0.0000263 nM) overnight at 37°C, 5% CO2. After overnight incubation, cells were washed and incubated with MTS solution for 1-2 hours. Absorption was recorded by a BIO-TEK Synergy HT plate reader at 490nm and absorption data plotted with the control readings, against log concentration on GraphPad (n=2).

.

The results of HEK-293 cells incubated with Yellow QD's functionalised with Exendin-4 and Gd-DOTA-TA are shown in figure 3.3.7. It shows the data points don't have a clear correlation and the error bars are large. The results indicate that the controls were in consistent and cells likely became less viable at approximately 0.32nM and the data points after this, which display a higher absorbance was due to infection. The bacteria present likely reacted with the MTS solution, producing a colour change that was read by the BIO-TEK Synergy HT plate reader. The results of the MIN6 cells that were incubated with Yellow QD's functionalised with Exendin-4 and Gd-DOTA-TA are shown in figure 3.3.8. The graph appears to slow a increase in absorbance as the concentration increases. This is unexpected because we expected the cells to decrease in absorbance as the concentration increased.

The MTS results are varied and not desirable. This being because the MTS assays with the different compounds often showed a large amount of error or inconsistencies, meaning the true effects can not be determined. The IC_{50} could also not be determined for this reason. Some experiments exhibited infection so there is need for repetition. To prevent this, smaller cell numbers per well could be implicated to prevent over confluency or infection. This is supported by the review paper by Aslantürk (2017) that lists MTS assays have limitations in that the readings are sensitive to cell number, cell type, and incubations time with the suggestion the minimum time MTS needs to be incubated on cells is 1 hour, but should be as long as 3 hours. The review also lists advantages of comparing different assay results over different time periods e.g 24 hours, 48 hours, 72 hours which should be investigated in future studies with the compounds used in this project.

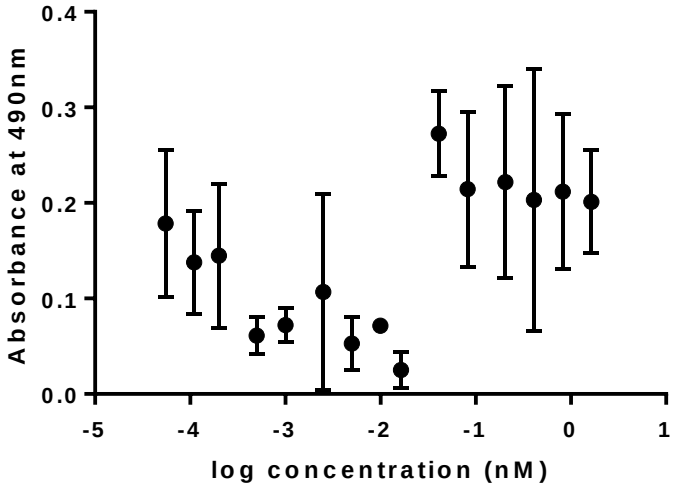

Figure 3.3.7: MTS assay results of HEK-293 cells incubated with Yellow QD's functionalised with Exendin-4 and Gd-DOTA-TA (1.64 nM to 0.000055 nM) overnight at 37°C, 5% CO2. After overnight incubation, cells were washed and incubated with MTS solution for 1-2 hours. Absorption was recorded by a BIO-TEK Synergy HT plate reader at 490nm and absorption data plotted with the control readings, against log concentration on GraphPad (n=2).

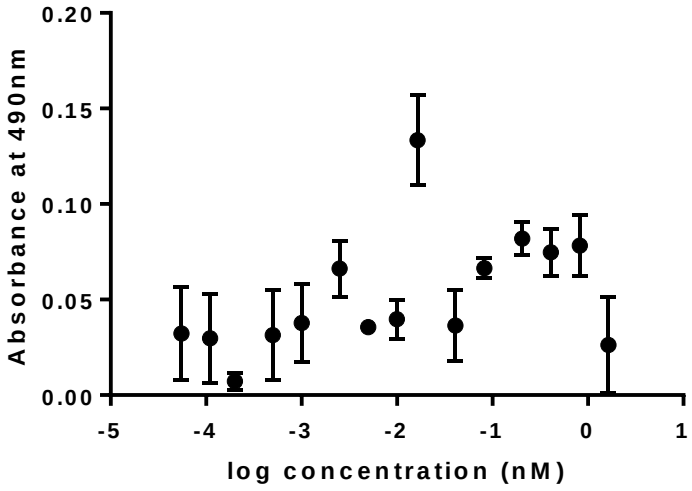

Figure 3.3.8: MTS assay results of MIN6 cells incubated with Yellow QD's functionalised with Exendin-4 and Gd-DOTA-TA (1.64nM to 0.000055 nM) overnight at 37°C, 5% CO2. After overnight incubation, cells were washed and incubated with MTS solution for 1-2 hours. Absorption was recorded by a BIO-TEK Synergy HT plate reader at 490nm and absorption data plotted with the control readings, against log concentration on GraphPad (n=2).

4. Conclusion

This Master's project aimed to develop a multimodal imaging fluorescent/MRI probe to image the β-cell mass in the pancreas. This agent was formed by functionalising the surface of fluorescent red and yellow emitting quantum dots with Exendin-4 for targeting of the GLP1-R and Gd-DOTA-TA for MRI. The probe was developed using QD's between 2.5nm and 2.75nm, and they were provided in Hexane, undergoing phase transfer and then functionalisation. Characterisation of the probe involved collecting emission and excitation profiles, in addition to DLS and Zeta potential readings. Though some of the readings suggested aggregation, biological studies were conducted in the two cell lines to determine cell viability and localisation of the probe in the cell.

FACS analysis confirmed the presence of the GLP1-R in the MIN6 cells, and therefore, confocal studies were done to determine whether the Exendin-4 in the multimodal probe was specifically binding to this receptor. The confocal studies showed evidence of the probe being internalised into the cell. Furthermore, there was evidence that the agent (and QD'S functionalised with Exendin) were specifically localising to the cell membrane. Cell viability studies were also conducted, but the results were varied, and therefore the true effects of the probe could not be determined.

The literature discussing the use of multimodal imaging agents is evolving. There is a greater focus on the use of PET and MRI imaging agents, conjugated with specific proteins (Key & Leary, 2014) to target receptors, or biological processes of interest. The literature in regards to quantum dots in biological applications is still focused on the heavy metal types (Barroso, 2011) with increasing work in the InP/ZnS variety though it is still limited. Despite this, they have been used in biological applications (Chen *et al*., 2018). Though currently there is still little work on these type of QD's with Exendin-4 for Diabetes research. Exendin-4 has been used in specific receptor targeting and multimodal imaging in literature before (Sood *et al*., (2019); Ericksson *et al*., (2014)), with PET, MRI, and fluorescence being used as imaging modalities as Exendin-4 has been well established as a GLP1 agonist (Wang *et al*., 2014).

With this area still being developed, this Master's project provides preliminary findings on the potential of the InP/ZnS QD's functionalised with Exendin-4 and Gd-DOTA-TA. This probe has a potential for imaging the β-cell mass in the pancreas, but in order to progress in the future, the functionalisation of the probe needs to be repeated with emphasis on the pH in the phase transfer and functionalisation of the QD's. If this is done, there is potential for the agent to be more concentrated with better TGA to Exendin-4 and Gd-DOTA-TA ligand transfer with less aggregation. Cell viability studies need to be repeated in order to determine an accurate IC_{50}. Confocal studies have provided a starting point in determining the localisation and internalisation of the probe, but future confocal studies can help determine the specific localisation.

5. References

Anandhakrishnan, A. & Korbonits, M. (2016) Glucagon-like peptide 1 in the pathophysiology and pharmacology of clinical obesity. *World Journal of Diabetes*. 7 (20). 572-598.

Asif, M. (2014) The prevention and control type-2 diabetes by changing lifestyle and dietary pattern. *Journal of Education and Health Promotion*. 3. (1). 5-6.

Aslantürk, Ö. (2018). In Vitro Cytotoxicity and Cell Viability Assays: Principles, Advantages, and Disadvantages. Genotoxicity - A Predictable Risk to Our Actual World.

Bachmann, L., Zezell, D. M., Ribeiro, A. da C., Gomes, L., & Ito, A. S. (2006). Fluorescence Spectroscopy of Biological Tissues—A Review. *Applied Spectroscopy Reviews*, 41(6), 575–590.

Baron, M., Veres, A., Wolock, S. L., Faust, A. L., Gaujoux, R., Vetere, A., Ryu, J. H., Wagner, B. K., Shen-Orr, S. S., Klein, A. M., Melton, D. A. & Yanai, I. (2016) A single cell Transcriptomic Map of the Human and Mouse Pancreas Reveals Inter and Intra cell population structure. *Cell Systems*. 3 (4). 346-360.

Barroso, M. M. (2011) Quantum dots in Cell Biology. *Journal of Histochemistry & Cytochemistry*. 59 (3). 237-251.

Baur, L., Twigg, S. & Magnusson, R. (2012) A modern epidemic. Sydney: Sydney University Press.

Bladowska, J., Biel, A., Zimny, A., Lubkowska, K., Bednarek-Tupikowska, G., Sozanski, T., Zaleska-Dorobisz, U. and Sasiadek, M. (2011) Are T2-weighted images more useful than T1-weighted contrast-enhanced images in assessment of postoperative sella and parasellar region?. *Medical Science Monitor*, 17(10).

Brewster, S., Curtis, L. & Poole, R. (2017) Urine Versus blood ketones. *Practical Diabetes*. 34 (1). 13-15.

Broichhagen, J., Schönberger, M., Cork, S. C., Frank, J. A., Marchetti, P., Bugliani, M., Shapiro, A. M. J., Trapp, S., Rutter, G. A., Hodson, D. J., Trauner, D. (2014) Optical control of insulin release using a photoswitchable sulfonylurea. *Nature Communications*. 5. 5116.

Brunner, Y., Coute, Y., Iezzi, M., Foti, M., Fukuda, M., Hochstrasser, D. F., Wollheim, C. B. & Sanchez, J-C. (2007) Proteomics analysis of insulin secretory granules. *Molecular & Cellular Proteomics*. 6. 1007-1017.

Bonora, E. & Tuomilehto, J. (2011) The Pros and Cons of Diagnosing Diabetes With A1C. *Diabetes Care*, 34(Supplement_2), S184-S190.

Chaudhury, A., Duvoor, C., Dendi, V. S. R., Kraleti, S., Chada, A., Ravilla, R., Marco, A., Shekhawat, N. S., Montales, M. T., Kuriakose, K., Sasapu, A., Beebe, A., Patil, N., Musham., C. K., Lohani, G. P. & Mirza, W. (2017) Clinical Review of Antidiabetic drugs: implications for Type 2 Diabetes Mellitus Management. *Frontiers in Endocrinology*. 8 (6).

Chen, C., Cohrs, C., Stertmann, J., Bozsak, R. and Speier, S. (2017) Human beta cell mass and function in diabetes: Recent advances in knowledge and technologies to understand disease pathogenesis. *Molecular Metabolism*, 6(9), 943-957.

Chen, T., Li, L., Xu, G., Wang, X., Wang, J., Chen, Y., Jiang, W., Yang, Z. and Lin, G. (2018). Cytotoxicity of InP/ZnS Quantum Dots With Different Surface Functional Groups Toward Two Lung-Derived Cell Lines. *Frontiers in Pharmacology*, 9.

Christ, E., Wild, D., Forrer, F., Brandle, M., Sahli, R., Clerici, T. (2009) Glucagon-like peptide 1 receptor imaging to localization of insulinomas. *Journal of Clinical Endocrinology.* 94. 4398-4405.

Clarke, M., Viscomi, F., Chamberlain, T., Hondow, N., Adawi, A., Sturge, J., Erwin, S., Bouillard, J., Tamang, S. and Stasiuk, G. (2019). Synthesis of super bright indium phosphide colloidal quantum dots through thermal diffusion. *Communications Chemistry,* 2(1).

Combs, C. A. (2013) Fluorescence Microscopy: A concise guide to current imaging methods. *Current Protocols in neuroscience*. 2.

Connolly, B. M., Vanko, A., McQuade, P., Guenther, I., Meng, X., Rubins, D. (2012) Ex vivo imaging of pancreatic β- cells using a radiolabelled GLP-1 receptor agonist. *Molecular Imaging and Biology.* 14. 79-87.

Coppieters, K. T., Boettler, T. & von Herrath, M. (2012) Virus infection in Type 1 Diabetes. Cold Spring Harbor Perspectives in medicine. 2 (1). 2.

Currie, S., Hoggard, N., Craven, I. J., Hadjivassiliou, M., Wilkinson, I. D. (2012) Understanding MRI: basic MR Physics for physicians. *Postgraduate Medical Journal*. 89. 209-233.

Davidson, H. W., Wenzlau, J. M. & O'Brien, R. M. (2015) Zinc Transporter (ZNT8) and B- cell function. *Trends in Endocrinology & Metabolism*. 25 (8). 415-424.

Davidson, M. B. (2010) Correction to the 2010 report on the diagnosis and classification of diabetes. *Diabetes Care*. 33 (4). 57.

Deng, D., Qu, L., Zhang, J., Ma, Y. and Gu, Y. (2013) Quaternary Zn–Ag–In–Se Quantum Dots for Biomedical Optical Imaging of RGD-Modified Micelles. *ACS Applied Materials & Interfaces*, 5(21), 10858-10865.

Deng, S., Vatamaniuk, M., Huang, X., Doliba, N., Lian, M., Frank, A., Velidedeoglu, E., Desai, N., Koeberlein, B., Wolf, B., Barker, C., Naji, A., Matschinsky, F. & Markmann, J. (2004) Structural and Functional Abnormalities in the Islets Isolated From Type 2 Diabetic Subjects. *Diabetes*, 53(3), 624-632.

Duh, E., Sun, J. and Stitt, A. (2017) Diabetic retinopathy: current understanding, mechanisms, and treatment strategies. JCI Insight, 2(14). 2-17.

Elkon, K., Casali, P. (2009) Nature and functions of autoantibodies. *Nature Clinical Practice Rheumatology*. 4 (9). 491-498.

Eriksson, O., Velikyan, I., Selvaraju, R., Kandeel, F., Johansson, L., Antoni, G., Eriksson, B., Sörensen, J. and Korsgren, O. (2014). Detection of Metastatic Insulinoma by Positron Emission Tomography With [68Ga]Exendin-4—A Case Report. *The Journal of Clinical Endocrinology & Metabolism*, 99(5), pp.1519-1524.

Esqueda, A. C., López, J. A., Andreu-de-Riquer, G., Alvarado-Monzón, J. C., Ratnakar, J., Lubag, A. J. M., Sherry, D. A. & De León-Rodríguez, L. M. (2009). A New Gadolinium-based MRI Zinc Sensor. *Journal of the American Chemical Society*, 131(32), 11387–11391.

Fowler, M. (2011) Microvascular and Macrovascular Complications of Diabetes. *Clinical Diabetes*, 29(3), 116-122.

Fu, Z., Gilbert, E. R. & Liu, D. (2013) Regulation of Insulin synthesis and secretion and pancreatic β--cell dysfunction in diabetes. *Current Diabetes Reviews*. 9 (91). 25-53.

Global Report on Diabetes. (2019) World Health Organisation (WHO). Available online: http://apps.who.int/iris/bitstream/handle/10665/204871/9789241565257_eng.pdf;jsessionid=D0D1265FA71806A3701CF9402A96128C?sequence=1 [Accessed 2/1/2019].

Grand, D. J., Woodfield, C. A., Mayo-Smith, W. W. (2012) Practical Body MRI: Protocols, Applications and Image Interception. Cambridge University Press, Cambridge. Pages 1-2.

Grarup, N., Sandholt, C. H., Hanse, T. & Pedersen, O. (2014) Genetic susceptibility to type 2 diabetes and obesity: from genome-wide association studies to rare variants and beyond. *Diabetologia*. 57 (8). 1528-1541.

Habegger, K. M., Heppner, K. M., Geary, N., Bartness, T. J., DiMarchi, R. & Tschop, M. H. (2010) The metabolic actions of glucagon revisited. *Nature Reviews Endocrinology*. 6 (12). 689-697.

Hanaoka, K., Kikuchi, K., Kojima, H., Urano, Y. and Nagano, T. (2004) Development of a Zinc Ion-Selective Luminescent Lanthanide Chemosensor for Biological Applications. *Journal of the American Chemical Society*, 126(39), 12470-12476.

Harris, R. E. (2013) Epidemiology of Pancreatic Cancer. Burlington: World Headquarters.

Heller, S., Bergenstal, R., White, W., Kupfer, S., Bakris, G., Cushman, W., Mehta, C., Nissen, S., Wilson, C., Zannad, F., Liu, Y., Gourlie, N. & Cannon, C. (2017) Relationship of glycated haemoglobin and reported hypoglycaemia to cardiovascular outcomes in patients with type 2 diabetes and recent acute coronary syndrome events: The EXAMINE trial. *Diabetes, Obesity and Metabolism*, 19(5), 664-671.

Higgins, T. (2012) HbA1c for screening and diagnosis of diabetes mellitus. *Endocrine,* 43(2), 266-273.

Huang, Q., Meriman, C., Zhang, H. & Fu, D. (2017) Coupling of insulin secretion and display of a granule-resident zinc transporter ZnT8 on the surface of pancreatic β-cells. *Journal of Biological Chemistry.*

Huang, X., Fan, C., Zhu, H., Le, W., Cui, S., Chen, X., Li, W., Zhang, F., Huang, Y., Shi, D., Cui, Z., Shao, C. and Chen, B. (2018) Glypican-1-antibody-conjugated Gd-Au nanoclusters for FI/MRI dual-modal targeted detection of pancreatic cancer. *International Journal of Nanomedicine*, Volume 13, 2585-2599.

Human GLP-1R Alexa Fluor® 488-conjugated Antibody. (2019) www.rndsystems.com. Available online:https://www.rndsystems.com/products/human-glp-1r-alexa-fluor-488-conjugated-antibody-197920_fab2814g [Accessed 1/9/2019].

(Human Metabolome Database, 2019) Human Metabolome Database: Showing metabocard for D-Glucose (HMDB0000122). (2019) Hmdb.ca. Available online: http://www.hmdb.ca/metabolites/HMDB0000122 [Accessed 8/9/2019].

IBS - Photophysics of fluorescent proteins -. (2019) IBS - Institut de Biologie Structurale. Available online: http://www.ibs.fr/research/research-groups/dynamics-and-kinetics-of-molecular-processes-group-m-weik/pixel/photophysics-of-fluorescent/ [Accessed 21/1/2019].

Inaishi, J., Saisho, Y., Sato, S., Kou, K., Murakami, R., Watanabe, Y., Kitago, M., Kitagawa, Y., Yamada, T. & Itoh, H. (2016) Effects of Obesity and Diabetes on α- and β-Cell Mass in Surgically Resected Human Pancreas. *The Journal of Clinical Endocrinology & Metabolism*, 101(7), 2874-2882.

Jarnagin, R. W. (2017) Blumgart's Surgery of the Liver, Biliary Tract and Pancreas, 2-Volume Set (Sixth Edition) Elsevier. 6.

Ji, X., Peng, F., Zhong, Y., Su, Y. and He, Y. (2014) Fluorescent quantum dots: Synthesis, biomedical optical imaging, and biosafety assessment. Colloids and Surfaces B: *Biointerfaces*, 124, 132-139.

Jin, S., Hu, Y., Gu, Z., Liu, L. & Wu, H. (2011) Application of Quantum Dots in Biological Imaging. *Journal of Nanomaterials*. 2011.

Jodal, A., Schibli, R. & Behe, M. (2017) Targets and probes for non-invasive imaging of β-cells. *European Journal of Nuclear Medicine and Molecular Imaging*. 44 (4). 712-727.

Jones, A. G., Hattersley, A. T. (2013) The clinical utility of C-peptide measurement in the care of patients with diabetes. *Diabetic Medicine*. 30 (7). 803-817.

Jones, B., Buenaventura, T., Kanda, N., Chabosseau, P., Owen, B., Scott, R., Goldin, R., Angkathunyakul, N., Corrêa Jr, I., Bosco, D., Johnson, P., Piemonti, L., Marchetti, P., Shapiro, A., Cochran, B., Hanyaloglu, A., Inoue, A., Tan, T., Rutter, G., Tomas, A. and Bloom, S. (2018). Targeting GLP-1 receptor trafficking to improve agonist efficacy. *Nature Communications*, 9(1).

Juster-Switlyk, K. and Smith, A. (2016) Updates in diabetic peripheral neuropathy. F1000 Research, 5, 738.

Katti, G., Ara, S. A., Shireen, A. (2011) Magnetic Resonance Imaging (MRI) – A review. (2010) *International Journal of Dental Clinics*. 3. (1)

Kalra, S. (2014) Sodium Glucose Co-Transporter-2 (SGLT2) Inhibitors: A Review of Their Basic and Clinical Pharmacology. *Diabetes Therapy*. 5 (2). 355-366.

Ketema, E. B., Kibret, K. T. (2015) Correlation of fasting and postprandial plasma glucose with HbA1c in assessing glycemic control; systematic review and meta-analysis. *Archives of public health*. 73. 43.

Khan, H., Sobki, S. & Khan, S. (2007) Association between glycaemic control and serum lipids profile in type 2 diabetic patients: HbA1c predicts dyslipidaemia. *Clinical and Experimental Medicine*. 7 (1). 24-9.

Klein, A. M., Melton, D. A. & Yanai, I. (2016) A single cell Transcriptomic Map of the Human and Mouse Pancreas Reveals Inter and Intra cell population structure. *Cell Systems.* 3 (4). 346-360.

Knowler, W. C., Barrett-Connor, E., Fowler, S. E., Hamman, R. F., Lachin, J. M., Walker, E. A., Nathan, D. M. (2002) Reduction in the incidence of type 2 diabetes with lifestyle intervention or metformin. *The New England Journal of Medicine*. 7;346 (6). 393-403

Larsen, M. L., Horder, M., Mogensen, E. F. (1990) Effect of long-term monitoring of glycosylated haemoglobin levels in insulin-dependent diabetes mellitus. *The New England Journal of Medicine*. 323 (15). 1021-1025.

Laurent, D., Vinet, L., Lamprianou, S., Daval, M., Filhoulaud, G., Ktorza, A., Wang, H., Sewing, S., Juretschke, H.-P., Glombik, H., Meda, P., Boisgard, R., Nguyen, D. L., Stasiuk, G. J., Long, N. J., Montet, X., Hecht, P., Kramer, W., Rutter, G. A. & Hecksher-Sørensen, J. (2016), Pancreatic β-cell imaging in humans: fiction or option?. *Diabetes Obes Metab,* 18: 6–15.

Leary, J. and Key, J. (2014). Nanoparticles for multimodal in vivo imaging in nanomedicine. *International Journal of Nanomedicine*. 1(9). 711.

Lebastchi, L., Herlond, C. K. (2012) Immunologic and metabolic biomarkers of β-cell destruction in the diagnosis of Type 1 Diabetes. *Cold Spring Harbor Perspectives in Medicine*. 2 (6). 3-5.

Leighton, E., Sainsbury, C. A. R., Jones, C. G. (2017) A practical Review of C-peptide testing in diabetes. *Diabetes Therapy*. 8 (3). 475-487.

Leow, M. K. (2016) Glycated Hemoglobin (HbA1c): Clinical Applications of a Mathematical Concept. *Acta Informatica Medica.* 24 (4). 233-238.

Li, D., Chen, S., Bellomo, E. A., Tara, A. I., Kaut, C., Rutter, G. A., Li, W-H. (2011) Imaging dynamic insulin release using a fluorescent zinc indicator for monitoring induced exocytotic release (ZIMIR). Proceedings of the National Academy of Sciences. 108 (52). 21,063-21,068.

Lim, E. G., Brubaker, P. L. (2006) Glucagon-Like Peptide 1 Secretion by the L-cell. *American Diabetes Association.*

Li, J., Karunananthan, J., Pelham, B. and Kandeel, F. (2016) Imaging pancreatic islet cells by positron emission tomography. *World Journal of Radiology*, 8(9), 764.

Lodish, H., Kaiser, C. A., Berk., A., Amon, A., Ploegh, H., Bretshcer, A., Krieger, m., Martin, K. C. (2016) Molecular Cell Biology. 8th Edition

Longnecker, D. S. (2014). Anatomy and Histology of the Pancreas. Pancreapedia: Exocrine Pancreas Knowledge Base.

Lubag, A. J. M., De Leon-Rodriguez, L. M., Burgess, S. C., & Sherry, A. D. (2011). Noninvasive MRI of β-cell function using a Zn2+-responsive contrast agent. *Proceedings of the National Academy of Sciences of the United States of America*. 108(45). 18400–18405.

MacDonald, P. E., Marinis, Y. Z. D., Ramracheya, R., Salehi, A., Ma, X., Johnson, P. R. V., Cox, R., Eliasson, L. & Rorsman, P. (2007) A KATP Channel dependent pathway within α cells regulates glucagon release from both rodent and human islets of Langerhans. *Plos Biology.* Pages 1-2.

Marrif, H. & Al-Sunousi, S. (2016). Pancreatic β Cell Mass Death. *Frontiers in Pharmacology*. 7 (83).

Mathebula, S. (2018) Biochemical changes in diabetic retinopathy triggered by hyperglycaemia: A review. *African Vision and Eye Health*, 77(1).

McBride, H. M., Neuspiel, M., Wasiak, S. (2006) Mitochondria: More than just a powerhouse. *Current Biology*. 16 (14). 551-560.

Mezza, T., Muscogiuri, G., Sorice, G., Clemente, G., Hu, J., Pontecorvi, A., Holst, J., Giaccari, A. and Kulkarni, R. (2013) Insulin Resistance Alters Islet Morphology in Nondiabetic Humans. *Diabetes*, 63(3), 994-1007.

Mi, B., Xu, Y., Pan, D., Wang, L., Yang, R., Yu, C., Wan, W., Wu., Y., Y. M. (2016) Non-invasive glucagon-like peptide 1 receptor imaging in pancreas with 18F-Al-NOTA-MAL-Cys(39)-exendin-4. *Biomedical and Biophysical Research Communications.* 471 (1). 47-51.

Mo, D., Hu, L., Zeng, G., Chen, G., Wan, J., Yu, Z., Huang, Z., He, K., Zhang, C. and Cheng, M. (2017) Cadmium-containing quantum dots: properties, applications, and toxicity. *Applied Microbiology and Biotechnology*, 101(7), 2713-2733.

Mukai, E., Toyoda, K., Kimura, H., Kawashima, H., Jujimoto, H., Ueda, M. (2009) GLP-1 receptor antagonist as a potential probe for pancreatic β-cell imaging. *Biochemical and Biophysical Research Communications.* 389. 523-526.

Myers, S. (2015). Zinc Transporters and Zinc Signaling: New Insights into Their Role in Type 2 Diabetes. *International Journal of Endocrinology*. 2015. 167503.

Nadkarni, P., Chepurny, O. and Holz, G. (2014) Regulation of Glucose Homeostasis by GLP-1. *Progress in Molecular Biology and Translational Science*, 23-65.

Nakashima, K., Shimoda, M., Hamamoto, S., Tatsumi, F., Hirukawa, H., Tawaramoto, K., Kanda, Y. and Kaku, K. (2012). Self-inducible secretion of glucagon-like peptide-1 (GLP-1) that allows MIN6 cells to maintain insulin secretion and insure cell survival. *Molecular and Cellular Endocrinology*. 349 (2) .281-288.

Nam, D., Barrack, R., and Potter, H. (2014) What Are the Advantages and Disadvantages of Imaging Modalities to Diagnose Wear-related corrosion problems? *Clinical Orthopaedics and Related Research.* 472 (12). 3665-3673.

Nissen, S. & Wolski, K. (2007) Effect of Rosiglitazone on the Risk of Myocardial Infarction and Death from Cardiovascular Causes. *New England Journal of Medicine*, 356(24), 2457-2471.

Nussey, S. & Whitehead, S. (2001) *Endocrinology: An Integrated Approach.* Chapter 2. Pages 1-5.

Olsen, H. L., Theander, S., Bokvist, K., Buschard, K., Wollheim, C. B. & Gromada, J. (2005) Glucose stimulates glucagon release in single rat alpha-cells by mechanisms that mirror the stimulus-secretion coupling in β-cells. *Endocrinology* (146). 4861–4870.

Pandol, S. J. (2018). The Exocrine Pancreas. Mississippi: Morgan & Claypool Life Sciences.

Papatheodorou, P., Papanas, N., Banach, M., Papazoglou, D. & Edmonds, M. (2016). Complication of Diabetes. *Journal of Diabetes Research*. 2016. 2-8.

Pathak, R., Bridgeman, M. B. (2010) Dipeptidyl Peptidase-4 (DPP-4) Inhibitors in the Management of Diabetes. *Pharmacy and Therapeutics*. 35 (9). 509-513.

Prasad-Reddy, L. & Isaacs, D. (2015). A clinical review of GLP-1 receptor agonists: efficacy and safety in diabetes and beyond. *Drugs in context*. 4. 1-4

Quesada, I., Tuduri, E., Ripoll, C. & Nadal, Á. (2008). Physiology of the pancreatic α-cell and glucagon secretion: role in glucose homeostasis and diabetes. *Journal of Endocrinology*. 199. 5-19.

Raffo, A., Hancock, K., Polito, T., Xie, Y., Andan, G., Witkowski, P., Hardy, M., Barba, P., Ferrara, C., Maffei, A., Freeby, M., Goland, R., Leibel, R., Sweet, I. and Harris, P. (2008) Role of vesicular monoamine transporter type 2 in rodent insulin secretion and glucose metabolism revealed by its specific antagonist tetrabenazine. *Journal of Endocrinology*, 198(1), 41-49.

Rajan, S., Dickson, L., Mathew, E., Orr, C., Ellenbroek, J., Philipson, L. and Wicksteed, B. (2015). Chronic hyperglycemia downregulates GLP-1 receptor signalling in pancreatic β-cells via protein kinase A. *Molecular Metabolism*. 4(4). 265-276.

Ramachandran, A. (2014). Know the signs and symptoms of diabetes. *Indian Journal of Medical Research*. 140 (5). 579-581.

Reimer, P., Parizel, P. M., Meaney, J. F. M., Sticnoth, F-A. (2010) Clinical MR Imaging. Springer Science and Business Media.

Renz, P. B., Cavagnolli, G., Weinert, L. S., Silveiro, S. P., & Camargo, J. L. (2015). HbA1c Test as a Tool in the Diagnosis of Gestational Diabetes Mellitus. *PLoS ONE.* 10(8).

Roder, P. V., Wu, B., Liu, Y. & Han, W. (2016) Pancreatic regulation of glucose homeostasis. *Experimental and Molecular Medicine*. 11 (48). 219.

Rohlfing, C., Wiedmeyer, H., Little, R., England, J., Tennill, A. & Goldstein, D. (2002) Defining the Relationship Between Plasma Glucose and HbA1c: Analysis of glucose profiles and HbA1c in the Diabetes Control and Complications Trial. *Diabetes Care*, 25(2), 275-278.

Rorsman, P. (2007) A KATP Channel dependent pathway within α cells regulates glucagon release from both rodent and human islets of Langerhans. *Plos Biology.* 3-6.

Roy, D., Fouzder, C., Mukhuty, A., Pal, S., Mondal, M., Kundu, R. and Chowdhury, P. (2019). Designed Synthesis of Dual Emitting Silicon Quantum Dot for Cell Imaging: Direct Labeling of Alpha 2-HS-Glycoprotein. *Bioconjugate Chemistry*. 30(5). 1575-1583.

Sacks, D. (2011). A1C Versus Glucose Testing: A Comparison. *Diabetes Care*. 34 (2). 518-523.

Sarafidis, P. A., Stafylas, P. C., Georginanos, P. I., Saratzis, A. N., Lasaridis, A. N. (2010) Effect of thiazolidinediones on albuminuria and proteinuria in diabetes: a meta-analysis. *American Journal of Kidney Diseases.*

Schmidt, K. D., Leslie, R. D. G. V. (2005) Autoantibodies in Type 1 Diabetes. *Clinica Chimica Acta*. 354 (1-2). 35-40.

Selvaraju, R. K., Velikyan, I., Johansson, I., Wu, Z., Todorov, I., Shively, J. (2013) In vivo imaging of the glucagon-like peptide 1 receptor in the pancreas with 68Ga-DO3A-exendin-4. *Journal of Nuclear Medicine*. 54. 1458-1463.

Sharaf El Din, U., Salem, M. and Abdulazim, D. (2017) Diabetic nephropathy: Time to withhold development and progression - A review. *Journal of Advanced Research,* 8(4), 363-373

Sherwani, S., Khan, H., Ekhzaimy, A., Masood, A. & Sakharkar, M. (2016). The significance of HbA1c Test in Diagnosis and Prognosis of Diabetic patients. *Biomarker Insights*. 11. 95-104.

Sladek, R., Rocheleau, G., Rung, J., Dina, C., Shen, L., Serre, D., Boutin, P., Vincent, D., Belisle, A., Hadjadj, S., Balkau, B., Heude, B., Charpentier, G., Hudson, T. J., Montpetit, A., Pshezhetsky, A. V., Prentki, M., Posner, B. I., Balding, D. J., Meyre, D., Polychronakos, C., Froguel, P. (2007) A genome-wide association study identifies novel risk loci for type 2 diabetes. *Nature*. 445 (7130). 881-885.

Smith, A., Duan, H., Mohs, A. and Nie, S. (2008) Bioconjugated quantum dots for in vivo molecular and cellular imaging. *Advanced Drug Delivery Reviews*, 60(11), 1226-1240.

Sola, D., Rossi, L., Schiance, G. P. C., Maffioli, P., Bigliocca, M., Mella, R., Corliano, F., Fra, G. P., Bartoli, E., Derosa, G. (2015). Sulfonylureas and their use in clinical practice. Archives of Medical Science. 11 (4). 840-848.

Sood, A., Basher, R., Kang, M., Shukla, J., Behera, A., Walia, R., Nada, R., Mittal, B. and Bhattacharya, A. (2019). 68Ga-DOTA-Exendin PET-MRI Fusion Imaging in a Case of Insulinoma. *Clinical Nuclear Medicine*, 44(7). 1.

Spreckley, E. (2015) The L-cell in nutritional sensing and the regulation of appetite. *Frontiers in Nutrition*, 2.

Stanfield, C. L. (2013) Principles of Human Physiology. 5th edition. Alabama: Pearson Education.

Stasiuk, G. J., Minuzzi, F., Sae-Heng, M., Rivas, C., Juretschke, H.-P., Piemonti, L., Allegrini, P. R., Laurent, D., Duckworth, A. R., Beeby, A., Rutter, G. A. & Long, N. J. (2015). Dual-Modal Magnetic Resonance/Fluorescent Zinc Probes for Pancreatic β-Cell Mass Imaging. *Chemistry* (Weinheim an Der Bergstrasse, Germany). 21(13). 5023–5033.

Steppel, J. and Horton, E. (2004) Beta-cell failure in the pathogenesis of type 2 diabetes mellitus. *Current Diabetes Reports*, 4(3), 169-175.

Tyagi, S., Gupta, P., Saini, A. S., Kaushal, C., Sharma, S. (2011) The peroxisome proliferator-activated receptor: A family of nuclear receptors role in various diseases. *Journal of Advanced Pharmaceutical Technology and Research*. 2 (4). 236-240.

Tytus, M., Krasnyj, J., Jacak, W., Chuchmała, A., Donderowicz, W. and Jacak, L. (2008) Differences between photoluminescence spectra of type-I and type-II quantum dots. *Journal of Physics: Conference Series,* 104.

Urrechaga, E. (2012) High-Resolution HbA1c Separation and Hemoglobinopathy Detection with Capillary Electrophoresis. *America Journal of Clinical Pathology*. 138 (3). 448-45.

Van de Laar, F. (2008) Alpha-glucosidase inhibitors in the early treatment of type 2 diabetes. *Vascular Health and Risk Management*. 4 (6). 1189-1195.

Vats, D., Wang, H., Esterhazy, D., Dikaiou, K., Danzer, C., Honer, M., Stuker, F., Matile, H., Migliorini, C., Fischer, E., Ripoll, J., Keist, R., Krek, W., Schibil, R., Stoffel, M. & Rudin, M. (2012) Multimodal imaging of pancreatic β- cells in vivo by targeting transmembrane protein 27 (TMEM27). *Diabetologia*. 55 (9). 2407-2416.

Veening, M. A., Van Weissenbruch, M. M. & Delemarre-Van De Waal., H. A. (2002) Glucose tolerance, insulin sensitivity, and insulin secretion in children born small for gestational age. *Journal of Clinical Endocrinology and Metabolism*. 87 (10). 4657-4661.

Wang, J., Zeng, G., Huang, D., Huang, C., Lai, C., Li, N., Wei, Z., Xu, P., He, X., Lai, M. and He, Y. (2014) The Oxidative Stress of Phanerochaete chrysosporium Against Lead Toxicity. *Applied Biochemistry and Biotechnology*, 175(4), 1981-1991.

Wang, P., Yoo, B., Yang, J., Zhang, X., Ross, A., Pantazopoulos, P., Dai, G. & Moore, A. (2014). GLP-1R–Targeting Magnetic Nanoparticles for Pancreatic Islet Imaging. *Diabetes*. 63(5). 1465–1474.

Weiss, M. (2018) Insulin Biosynthesis, Secretion, Structure, and Structure-Activity Relationships. South Dartmouth: MDText.com.

Weishaupt, D., Köchli, V. D., Marincek, B. (2016) How Does MRI Work? An Introduction to the Physics and Function of Magnetic Resonance Imaging. *Journal of Nuclear Medicine*. 57 (11)

Wenzlau, J. M., Hutton, J. C. (2013) Novel Diabetes Autoantibodies and Prediction of Type 1 Diabetes. *Current Diabetes Reports.* 13 (5).

Wicki, A., Wild, D., Storch, D., Seemayer, C., Gotthardt, M., Behe, M. (2007) [Lys40(Ahx-DTPA-111In)NH2]Exendin-4 is a highly efficient radiotherapeutic for glucagon-like peptide-1 receptor targeted therapy for insulinoma. *Clinical Cancer Research*. 13. 3696-2705

Wild, D., Behe, M., Wicki, A., Storch, D., Waser, B., Gotthardt, M. (2006) [Lys40(Ahx-DTPA-111In)NH2]Exendin-4, a very promising ligand for glucagon like peptide 1 receptor targeting. *Journal of Nuclear Medicine*. 12. 2025-2033.

Wimalasena, K. (2010) Vesicular monoamine transporters: Structure-function, pharmacology, and medicinal chemistry. *Medicinal Research Reviews*, 31(4), 483-519.

Wolfsdorf, J. I., Garvey, K. C. (2016) Glycated Hemoglobin or Hemoglobin A1c. *Endocrinology: Adult and Pediatric*. 7.

Yi, B., Huang, G., Zhou, Z. (2016) Different role of zinc transporter 8 between type 1 diabetes mellitus and type 2 diabetes mellitus. *Journal of Diabetes Investigation*. 7 (4). 459-465.

Yong, K., Ding, H., Roy, I., Law, W., Bergey, E., Maitra, A. and Prasad, P. (2009). Imaging Pancreatic Cancer Using Bioconjugated InP Quantum Dots. *ACS Nano*, 3(3). 502-510.

Xiao, Y., Paudel, R., Liu, J., Ma, C., Zhang, Z. & Zhou, S. (2016) MRI contrast agents: Classification and application (Review). *International Journal of Molecular Medicine*, 38(5), 1319-1326.

Zhang, L., Bäumer, W. and Monteiro-Riviere, N. (2011). Cellular uptake mechanisms and toxicity of quantum dots in dendritic cells. *Nanomedicine*, 6(5). 777-791.

6. Appendix

Appendix 1: The DLS graph measurements of the Red QD's

			Size (d.nm):	% Volume:	St Dev (d.nm):
Z-Average (d.nm):	89.30	Peak 1:	711.8	1.6	535.0
PdI:	0.930	Peak 2:	9.559	98.4	3.552
Intercept:	0.320	Peak 3:	0.000	0.0	0.000

Result quality : Refer to quality report

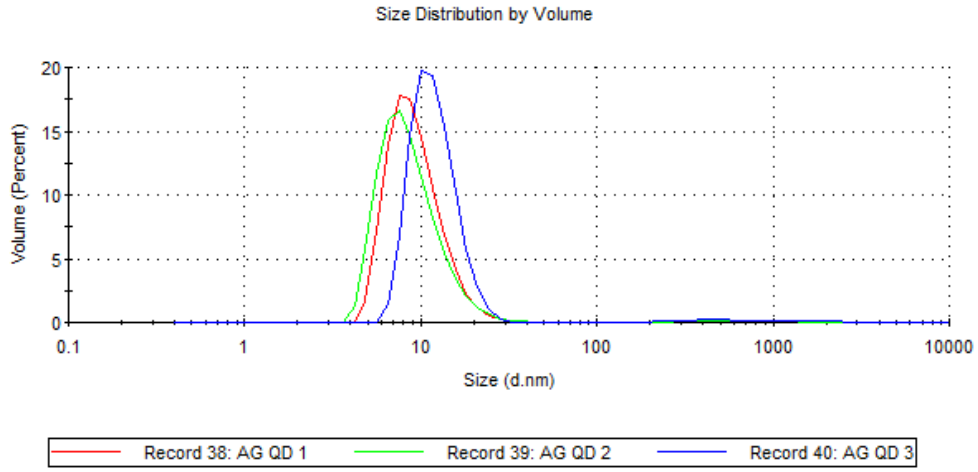

Appendix 2: The Zeta potential graph measurements of the Red QD's

			Mean (mV)	Area (%)	St Dev (mV)
Zeta Potential (mV):	-27.6	Peak 1:	-17.9	52.7	4.18
Zeta Deviation (mV):	12.0	Peak 2:	-38.3	47.3	7.06
Conductivity (mS/cm):	0.140	Peak 3:	0.00	0.0	0.00

Result quality : Good

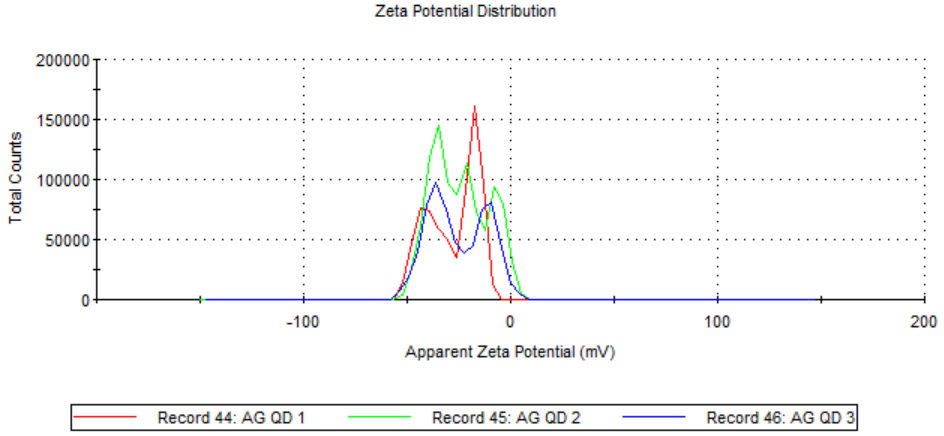

Appendix 3: The DLS graph measurements of the Red QD's functionalised with Exendin-4

			Size (d.nm):	% Volume:	St Dev (d.nm):
Z-Average (d.nm):	2032	Peak 1:	90.29	0.1	13.59
PdI:	1.000	Peak 2:	4.115	99.9	0.6175
Intercept:	0.619	Peak 3:	0.000	0.0	0.000

Result quality : Refer to quality report

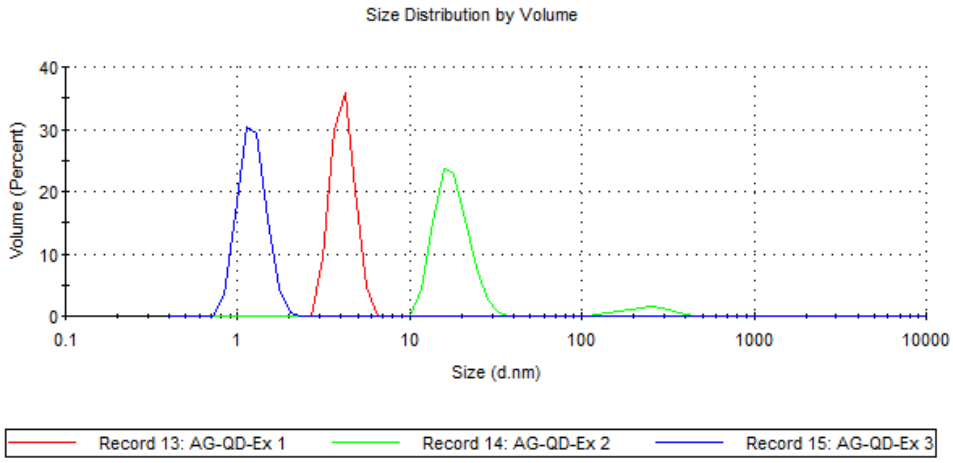

Appendix 4: The Zeta potential graph measurements of the Red QD's functionalised with Exendin-4

			Mean (mV)	Area (%)	St Dev (mV)
Zeta Potential (mV):	-0.433	Peak 1:	-101	13.3	8.44
Zeta Deviation (mV):	129	Peak 2:	-72.0	13.3	10.2
Conductivity (mS/cm):	0.360	Peak 3:	95.0	12.1	8.05

Result quality : See result quality report

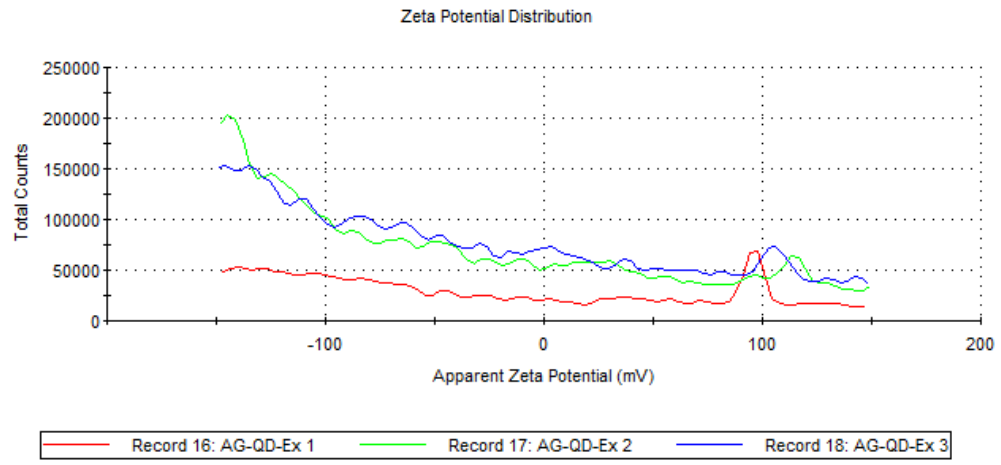

Appendix 5: The DLS graph measurements of the Red QD'S functionalised with Gd-DOTA-TA

			Size (d.nm):	% Volume:	St Dev (d.nm):
Z-Average (d.nm):	46.62	Peak 1:	18.89	96.0	6.585
PdI:	0.249	Peak 2:	257.4	0.8	113.8
Intercept:	0.453	Peak 3:	5068	3.2	820.3

Result quality : Refer to quality report

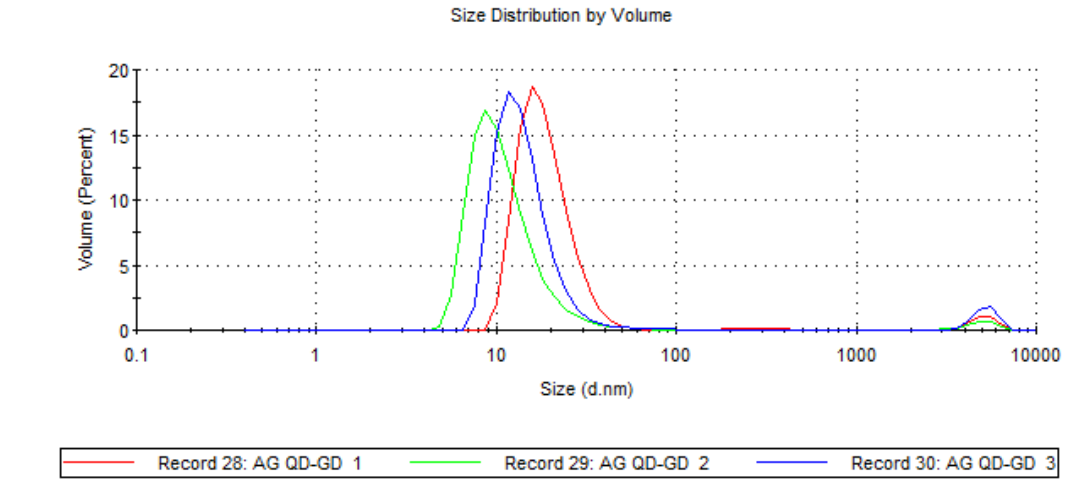

Appendix 6: The Zeta potential graph measurements of the Red QD's functionalised with Gd-DOTA-TA

			Mean (mV)	Area (%)	St Dev (mV)
Zeta Potential (mV):	-9.59	Peak 1:	-17.9	51.9	6.40
Zeta Deviation (mV):	11.6	Peak 2:	-2.63	44.9	2.31
Conductivity (mS/cm):	0.00264	Peak 3:	29.2	3.1	3.23

Result quality : See result quality report

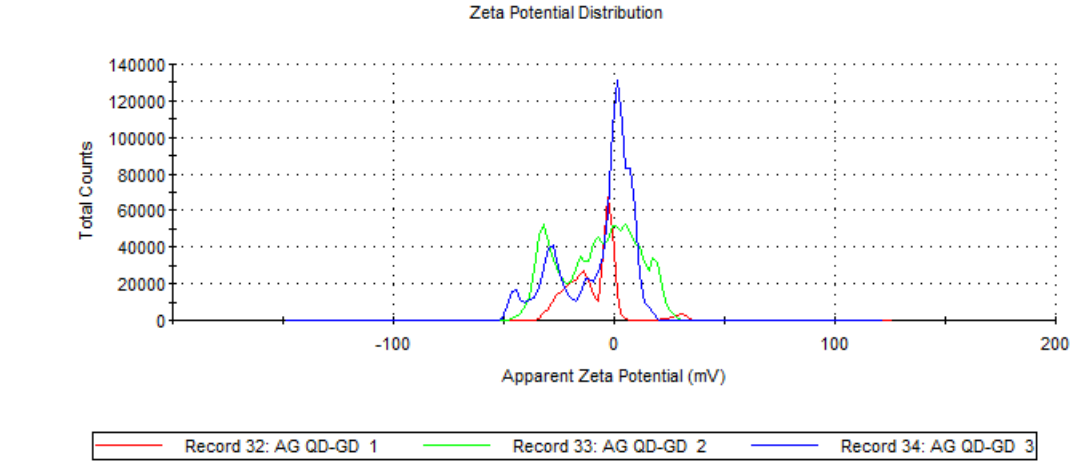

Appendix 7: The DLS graph measurements of the Red QD's functionalised with Exendin-4 and Gd-DOTA-TA

		Size (d.nm):	% Volume:	St Dev (d.nm):
Z-Average (d.nm): 533.6	Peak 1:	408.7	100.0	78.08
PdI: 0.419	Peak 2:	0.000	0.0	0.000
Intercept: 0.647	Peak 3:	0.000	0.0	0.000

Result quality : Refer to quality report

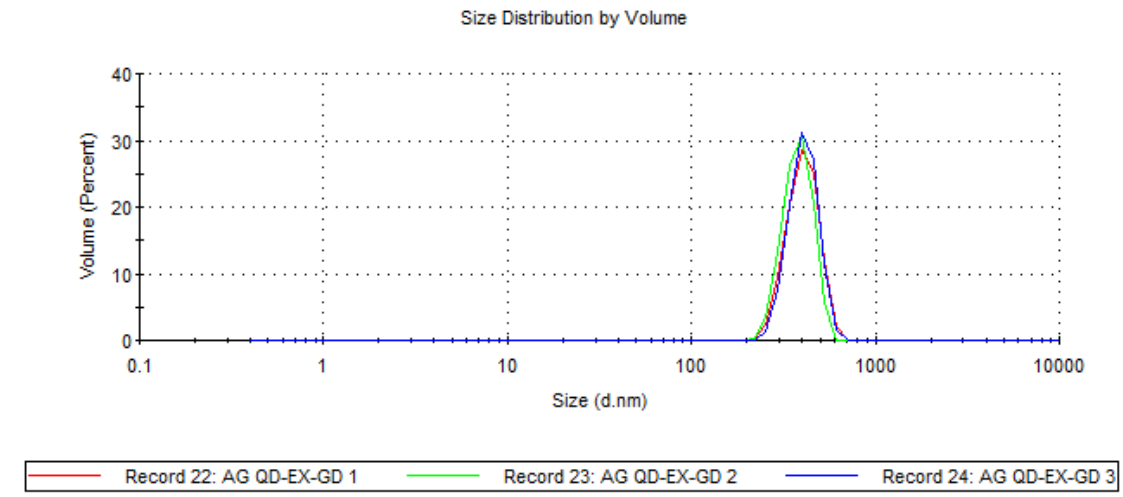

Appendix 8: The Zeta potential graph measurements of the Red QD's functionalised with Exendin-4 and Gd-DOTA-TA

		Mean (mV)	Area (%)	St Dev (mV)
Zeta Potential (mV): -20.1	Peak 1:	-23.3	89.4	6.55
Zeta Deviation (mV): 11.1	Peak 2:	6.40	10.6	2.86
Conductivity (mS/cm): 0.0168	Peak 3:	0.00	0.0	0.00

Result quality : Good